In-situ Characterization of Transient Dynamics in Laser Powder Bed Fusion Additive Manufacturing Process

By

Qilin Guo

A dissertation submitted in partial fulfillment of
the requirements for the degree of

Doctor of Philosophy
(Mechanical Engineering)

at the

UNIVERSITY OF WISCONSIN – MADISON

2022

Date of final oral examination: 08/12/2022

The dissertation is approved by the following members of the Final Oral Committee:
- Lianyi Chen, Associate Professor, Mechanical Engineering
- Frank E. Pfefferkorn, Professor, Mechanical Engineering
- Dan J. Thoma, Professor, Materials Science and Engineering
- John H. Perepezko, Professor, Materials Science and Engineering
- Sindo Kou, Professor, Materials Science and Engineering

Acknowledgements

I would like to thank my parents, Qingdong Guo and Guirong Liu, for their lifelong support and unconditional love. I am deeply grateful to my advisor, Lianyi Chen, for guiding me through my Ph.D. studies, always being there for me, believing in me, encouraging me, and preparing me for the next chapter of my career. I want to extend my sincere thanks to my other committee members: Frank E. Pfefferkorn, Dan J. Thoma, John H. Perepezko, and Sindo Kou, for their invaluable advice and feedback. I would like to express my sincere gratitude to my fellow lab mates for the countless inspirations and the joyful moments. Ultimately, I would like to offer my special thanks to my partner, Kang Yang, for her love, understanding, and trust.

Table of Contents

List of Figures

List of Tables

Nomenclature and Acronyms

1D = One-dimensional
2D = Two-dimensional
3D = Three-dimensional
AM = Additive manufacturing
APT = Atom probe tomography
BCC = Body-centered cubic
C_17-4 = Commercial additively manufactured 17-4PH stainless steel
CAD = Computer-aided design
CALPHAD = Calculation of phase diagrams
DED = Directed Energy Deposition
EBSD = Electron backscatter diffraction
EDM = Electrical discharge machining
FCC = Face-centered cubic
FIB = Focused ion beam
HRXRD = High-resolution X-ray diffraction
ICP = Inductively coupled plasma
ISCD = Inorganic crystal structure database
IED = Input energy density
LPBF = Laser powder bed fusion
SAXS = Small-angle X-ray scattering
SEM = Scanning electron microscope/microscopy
TMA = Thermomechanical analysis
UW_17-4 = A new 17-4PH stainless steel composition developed in this work
XRD = X-ray diffraction

Abstract

Laser powder bed fusion (LPBF) is one of the dominating techniques in metal additive manufacturing (AM). It enables the fabrication of geometrically and compositionally complex parts unachievable by conventional manufacturing methods. However, understanding the complex transient dynamics during the LPBF process is greatly hindered by the lack of experimental characterizations, mainly due to two reasons: (a) It is challenging to monitor the dynamics inside metals due to their opacity to visible light. (b) The transient dynamics occur in a small space within a short time, which requires the monitoring tools to have both high temporal and spatial resolution.

This work studied the multi-level transient dynamics during the LPBF process by addressing the above challenges with in-situ high-energy synchrotron X-ray imaging & diffraction. The mechanisms and driving forces of the powder spattering process—one of the significant causes of defect formation in LPBF—were identified and quantified in Chapter 3. The spattering behaviors in terms of environmental pressures and locations were explicitly characterized. Chapter 4 answers why an identical input energy density could lead to various melt pool sizes and shapes by exploring the mechanism of melt pool variation under different processing conditions. In Chapters 5 and 6, a flow-tracing approach was developed to study the melt flow dynamics during the LPBF process. The regular melt pool patterns within the conduction-mode and keyhole-mode melt pools were experimentally revealed and quantified for the first time in Chapter 5, while the unstable melt flow formation mechanisms and consequences were illustrated in Chapter 6. Chapter 7 revealed the phase transformation dynamics in 17-4PH stainless steel during the rapid solidification of the melt pool. Informed by the phase transformation dynamics,

a 17-4PH composition was developed specifically for AM process to consistently deliver the desired phase under a wide range of cooling rates and withstand common environment impurities. Overall, this work provides critical insights into the transient process dynamics during LPBF, which serves as a foundation to guide the mitigation of part defects and the optimization of processing conditions. The direct observation of the process dynamics is also important for developing and validating high-fidelity computational models.

Chapter 1: Introduction

This chapter introduces the concept of the laser powder bed fusion (LPBF) additive manufacturing (AM) process and reviews the state-of-the-art studies of powder spattering, melt pool evolution, and melt flow dynamics. In the end, it presents the objectives of this work, aiming to address the challenges met by the previous research.

1.1 Laser Powder Bed Fusion

Laser powder bed fusion (LPBF) is currently one of the dominating techniques in metal additive manufacturing (AM). It can fabricate geometrically and compositionally complex parts unachievable in conventional manufacturing methods [1,2]. During a typical LPBF process, a three-dimensional (3D) model of the part is first created in computer-aided design (CAD) software and sliced into multiple layers with a layer thickness that varies between 20–100 μm. According to the specified layer thickness, a thin layer of metal powder is spread on the build plate. A laser will scan and fuse the selective area of the powder bed to build a cross-section defined in the CAD software. The final part can be fabricated by repeating the powder-spreading and selective laser melting process.

To fabricate parts with desired quality and performance, extensive research has been dedicated to correlating the material microstructures with the AM processing conditions [3–7]. However, the complex physical dynamics (defect formation, laser-matter interaction, fluid dynamics, etc.) intrinsic to the LPBF-AM process pose a significant barrier to establishing the process-microstructure relationship. Therefore, there is a great need to experimentally characterize the process dynamics during LPBF to understand the underlying physical mechanisms.

1.2 In-situ Investigation of Powder Spattering

A major cause of defect formation in LPBF is powder spattering during laser scanning on the powder bed [8]. The most commonly used tool for experimental observation and characterization of powder spattering is visible-light videography [9,10]. Liquid spatter and hot powder spatter are relatively easy to capture by a visible light camera due to the incandescence. Thus, the quantified information of spatters, such as their size, amount, speed, and moving direction, can be acquired [11]. Cold powder spattering can also be observed with an additional light source (laser or tungsten filament lamp). However, due to the large difference in brightness between the liquid and solid material, it is difficult to observe both hot and cold spattering at the same time with high resolution using visible-light videography.

Optical pyrometer and infrared thermography have also been used to study powder spattering behavior [12,13]. The major challenge is their low spatial and temporal resolution [14]. Another challenge is that low-temperature spatter (cold solid powder spatter) cannot be detected by a thermal camera due to low radiance. Therefore, thermography cannot observe the whole picture of the spattering behavior.

Due to the lack of proper characterization tools, the powder spattering mechanism during the LPBF process was poorly understood before the work reported in this dissertation. Specifically, several questions remained unclear: (1) How does laser-matter interaction initiate powder spattering? (2) What are the driving forces for the powder motion? (3) What is the behavior of total spattering (both hot and cold)? The answers to these questions are critical for understanding the powder spattering behavior and thus are helpful for developing new process technologies to mitigate or eliminate the defects in the as-printed LPBF parts.

1.3 Characterization of Melt Pool Variations

As the direct product of laser-matter interaction, the melt pool is the matrix for bonding various physical dynamics during the LPBF process (such as powder spattering). Therefore, it is essential to study the melt pool evolution under different processing conditions.

The primary processing parameters in LPBF are commonly organized by a metric named “input energy density (IED)”, which can be defined as laser power (P) over the product of laser scan speed (v) and the laser beam diameter (d), i.e., IED = $P/(v \cdot d)$ with a unit of J/cm^2. It is widely used for designing processing parameters for additive manufacturing or expressing properties of additively manufactured materials. However, significant microstructure and property variations were observed in the parts produced under a constant IED, e.g., variations in crystalline phases and grains[15], porosity and density [16], mechanical properties [17], etc. Recent research shows that these microstructure and property variations are associated with the variations in melt pool size and geometry under the same IED [18,19]. Since the same amount of energy is supplied from the heat source under the same IED, it was not clear why the same IED could lead to different melt pool sizes and shapes. Thus, it is critical to experimentally quantify melt pool variation under a constant IED and understand the underlying mechanisms.

It is challenging to accurately characterize a melt pool’s dimension, geometry, and volume by ex-situ methods because the solid-liquid interface is inherently difficult to observe by ex-situ methods (no liquid exists under ex-situ conditions). The work done based on ex-situ methods had to estimate the melt pool dimensions (length, width, depth) from the solidified melt track [20–22] or the volumetric melting rate from the product of laser scan speed and the cross-section area of the melt track [23,24]. For in-situ techniques, it is also difficult to observe the solid-liquid interface beneath the surface of the melt pool during laser melting. Conventional in-situ characterization tools, such as visible light radiography and thermography, cannot receive signals from the interior of metals. The X-ray can penetrate metals, whereas the limited flux of X-ray photons in a lab or mid-energy synchrotron X-ray facility cannot generate good contrast to distinguish the slight difference in density between solid and liquid phases.

Due to the challenges in the experimental characterization of the melt pool during laser processing, no study has reported direct observation or quantification of the melt pool dynamics during the LPBF process before the work presented in this dissertation. The mechanism for causing melt pool variation under a constant IED was unclear. The melt pool evolution path under varying P-v combinations within a constant IED remains to be uncovered.

1.4 Characterization of Melt Flow Dynamics

Melt flow within the melt pool determines the heat transfer and mass transfer, thus playing a critical role in the development of the melt pool. Therefore, understanding the melt flow behavior in the melt pool is crucial for microstructure prediction and process control.

Due to the difficulty in experimentally visualizing the fluid flow inside the melt pool, extensive modeling and simulation work have been carried out to study the flow patterns under various conditions. However, given the complexity of the physics in laser additive manufacturing, it is extremely challenging to simulate the involved multi-physics phenomena using a single numerical model [25]. Major assumptions must be applied in most simulations [25–27]: some assumptions are applied to maintain calculation efficiency, some are made due to the unavailability of data, and others are made because the underlying physics are still not well understood. As a result, the calculated melt flows are not always consistent and sometimes are even opposite in the reported research [28–30]. Thus, it is critical to experimentally unveil the melt flow behavior within the melt pool in laser additive manufacturing to understand the actual melt flow behavior and to develop and validate computational models.

In the last few decades, extensive work has been done in the welding community to characterize the liquid flow behavior in the melt pool using flow tracers [31–35]. The tracers used in welding research are usually of relatively large size (50 µm – 500 µm) and a small amount (≤ 80 counts per test), which can only trace melt flow behavior in a localized area of the melt pool. Visible light imaging, such as glass flanking [36], was used to observe the flow pattern inside the melt pool directly. However, the glass plate changes the heat transfer condition and cuts off the flow at the cross-section so that the observed flow pattern may differ from the actual laser processing condition. Characterizing the three-dimensional melt flow in real LPBF conditions is much more challenging than welding because the laser usually scans at a much higher speed and the resulting melt pool is much smaller.

To understand the melt flow behavior during the LPBF process and to address the discrepancies observed from computational results, there is an urgent need to develop appropriate approaches for the direct observation and quantification of melt flow dynamics in LPBF. The melt flow pattern in the entire melt pool under different laser melting modes remains unclear. The prevailing physical processes, such as heat-transfer mode, at specific locations of the melt pool need to be identified and characterized.

1.5 Characterization of Melt Flow Instability

To fabricate parts with desirable and predictable quality, extensive research has been dedicated to correlating the process dynamics (melt pool variation [37,38], pore formation [39–41], spatter generation [42,43], keyhole oscillation [44–46], etc.) with the processing conditions (laser power, scan speed, beam size, etc.). The aim was to establish an “optimized” set of parameters to produce parts with fewer defects and higher density [14,47–49]. However, there are uncertainties intrinsic to the laser metal additive manufacturing process where some unstable physical dynamics are not tightly bonded to specific processing conditions [14,49–52]. Such instabilities pose great uncertainty to the qualification and certification of the additively manufactured parts [52–54], which require explicit characterization through direct observations.

To investigate the process instabilities, it is essential to trace the transient melt flow behavior inside the melt pool—the direct product of laser-matter interaction. However, the opacity of metals to visible light poses a great barrier to direct observation of the molten metals within the melt pools. To overcome this challenge, recent research has applied synchrotron radiation-based in-situ X-ray imaging to observe the physical dynamics within metals, such as the work reported in Chapter 4 of this dissertation and in [38,39,55–57]. By in-situ X-ray imaging, the localized melt flow behavior within a laser-induced metallic melt pool could be inferred from the movement of pores generated during the process

[38,57,58]. The regular melt flow patterns within the whole melt pool have also been studied using tungsten particles as flow tracers, such as the work reported in Chapter 5 of this dissertation and in [39,55,56,59].

However, limited research has been conducted toward experimental investigations on melt flow instabilities. In the blown-powder directed energy deposition (DED) additive manufacturing process, it was reported that the impact of feeding particles could cause melt pool surface fluctuations, generate porosity, and cause keyhole oscillations [57]. In the LPBF additive manufacturing process, it was reported that high laser scan speeds and large powder layer thickness could cause unstable melt flow, leading to a rough surface finish [60]. The melt flow behavior was inferred by the morphology of solidified track, as well as the powder spattering behavior. Recent research using in-situ X-ray imaging to monitor the LPBF process has reported several defect-formation mechanisms resulting from unstable melt flow or keyhole fluctuations. However, the unstable melt flow behavior was not characterized [61].

Computational modeling work has also been performed to study melt flow instabilities. In general, the studies focused on two aspects: the instability formation mechanism and the consequences of the instabilities on the process. Surface tension variation was identified as a source of melt flow instabilities, as surface tension is one of the major driving forces for liquid migration. The surface tension fluctuations could be induced by both improper processing parameters (such as hatch spacing [62]) and chemical composition variations (such as increased oxidation levels [63]). The inhomogeneous powder packing in the LPBF powder bed also serves as a source to disturb the melt flow by cutting off the liquid migration at the loose-packing region, resulting in part defects such as porosity and balling [64]. As for the consequences, the melt flow instabilities have been reported to be accountable for the breakup of melt tracks (Plateau-Rayleigh instability), the trap of gas pores, and the creation of a denudation zone around the keyhole rim during LPBF [28]. Other melt flow-induced process instabilities, such as liquid ejection and periodical oscillations of keyholes, have also been demonstrated by high-fidelity simulations [44,65,66].

So far, in-process experimental characterization of the melt flow instabilities during LPBF has not been reported. The formation mechanisms, time scale and spatial scale, and the impacts on the part quality for the melt flow instabilities occurring during the LPBF process have been largely unclear, which need to be characterized experimentally and quantitatively.

1.6 Characterization of Phase Transformation Dynamics

The complex and often extreme thermal conditions of AM, intrinsic to a localized heat source-material interaction, pose considerable challenges to consistently obtaining desired phases in the as-printed parts, especially for materials with multi-stage phase transformation during AM fabrication (e.g., steels [67], titanium alloys [68], nickel superalloys [69,70]). These challenges frequently manifest themselves in three aspects: (1) AM solidification occurs far from equilibrium due to its rapid cooling rate, causing the phase transformation sequence/timing to deviate from predictions made by the equilibrium phase diagram [71,72]. (2) The heating/cooling conditions at different locations of the melt pool are heterogeneous, leading to diversified phase constitutions within a single melt pool [73,74]. (3) The thermal conditions across different machines, different parts within the same batch, and even different regions within a single part are all different, leading to inconsistent phase constitutions from print to print [75].

One prominent example is 17-4 precipitation-hardening (PH) martensitic stainless steel (also known as 17-4 PH or type 630 stainless steel), which exhibits various unwanted phases in the as-printed condition [76]. In a conventional manufacturing process with a low cooling rate, 17-4 PH steel solidifies following a phase transformation sequence of liquid (L)–δ-ferrite (δ)–austenite (γ)–martensite (α') [77]. δ-ferrite (δ) and martensite (α') in 17-4 have a body-centered cubic (BCC) lattice structure; austenite (γ) has a face-centered cubic (FCC) lattice structure. The desired final phase in 17-4 PH steel is the martensitic phase (α'), enabling its excellent mechanical performance. The typical processing of 17-4 steel also includes a high-temperature solution heat treatment, followed by quenching and aging at low temperatures for an extended period to introduce nanoscopic precipitates, which further increases its mechanical strength. In general, precipitation-hardening (PH) stainless steels have the highest tensile strength of stainless steels. 17-4 steel is the most widely used PH-grade stainless steel and has drawn much attention for its potential applications enabled by AM technologies.

However, the development of AM 17-4 steel has encountered severe phase control challenges. While martensite in conventional 17-4 provides its primary strength, AM 17-4 in its as-built state can contain a significant amount of retained austenite (up to 100% reported in the literature) and even a substantial fraction of δ-ferrite (up to >95% reported in the literature) [78–89]. To make things worse, the fractions of residual austenite and δ-ferrite phases also vary significantly across different printing parameters, AM build machines, and AM technologies. These residual phases deteriorate the properties of the printed parts and create significant uncertainties in the targeted applications that rely on the designed properties of 17-4 steels [84,88,90–92]. It is, therefore, imperative to understand the nonequilibrium phase transformation sequence of 17-4 steel during AM processing and develop an alloy within the 17-4 composition window that can reproducibly deliver 17-4's performance characteristics desirably in its as-built state.

1.7 Objectives of This Work

In this work, in-situ high-energy X-ray imaging & diffraction techniques will be used to address the challenges encountered by previous research to characterize the process dynamics above, and especially, within the metals during the LPBF process. Specifically, to understand the mechanism for powder spattering during the LPBF process, Chapter 3 will present the investigation of powder spattering dynamics as a function of time, environment pressure, and location. The initiation mechanism, the driving force, and the statistical behavior of total spattering will be examined. Chapter 4 will present the first direct observation and quantification of melt pool variations under constant IEDs. The melt pool evolution in size and shape under different processing conditions will be evaluated. The energy balance during the process will be examined to identify the underlying mechanism that causes melt pool variations under a constant IED. A flow tracing approach will be developed and adopted in Chapters 5 and 6 to study the melt flow dynamics within the melt pool during the LPBF process. Chapter 5 will reveal and quantify the regular melt flow patterns within the conduction-mode and keyhole-mode melt pools. The validity of the flow tracing approach, the location-dependent dominating driving forces of liquid flow, and the dominating physical process within the melt pool will also be discussed. Chapter 6 will focus on characterizing the melt flow instabilities and demonstrating their influences on the LPBF process. The mechanisms for causing various types of melt flow instabilities will be illustrated. The melt flow evolution path will be discussed with the combined information from Chapters 5 and 6. At last, the objective of Chapter 7 is to understand the complex phase transformation dynamics in 17-4PH stainless steel and develop an alloy composition that can consistently deliver the desired phase and the promised performance. The phase transformation behavior of the developed alloy will be tested under various cooling rates with/without environmental impurities. The microstructure and mechanical properties will be characterized for the developed alloy after 3D printing.

The multi-level in-situ characterization of process dynamics in this work provides critical insights into the LPBF process, which serves as a foundation for mitigating process defects and developing robust processing conditions. The experimental results are also crucial for developing and validating high-fidelity computational models.

Chapter 2: In-situ X-ray Imaging Methods and Materials

This chapter provides an overview of general experimental methods used in Chapters 3–6, including the in-situ X-ray imaging setup and the materials. The in-situ X-ray diffraction setup used in Chapter 7 will be separately introduced in Section 7.1.

In-situ high-speed, high-energy, high-resolution X-ray imaging technique was used in this work to overcome the limitations of conventional characterization tools in studying the dynamics of the AM process. The experimental approach is schematically shown in Figure 1.

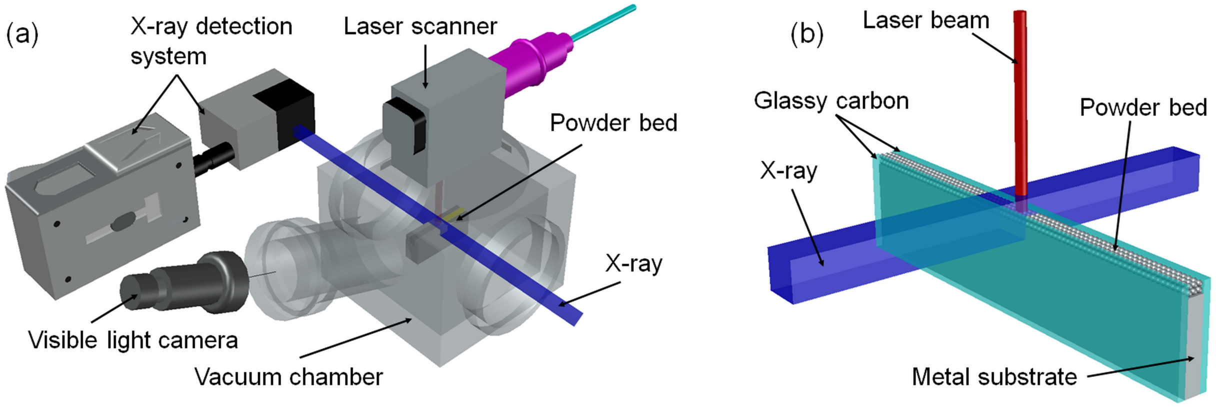

Figure 1. Schematic of the experimental set-up for in-situ LPBF high-speed high-energy X-ray imaging. Original figure from [43].

The system was developed and assembled by collaborators (Tao Sun, Cang Zhao, Kamel Fezzaa) at the beamline 32-ID-B, Advanced Photon Source, Argonne National Laboratory. The X-ray beam is an undulator-generated pink beam with the harmonic energy at 24 keV and an energy bandwidth of 5~7%. The X-ray beam can penetrate through metal samples (up to ~5.5 mm aluminum or ~1 mm stainless steel, yet varies depending on the desired temporal resolution), and the transmitted signal is captured by a detection system downstream where the X-ray signal is converted into visible light using a scintillator (LuAG:Ce, 100 μm thickness) and recorded by a high-speed camera (Photron FastCam SA-Z). The exposure time is set to be 500 ns. The camera records with a tunable frame rate of up to 1 MHz and a spatial resolution of up to 1 μm. ImageJ is used to process all of the recorded images.

A focused laser beam is applied from the top of the powder bed (the sample). The laser is an IPG continuous-wave (CW) ytterbium fiber laser with a wavelength of 1070 nm and maximum output power of 520W. This study consists of stationary laser beam melting tests (with a $1/e^2$ laser spot size of 200 μm and a duration time of 1 ms) and laser single-track scanning tests (with a $1/e^2$ laser spot size of 100 μm). The beam profile is Gaussian under both conditions.

The sample is placed on the X-ray path in a vacuum chamber refilled with argon gas. A motion stage (not shown in the schematic) holds the sample and allows z-direction (vertically) movement to adjust the laser spot size. The whole chamber is carried by an x-y-z motion stage (not shown in the schematic) so that an X-ray can illuminate different regions of the sample. By controlling the refilled argon amount in the chamber, tests under pressures of 1 atm to 10^{-4} atm can be conducted.

The detailed powder bed assembly (the sample) is schematically shown in Figure 1(b). The powders are applied on a metal substrate (build plate) made of the same material as the powder. The powders are spread manually by using a wiper. Two pieces of glassy carbon are used as side walls to hold the powder bed and to ensure X-ray transparency along the X-ray beam path. The uniformity of the powder bed is checked before laser melting experiments. The powder layer thickness is adjustable by controlling the height difference between the substrate and the glassy carbon walls. A layer thickness of 100 μm was generally used in this work unless specified otherwise. To find out a suitable powder bed width (along X-ray penetration direction) for this research, laser single-track scan tests on substrates with different thicknesses (1.0 mm, 0.8 mm, 0.5 mm) were conducted. No significant difference was observed. Therefore, 0.5 mm was chosen to be the powder-bed width for all the experiments in this paper due to better X-ray transparency unless specified otherwise.

The materials used in this work are mainly 316L stainless steel for stationary laser beam melting, and AlSi10Mg, for single-track laser scanning. Both materials are widely used in the metal AM industry. The powder size distributions of the two materials are shown in Figure 2. The compositions of 316L stainless are AlSi10Mg alloy are listed in Table 1.

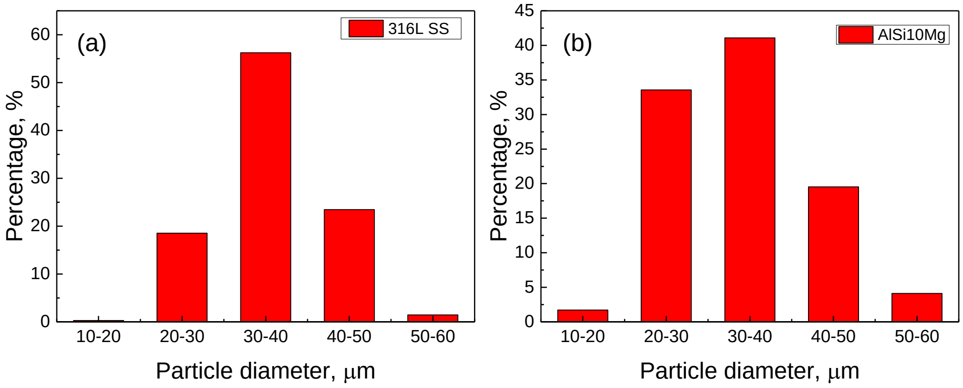

Figure 2. Particle size distributions of (a) 316L stainless steel and (b) AlSi10Mg powder. Original figure from [43].

Chapter 3: Transient Dynamics of Powder Spattering

This chapter contains experimental data and results that have been published in the following work:

Q. Guo, C. Zhao, L.I. Escano, Z. Young, L. Xiong, K. Fezzaa, W. Everhart, B. Brown, T. Sun, L. Chen, Transient dynamics of powder spattering in laser powder bed fusion additive manufacturing process revealed by in-situ high-speed high-energy X-ray imaging, Acta Mater. 151 (2018) 169–180. [43]

The publication rights for this section are given in Appendix A. Appropriate recognition is given to the relevant citation for the material in which it was originally published. The presented material represents my contributions and material collected with or by a collaborator has been highlighted as such.

This chapter reports the detailed dynamics of powder spattering during laser melting. The transient dynamics of powder spattering in the LPBF process were revealed. Powder spattering behaviors were uncovered as a function of time, environment pressure, and location. The mechanisms of powder spattering were depicted on a schematic map. Quantifications of the particles' moving speed, acceleration, and driving force as a function of time and pressure were performed. Potential ways to mitigate powder spattering in the LPBF process are proposed based on the revealed transient powder dynamics and spattering mechanisms.

3.1 Powder Dynamics as a Function of Time and Environment Pressure

3.1.1 Powder Motion as a Function of Time and Environment Pressure

The powder dynamics under three different environmental pressures of 10^{-4} atm, 0.05 atm, and 1 atm were recorded by X-ray imaging at 54310 frames per second with 312 W stationary laser beam melting. Three frames of each condition were displayed in Figure 3. Red circles indicate representative particles with their trajectories highlighted by yellow dashed lines, and green arrows highlight the overall particle moving tendency.

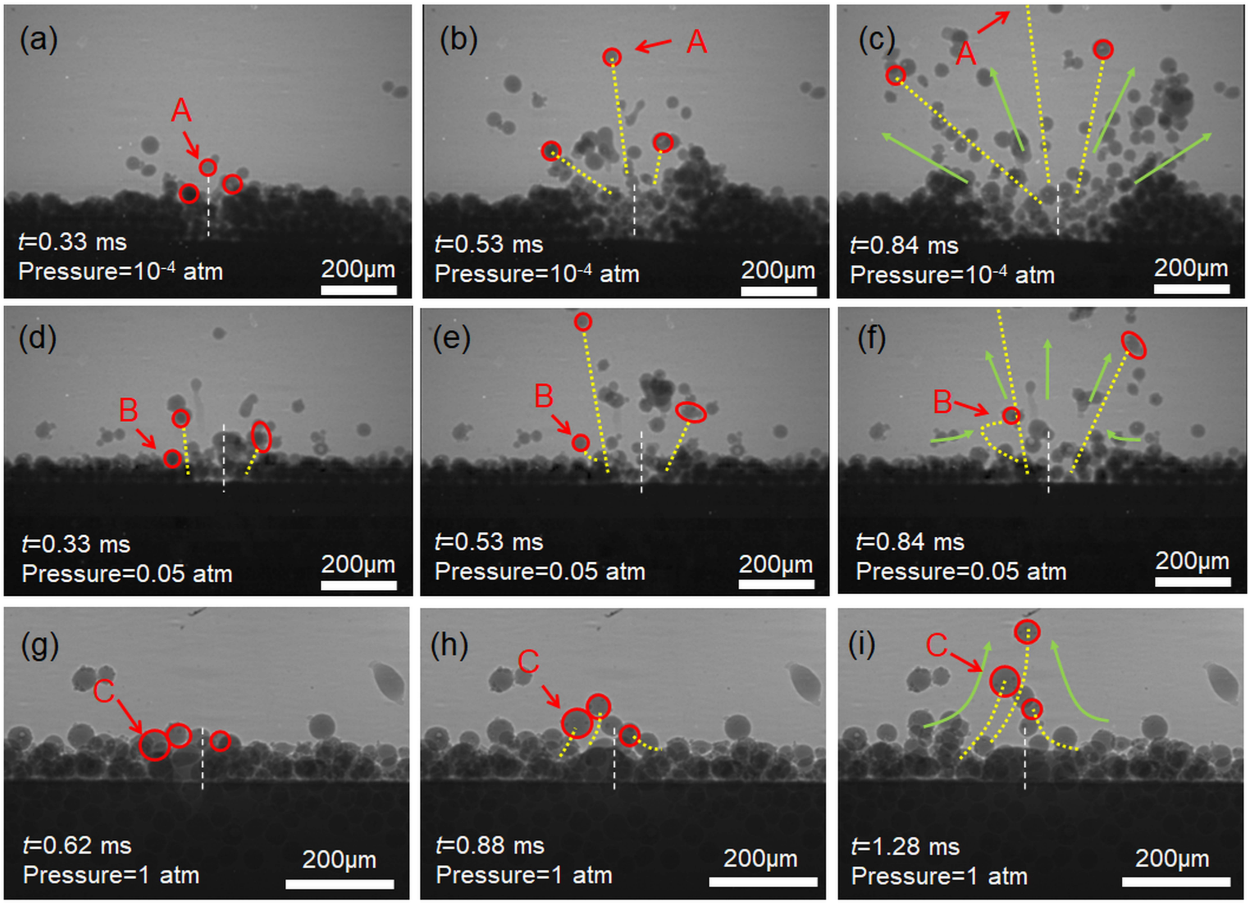

Figure 3. Dynamic X-ray images showing powder motion at different moments and under different environmental pressures. Original figure from [43].

Under vacuum (a–c), the particles surrounding the melt pool were directly ejected away with a large divergence angle. Under 0.05 atm (d–f), most particles surrounding the melt pool were repelled with a smaller divergence angle than under vacuum. Several particles (for example, particle B), ejected with an initial large divergence angle, were reversed soon after and merged into the majority particle stream. In the case of 1 atm, the particles were first ejected away from the melt pool, but the ejection amount is much smaller than that of low environment pressures. Then, the particles surrounding the melt pool moved toward the melt pool and formed a narrow stream flowing upward (g–i).

The results in Figure 3 demonstrate that environment pressure influences particle moving behavior regarding the spattering divergence angle, spatter amount, and spatter speed.

3.1.2 Initiation of Powder Motion

Figure 3 only depicts the powder movement out of the powder bed. How the powder spattering initiates cannot be seen clearly at the frame rate of 54310 fps. To look into more details of the transient particle motion initiation, X-ray images of high frame rate (135776 frames per second) zooming in the laser-particle interacting region with stationary laser beam melting under vacuum were recorded and displayed in Figure 4. The laser was on at t = 0 μs (judging from the particle vibration), as shown in Figure 4(a). After t = 22 ± 7 μs, the particle beneath the laser beam started to change in geometry at the top surface (highlighted by yellow dashed lines), indicating the beginning of melting, as shown in Figure 4(b). Vaporization began at another 22 ± 7 μs since particle melting (t=44 ± 7 μs in total since laser on) when particles A and B started one-way movement out of the powder bed, possibly driven by vapor pressure, as shown in Figure 4(c). At the same time, the (partially) melted regions of several particles beneath the laser beam joined together and became an early form of a melt pool. As the melt pool grew and consumed the particles it touched, a complete form of the melt pool with a depression zone penetrating the substrate at t=265 μs showed up in Figure 4(d). The bottom of the depression zone, where the recoil pressure from vaporization is the highest, indicates the position of the laser beam. (The laser beam was placed off center so the movement of particles surrounding the melt pool can be observed.) Note that particles A and B were ejected out of the view.

These high frame rate results uncover the details of the powder spattering initiation process. At the initial stage of powder movement, the laser first melts the powder and forms the molten pool. Then, vaporization begins, and the surrounding particles are later ejected from the powder bed.

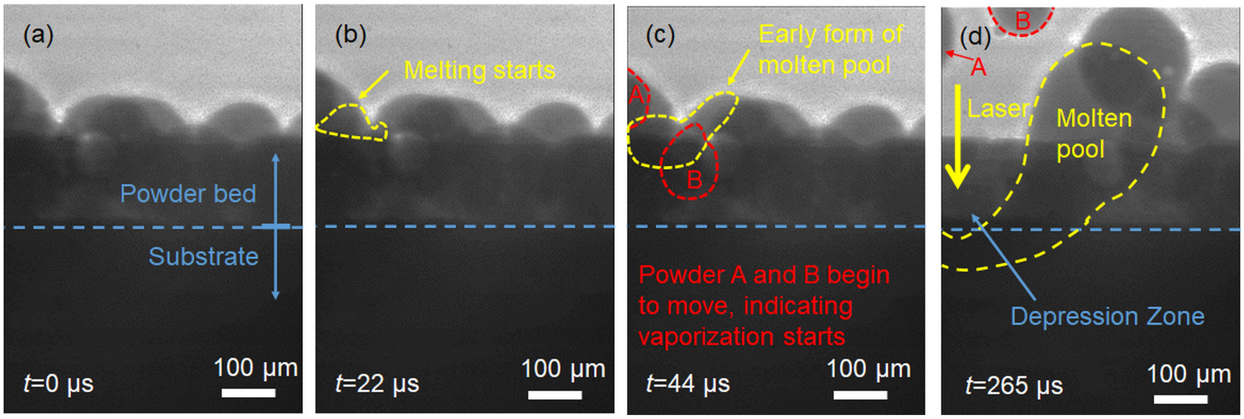

Figure 4. Dynamic X-ray images displaying transient melting and vaporization under vacuum during stationary laser beam melting. Original figure from [43].

3.1.3 Mechanism of Powder Motion as a Function of Time and Environment Pressure

Based on the above observations and inspired by previously published works [93,94], a clear schematic map showing the dynamics and mechanisms of powder motion during the LPBF process as a function of time and pressure was constructed and displayed in Figure 5. Schematics along the horizontal axis depict the transient evolution of laser melting, vaporizing, and the formation of argon gas flow, while those along the vertical axis show the effect of environment pressure on powder spattering behavior.

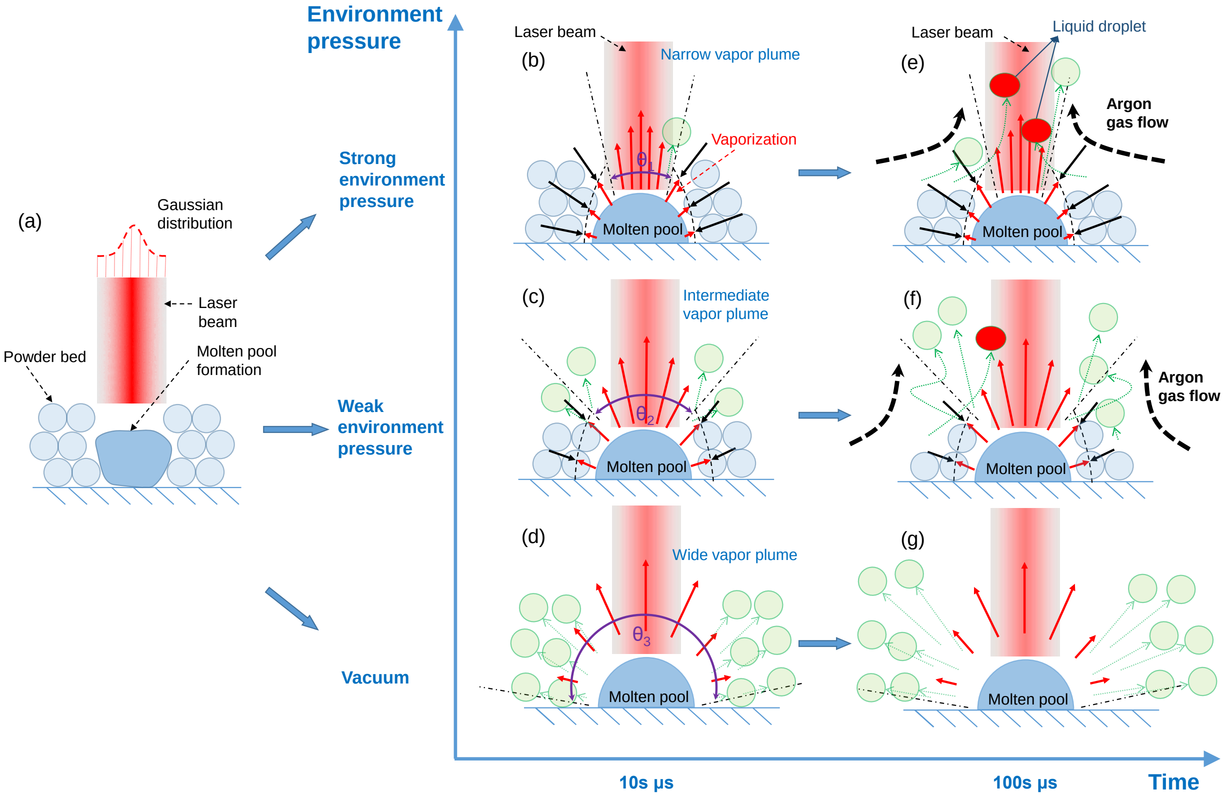

Figure 5. Schematic map of powder spattering behavior as a function of time and environment pressure. Original figure from [43].

When the laser is turned on, the Gaussian beam heats up and melts particles in a localized area under laser irradiation, as shown in Figure 5(a). Within a very short period, the vaporization is not significant. As soon as the melt pool surface temperature reaches the boiling point of the material, vaporization becomes intense. When vapor pressure is strong enough, the particles get ejected away from the melt pool, as shown by the second column in Figure 5.

Under vacuum, the metal vapor expands freely and, thus, ejects particles within a large divergence angle, as indicated by θ_3 in Figure 5(d). The ejected particles are colored green in the schematic. If there is argon gas in the environment, the escaping vapor must fight the confinement from environment pressure. After a short period (10s μs in this study), the melt pool is generated, and the vapor pressure accumulates and exceeds the environment pressure; then, the metal vapor breaks out and forms a vapor jet. The vapor jet originates at the top of the melt pool, where vaporization is the most intense due to Gaussian beam heating. The intensity of the environment pressure determines the divergence angle of the vapor jet, i.e., a stronger environment pressure results in a narrower vapor jet, as indicated by $\theta_1 < \theta_2$ in Figure 5(b–c). Since the particles in the path of the vapor jet will be ejected, a larger vapor jet divergence angle leads to more powder spattering. Therefore, higher environment pressure can potentially mitigate the powder spattering.

To confirm the effect of the environment pressure on the total spattering, two stationary laser melting tests were carried out on a 304L stainless steel powder bed with the same layer thickness (136 μm) but under different environment pressures: 0.0002 atm and 0.1 atm. The laser power was 260 W with a $1/e^2$ diameter of 100 μm and a duration of 1 ms for both tests. The experimental results are shown in Figure 6. The position of the laser is pointed out by red dashed lines. After the laser was on for 0.22 ms, the spattering particles above the powder bed were counted to be ~120 under 0.0002 atm and ~50 under 0.1 atm, which shows a significant decrease in the amount of powder spatter under relatively high environment pressure.

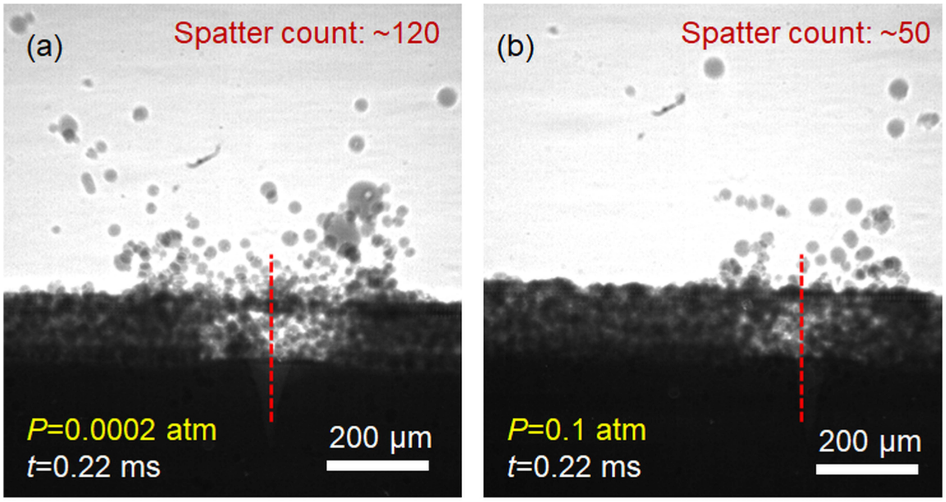

Figure 6. X-ray images showing spatter amount as a function of environment pressure. The powder bed thickness was kept the same between the two experiments. Original figure from [43].

Argon gas flow begins after the vapor jet forms for a certain period (100s μs in this study), following the vapor jet-induced horizontal pressure difference due to the Bernoulli Effect, as shown by schematics in Figure 5(e–f). The gas flow entrains particles in the flow path toward the melt pool, whether they are initially on the powder bed or have been ejected out of it. Some high-speed particles can fly close to the center above the melt pool and be heated up by the laser, metal vapor, or plasma [93] and thus become hot spatters. The hot spatters are colored in red in the schematics. The amount of hot spatter depends on the environment pressure. Higher environment pressure can generate stronger gas flow, which thrusts more particles into the central area above the melt pool. However, although the high environment pressure promotes the generation of hot spatter, the amount of overall spatter (both cold and hot) is still reduced, as demonstrated in Figure 6. When the argon gas is absent (vacuum) in the environment, there is no gas flow to entrain the particles toward the melt pool. The metal vapor keeps expanding freely and ejects all the particles in the vapor path away from the melt pool, as shown in Figure 5(g).

The schematic powder motion map illustrates the phenomena and mechanisms of the powder motion behavior as a function of time and environment pressure during laser melting. When there is argon gas in the environment, laser melting, metal vapor jet, and argon gas flow occur in order. The total spatter amount depends on the divergence angle of the metal vapor jet, and the hot spatter amount depends on the intensity of the argon gas flow, both of which depend on the environment pressure. Under vacuum, the argon gas flow is not generated, and the surrounding particles are all ejected by freely expanding metal vapor.

3.2 Powder Dynamics as a Function of Location

Stationary laser melting experiments enabled the analysis of the mechanisms of powder spattering formation during laser melting. However, in the LPBF process, the laser beam moves with a certain scanning speed. To answer how particles at different locations move during laser scanning, laser single-track scanning experiments were performed. To get better X-ray transparency beneath the powder bed, AlSi10Mg was used for single-track scanning experiments. The results are shown in Figure 7.

The laser beam scanned from left to right with a laser power of 416 W and a scanning speed of 0.5 m/s. Powder moving behavior varies at three different locations along the laser scan path. Location 1 (vapor jet domain) is around the laser beam. The particles at location 1 moved away from the laser-powder interaction spot. Red circles indicated the representative particles. White dashed arrows marked the trajectories of the particles. Location 2 (argon gas domain) is behind the laser beam. Most of the particles at location 2 moved toward the laser-powder interaction spot. The representative particles were marked by yellow circles with their trajectories highlighted by green dashed arrows.

Location 3 is ahead of the laser beam. Powder moving behavior at location 3 depends on the processing parameters. Under the present experiment parameters, the particles at location 3 did not travel long distances. The pile of particles ahead of the laser beam only tended to incline towards the laser beam.

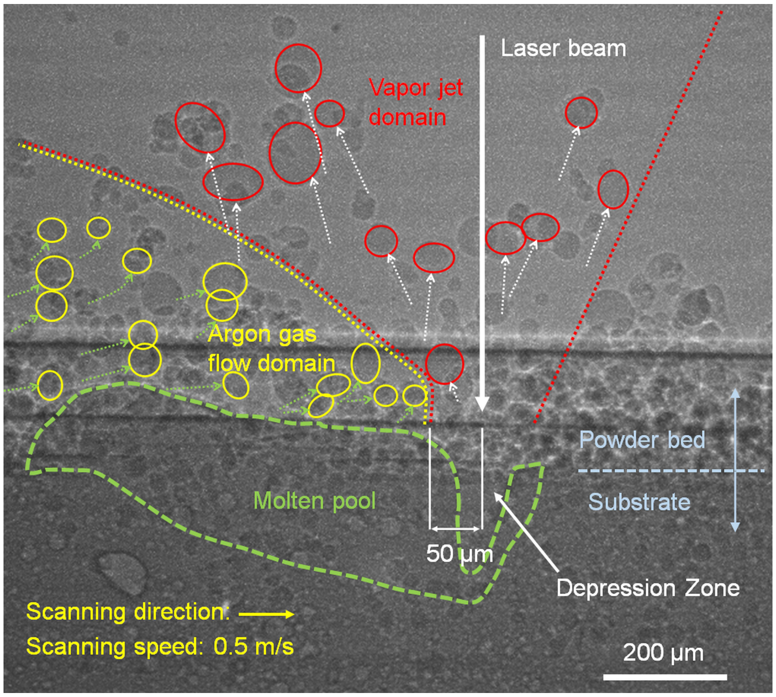

Figure 7. X-ray image of powder spattering during single-track laser scanning under 1 atm. Original figure from [43].

Based on the powder spattering mechanism illustrated in Figure 5, the vapor jet was the driving force that ejected the particles at location 1. At the same time, it was argon gas flow that entrained the particles at location 2 toward the laser-powder interaction spot.

Compared with the stationary laser melting tests, the relative position of vapor jet and argon gas flow during single-track laser scanning differs. In stationary laser melting, the laser beam is the symmetry axis of both vapor jet and argon gas flow. During laser scanning, the vapor jet region still surrounds the laser beam, but the argon gas flow region shifts backward to the laser scanning direction because it takes time for the argon gas flow to form.

3.3 Quantification of the Vapor-Driven Powder Dynamics

To further understand the powder spattering behavior, quantitative analysis was carried out on the results. Specifically, particle moving speed, acceleration, and the driving force for powder motion were calculated. The details are discussed below.

3.3.1 Quantification of Metal Vaporization Induced Powder Motion

By recording particle locations at different moments, the particles' speed (projectional moving velocity) can be calculated from the first derivative of displacement as a function of time. The speed of particle A in Figure 3(a–c) under vacuum is shown in Figure 8(a). The particle started to move at *t* = 0.3 ms (laser was on at t=0 ms and lasted for 1 ms) and reached up to 1.71 m/s at *t* = 0.76 ms before moving out of the view. As discussed in the schematic map, particle A was driven by the vapor plume [mechanism shown in Figure 5(d, f)]. The slope of the speed curve in Figure 8(a) decreases with time, indicating the influence of the vapor plume weakens when the particle moves away from the melt pool. The maximum acceleration during the particle movement is estimated by the derivative of the fitting equation at the initial moment, with a value of $a_{t=1.3}$= 12010 m/s^2. The driving force of the particle ejection can be calculated by Newton's second law:

$$\Delta \mathrm{P} = \frac{\mathrm{ma}}{\mathrm{A}} = \frac{\rho \mathrm{V} \cdot \mathrm{a}}{\mathrm{A}} = \frac{\rho \cdot (\frac{4}{3}\pi \mathrm{r}^3) \cdot \mathrm{a}}{\pi \mathrm{r}^2} = \frac{4}{3}\rho \cdot \mathrm{r} \cdot \mathrm{a} \qquad \text{Eq. 1}$$

where *m* is the mass of the particle, a is the acceleration of the particle, *A* is the cross-section area of the particle, *ρ* is the density of the particle, *V* is the volume of the particle, and *r* is the radius of the particle. Taking ρ = 7980 kg/m^3, *r* = 40 μm, a = 12177 m/s^2, the driving force for particle A was calculated to be 5111 Pa, which is the pressure drag induced by metal vapor flow.

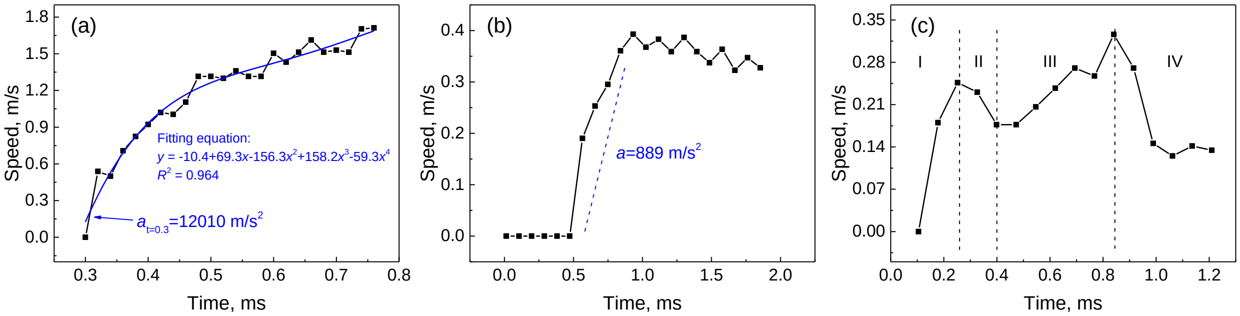

Figure 8. Powder moving speed as a function of time during stationary laser beam melting at different environment pressures. (a) Moving speed of powder driven by metal vapor plume under vacuum (10^{-4} atm). The traced powder is powder A in Figure 3. (b) Moving speed of powder driven by argon gas flow under the environment pressure of 1 atm. The traced powder is powder C in Figure 3. (c) Moving speed of powder driven by co-action of metal vapor plume and argon gas flow under the environment pressure of 0.05 atm. The traced powder is powder B in Figure 3. Original figure from [43].

To be noticed, only the particles on the edge of the melt pool were selected for quantified analysis. The particles move in three dimensions, but only the two-dimensional projected particle motions can be observed from the video. The particles on the edge of the melt pool have a better chance of moving in the projection plane. Since the number of particles on edge is small (< 10), statistical analysis of particle movement during stationary laser melting was not conducted.

3.3.2 Quantification of Argon Gas Flow Induced Powder Motion

The speed of particle C in Figure 3(g–i) is shown in Figure 8(b). As discussed in Figure 5(b, e), particle C is driven by vapor jet-induced argon gas flow. The movement started at *t* = 0.47 ms (laser is on at *t* = 0 ms and lasts for 1 ms) and reached the peak speed of 0.39 m/s at *t* = 0.93 ms; then the speed dropped to 0.33 m/s till *t* = 1.86 ms before the particle moving out of the view. The speed dropped because the laser was off at t = 1 ms. The vaporization vanished and stopped generating argon gas flow. The acceleration at the speed-increasing stage was estimated by the slope of the curve, which is a = 889 m/s^2. Both the peak speed and the maximum acceleration of particle C are lower than particle A, indicating that the intensity of argon gas flow is lower than the vapor plume/jet. Substituting a = 889 m/s^2 into Eq. *1*, the driving force of particle C is calculated to be 378 Pa, which is only about 1/14 of the particle driving force induced by metal vapor flow (5111 Pa).

3.3.3 Powder Motion Induced by a Combination of Metal Vapor and Argon Gas Flow

Figure 8(c) shows the speed variation of particle B in Figure 3(d–f) as a function of time that separates into four stages as marked by I–IV. As revealed in Figure 5(c, f) from the schematic map, under weak environment pressure, particles at feasible positions can be first ejected by the vapor and get reversed by the argon gas flow. Different stages of this process are reflected in the speed variation. In stage I, the particle was ejected and accelerated by the vapor plume. After about 150 μs, the argon gas flow formed gradually and moved against the particle movement. The argon gas flow first decelerated the particle (stage II) and later accelerated the particle back to the laser beam (stage III). In the end, the vapor pressure faded due to the particle moving far from the melt pool, as well as the laser turn-off. Therefore, the particle moving speed decreased in stage IV. Although a relatively accurate quantification of acceleration and driving force cannot be carried out because of insufficient data points, it is evident that the slope of the curve at stage I is higher than the slope of stage III, indicating that the driving force in stage I was stronger than that in stage III. Since the particles were carried by vapor jet at stage I and by argon gas flow at stage III, this result is consistent with the results in Sections 3.3.1 and 3.3.2.

3.3.4 Statistics of Powder Motion During Laser Single Track Scanning

The speed, acceleration, and driving force of ten particles in the vapor jet domain and ten particles in the argon gas flow domain from Figure 7 are analyzed and shown in Figure 9. Figure 9(a) shows the speed of the particles driven by the vapor jet, with the peak speed varying in a range of 0.75–2.24 m/s, within 1.14 ms. Note that the start time of each of the particles was set to zero. The accelerations are estimated by the slope of the rising stage in each curve and vary in a range of 2000–13900 m/s^2 with a median of 7600 m/s^2, as shown in Figure 9(b). The driving force is calculated based on Eq. *1*, with $\rho = 2670\ kg/m^3$ for AlSi10Mg particles. The results are shown in Figure 9(c) within a range of 121–931 Pa and a median of 348 Pa.

Figure 9(d) shows the speed of 10 particles moving in the argon gas flow region. The peak speed varies between 0.27–0.61 m/s within 2.88 ms. The accelerations of the ten particles range between 552–1494 m/s^2, with a median of 1140 m/s^2. The corresponding driving forces were calculated to be within 29–75 Pa, with a median of 48 Pa.

Considering the overall movement of each set of the ten particles, the speed of particles driven by the vapor jet is about three times as large as particles driven by argon gas flow. The acceleration and driving force of vapor-driving particles are one order of magnitude larger than argon gas flow-driven particles. The distinct difference in particle movement proves the existence of two driving forces and indicates a stronger intensity of vapor jet than argon gas flow.

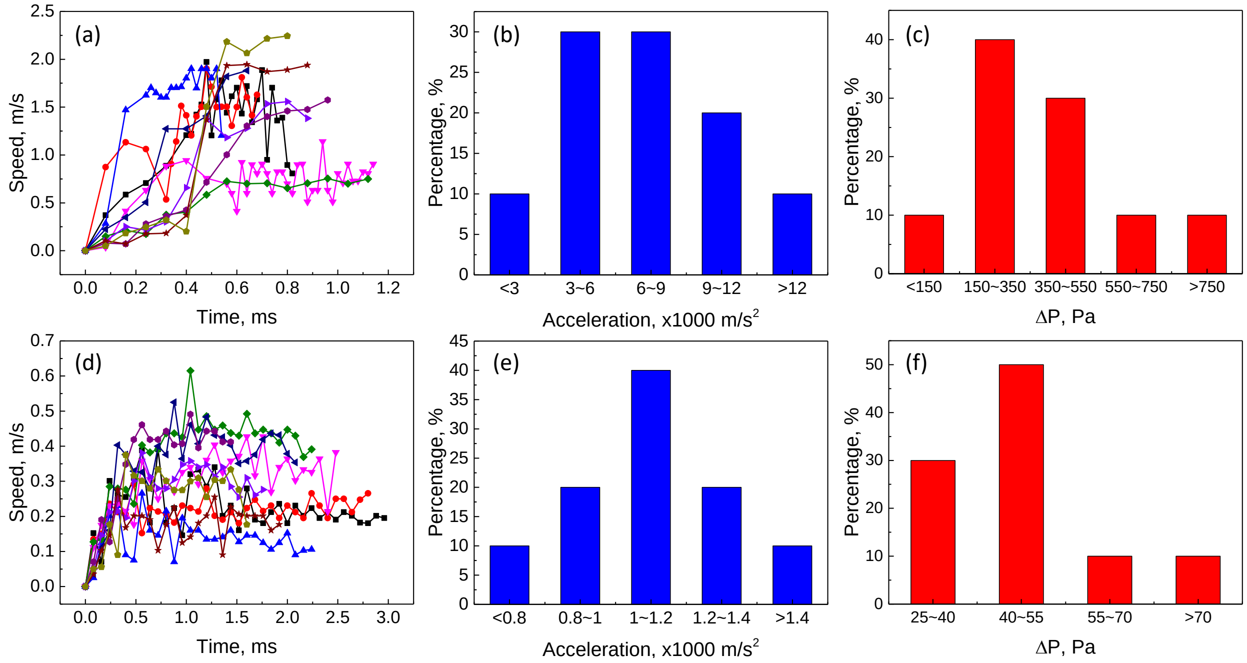

Figure 9. Quantification of speed, acceleration, and driving force of powder movement during laser single track scanning under 1 atm. (a) Moving speed of particles driven by vapor jet. Ten particles are shown. The time axis is the travel time for each particle, not the time elapsed in the X-ray video. (b, c) Acceleration and effective driving pressure for particles in vapor jet region. (d) Moving speed of particles driven by argon gas flow. Ten particles are shown. (e, f) Acceleration and effective driving pressure for particles in argon gas flow region. Original figure from [43].

3.3.5 Quantification of Angular Powder Velocity Profile Driven by Metal Vapor

To quantify the spatial distribution of powder moving velocity, an experiment was designed to track the particle moving trajectories in each direction simultaneously. Figure 10(a) shows the schematic of the experiment setup. The powder bed consists of two glassy carbon walls and a substrate. The two glassy carbon walls are higher than the powder bed surface of the standard samples. Small 316L stainless steel powders were attached to one of the walls by van der Waals force [95] to trace the vapor velocity profile. The size distribution is shown in Figure 10(c). Note that the glassy carbon is transparent under X-ray. Thus only the powders can be observed in the X-ray image. The laser beam was aimed close to the wall with powder so that the powder movement could reflect the metal vapor movement at the largest vertical cross-section. Figure 10(b) gives a schematic showing how the powders on the wall are being pushed away by the metal vapor.

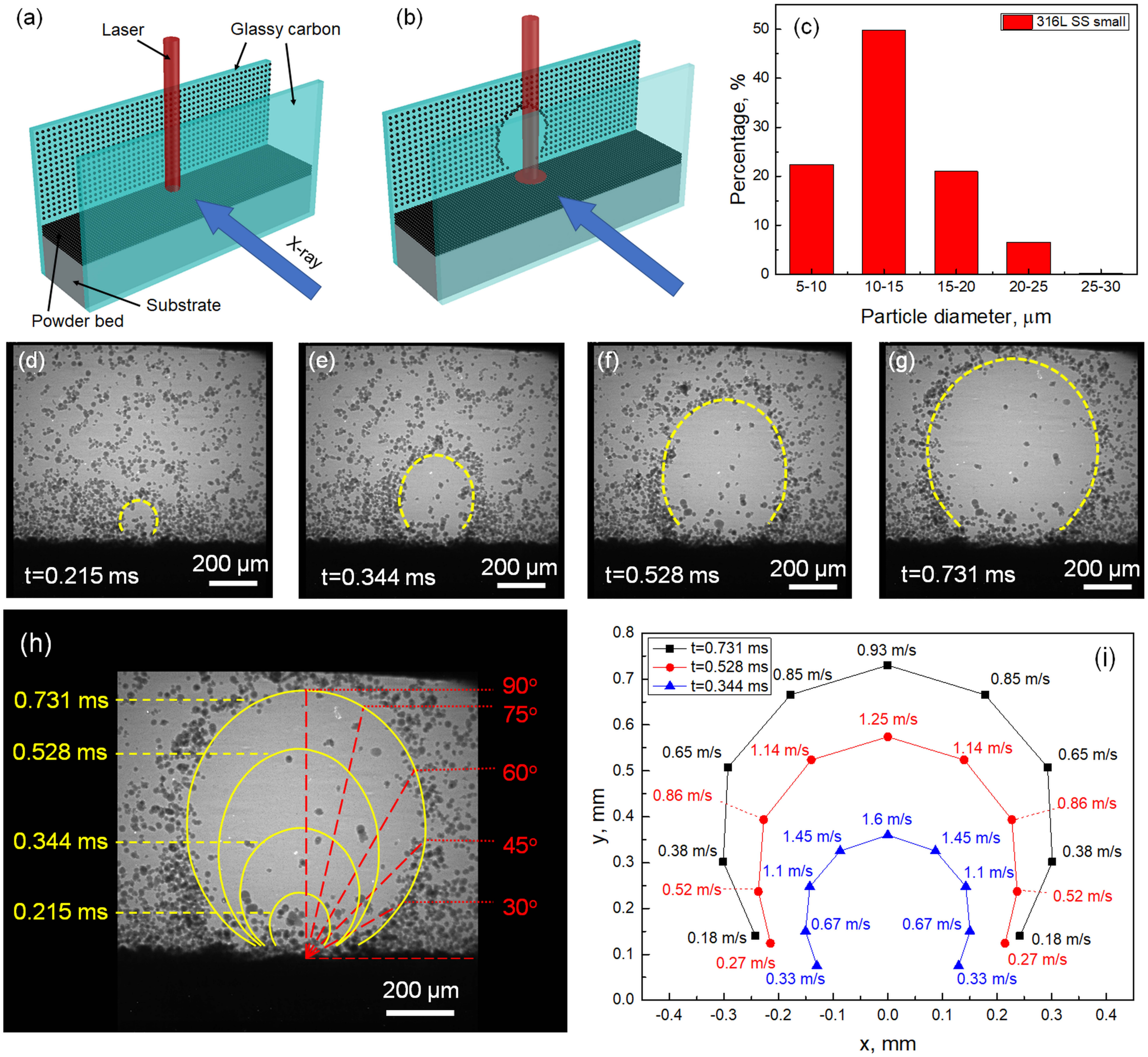

Figure 10. Quantification of angular powder velocity profile driven by metal vapor. (a) Schematic showing the sample design for tracing powder velocity profile. (b) Schematic showing how the powders move during laser radiation. (c) Histogram showing the distribution of small 316 L stainless steel powder used for this experiment. (d–g) X-ray images indicating the profile of powder moving front. The laser is on at t = 0 ms. The experiment was under a vacuum (0.0001 atm). (h) Schematic indicating the angular

powder tracing path (red line) at different moments. (i) The angular powder velocity distribution along the powder moving front as a function of time. Original figure from [43].

Figure 10(d–g) shows the powder moving front during laser melting. The laser power is 312W. The laser was turned on at t=0 ms. When the vaporization begins, the metal vapor will push the powders away. The experiment is carried out under a vacuum (0.0001 atm) to prevent the generation of argon gas flow. Yellow dashed lines in the figures marked the powder moving front at different moments.

To calculate the powder velocity spatial distribution, five angles were chosen to indicate the trend of angular velocity variation: 30°, 45°, 60°, 75°, and 90° to the powder bed surface (horizontal direction), as shown in Figure 10(h). The powder velocities at each angle were calculated to generate the angular powder velocity distribution along the powder moving front at different moments, as shown in Figure 10(i). The three curves represent the particle moving front at the moment of 0.344 ms, 0.528 ms, and 0.731 ms, respectively.

The angular distribution of particle moving velocity can be evaluated by comparing data points within each curve in Figure 10(i). It shows that the velocity at a higher angle to the powder bed surface is larger than at a lower angle. The maximum velocity appears at the center of the powder moving front. For all three moments, the maximum velocities are about five times as high as the minimum velocities (at 30°).

Comparing the velocity values between the three curves at the same angle, the velocity decreased during the period of 0.344–0.731 ms. Since the gravity and friction are almost constant, the particle velocity decrease may result from the attenuation of the expanding metal vapor.

3.3.6 Role of Gravity

In this study, the driving force of particle movement was identified as pressure drag. This is only valid when gravity can be ignored. Gravity can be considered as a force applied at the center of the particle, pointing vertically down to the ground. Therefore, the effect of the gravity is equivalent to a pressure of:

$$P_{eq} = \frac{mg}{A} = \frac{\rho V \cdot g}{A} = \frac{\rho \cdot (\frac{4}{3}\pi r^3) \cdot g}{\pi r^2} = \frac{4}{3}\rho \cdot r \cdot g \qquad \text{Eq. 2}$$

where m is the mass of the particle, g is the gravity, A is the cross-section area, V is the volume of the particle, r is the radius of the particle, ρ is the density of the particle. Taking r = 40 μm for example, P_{eq} = 4.2 Pa, which is only 1.1% of the particle driving force induced by gas flow, and 0.08% of the particle driving force induced by metal vapor flow. Thus, the influence of gravity can be ignored at the particle accelerating stage.

3.4 Effect of Spattering on Part Quality

To investigate the effect of spatters on the part quality, the morphology of a single laser scan track on the AlSi10Mg sample was characterized by an optical microscope after the in-situ X-ray imaging experiment. The loose powders on the sample were blown away by compressed air before taking optical images. The track's top and side views are shown in Figure 11(a) and (b), respectively. It was observed that some particles were sintered on the track. One typical type of residual particles are the solidified liquid spatters, as pointed out by red circles. The size of the liquid spatter can be much larger than the size of raw powders. When some cold particle spatters (same size as raw powder) enter the laser beam region, the particles can be melted into small droplets. The large liquid spatters can form by the collision of small droplets. The solidified large spatters can cause defects in the as-built part because (1) the spatters may carry a high level of oxygen content, which reduces the wetting of the substrate [96]; (2) the large spatter may not be fully melted during laser scanning, thus become potential sites of pore generation [97].

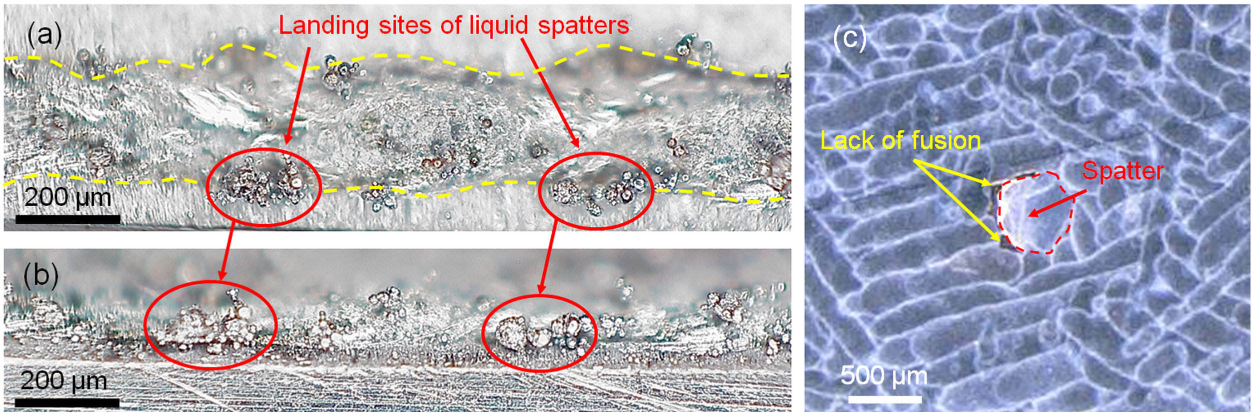

Figure 11. Optical images showing the influence of spatters on the defect formation in additively manufactured AlSi10Mg part. Original figure from [43].

The evidence of spatter-induced defects in the as-built part was found in the AlSi10Mg built by a commercial metal AM machine, as shown in Figure 11(c). The building direction is perpendicular to the view. A spatter is pointed out in the view with the boundary highlighted by red dashed line. The spatter size can be much larger than the raw powder (~30 μm). A string of lack-of-fusion pores was generated around the spatter, which is clear evidence of spatter-caused defects.

3.5 Potential Ways to Mitigate Powder Spattering

Based on the understanding of transient powder dynamics, several potential ways that could mitigate powder spattering are proposed below.

3.5.1 Pre-Sintering the Powder Bed

As revealed in Figure 4, there is a time window for the metal vapor to grow strong enough to eject the powder away after the laser melting. Therefore, if the laser duration time is within the time window, it is possible to pre-sinter the powder bed using a laser without inducing significant powder ejection, similar to the pre-sintering process in the electron beam melting (EBM process [98–100]). The time window can be extended by applying a laser beam with a lower energy density. Hence, reduced laser power or a larger laser beam is suggested for the pre-sintering process.

3.5.2 Tuning the Layer Thickness

Tuning the layer thickness can be an effect way to mitigate powder spattering. As illustrated by the schematic map, the vapor jet has a shape of an inverted cone that is more confined near the molten pool but expends when jetting away from the molten pool. Therefore, a thinner powder bed has a better chance of fully melted by the laser and leaving fewer loose powders in the vapor jet path to be ejected.

Evidence was found to confirm the effect of layer thickness by comparing AM parts built with different layer thicknesses. Two AlSi10Mg samples were built in a commercial AM machine with 50 μm and 30 μm layer thickness, respectively. Cross-sections of the two samples were cut perpendicularly to the building direction. The optical images of the two cross sections are shown in Figure 12. The spatter-caused pores can be found in the sample built with a thicker layer (50 μm), as indicated in Figure 12(a). However, the spatter-induced defects were not observed in the sample built with a thinner layer (30 μm), as shown in Figure 12(b). The densities of the two samples also support the above observation. The 50 μm layer sample has a density of 2.5648 g/cm^3, which is lower than the density of the 30 μm layer sample (2.6629 g/cm^3).

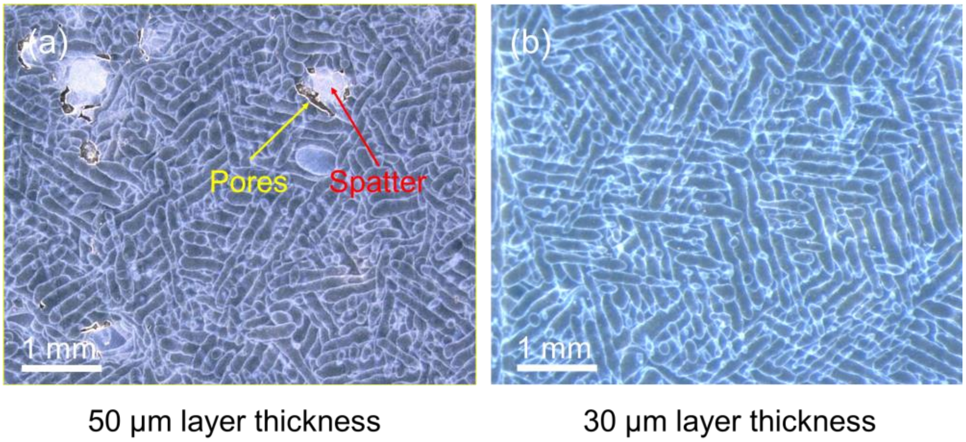

Figure 12. Optical images displaying the effect of powder layer thickness on the microstructure of additively manufactured AlSi10Mg parts. The building directions are perpendicular to the view. Original figure from [43].

3.5.3 Tuning the Environment Pressure

As demonstrated in Figure 6, the hot spatter amount increases with the rise of environment pressure, while the total spatter amount drops with the increase of environment pressure. Hence, the environment pressure can be tuned to balance the amount of hot spatter and total spatter to improve part quality.

3.6 Summary and Conclusions

A detailed study was conducted on the mechanisms/quantification of transient dynamics of powder spattering as a function of time, environment pressure, and location in the LPBF process by in-situ high-speed high-energy X-ray imaging. The major conclusions of this study are as follows:

(1) During laser heating, localized laser melting happens first, followed by the

generation of an intensive vapor jet. Then, the argon gas flow appears. The time for each step was estimated for the laser melting condition investigated in this work: microseconds for melting, tens of microseconds for vapor jet/plume formation, and hundreds of seconds for argon gas flow formation.

(2) The environment pressure influences the powder spattering behavior by controlling the divergence angle of the vapor jet and the argon gas flow. The amount of total spatters (both cold and hot), dominated by the divergence angle, drops with the increased environment pressure. The amount of hot spatters, dominated by argon gas flow-induced entrainment, increases with the increase of environment pressure.

(3) Powder spattering behavior during single-track laser scanning varies with location. Powder spattering around the laser beam is driven by a vapor jet. Particles in the region behind the laser beam are entrained by the argon gas flow. Particles ahead of the laser beam are also affected by argon gas flow. But long-distance particle movement is not observed under the processing conditions in this work. The vapor jet and argon gas flow are not symmetrical to the laser beam during single-track laser scanning. The argon gas flow falls behind the laser beam because the formation of argon gas flow takes time.

(4) Quantification of powder dynamics shows that particles driven by vapor jet have a moving speed three times as large as particles driven by gas flow; the acceleration and driving force of vapor-driven particles are one order of magnitude larger than argon gas flow-driven particles.

(5) Based on the understanding of the transient powder dynamics from this study, it is

proposed that pre-sintering the powder bed, tuning layer thickness, and tuning environment pressure could potentially mitigate powder spattering.

Chapter 4: Melt Pool Variation under Constant Input Energy Density

---

This chapter contains experimental data and results that have been published in the following work:

Q. Guo, C. Zhao, M. Qu, L. Xiong, L.I. Escano, S.M.H. Hojjatzadeh, N.D. Parab, K. Fezzaa, W. Everhart, T. Sun, L. Chen, In-situ characterization and quantification of melt pool variation under constant input energy density in laser powder bed fusion additive manufacturing process, Addit. Manuf. 28 (2019) 600–609. [37]

The publication rights for this section are given in Appendix A. Appropriate recognition is given to the relevant citation for the material in which it was originally published. The presented material represents my contributions and material collected with or by a collaborator has been highlighted as such.

This chapter reports the direct observation and quantification of melt pool variation during the LPBF process via in-situ high-speed high-energy X-ray imaging. It is demonstrated that the melt pool can undergo different melting regimes, and both the melt pool dimension and the volume can have orders-of-magnitude change under a constant input energy density (IED). The mechanisms causing such dramatic melt pool variation under a constant IED are explored and discussed.

4.1 Experiment Design

To study melt pool variations under a constant IED level, laser single-track scan tests were carried out on an AlSi10Mg powder bed with five different combinations of laser power and laser scan speed under a constant IED level. The laser power increased from 104 W to 520 W with an increment of 104 W. Suitable laser scan speeds were calculated to maintain a constant IED. A total of three IED levels (260 J/cm^2, 520 J/cm^2, and 1040 J/cm^2) were tested to validate the phenomena. Detailed processing parameters and corresponding IED levels are listed in Table 1. To study the separate roles of laser power and laser scan speed, five laser single-track scan tests were conducted with a constant laser scan speed of 0.6 m/s and different laser powers of 208 W, 260 W, 312 W, 364 W, and 416 W. Four laser single-track scan tests were carried out with a constant laser power of 416 W and different laser scan speeds of 0.4 m/s, 0.8 m/s, 1.2 m/s, and 1.6 m/s.

Table 1. Processing parameters for laser single-track scan tests as functions of input energy density.

Input energy density (J/cm^2)	**Laser scan speed (m/s)**				
1040	0.1	0.2	0.3	0.4	0.5
520	0.2	0.4	0.6	0.8	1.0
260	0.4	0.8	1.2	1.6	2.0
Laser power (W)	104	208	312	416	520

In this work, the melt pool depth and length, as well as the depression-zone width and depth, will be measured from X-ray images. Since the solid-liquid interface in the original X-ray image is unclear, ImageJ was used to process all the images to enhance the contrast at the solid-liquid interface. As illustrated in Figure 13(a), the liquid-gas interface (i.e., depression zone boundary) clearly shows up in the original X-ray images, while the solid-liquid interface is unclear. After dividing the intensity at each pixel of Frame i by the intensity of corresponding pixels in Frame i+2, the solid-liquid interface is revealed, as shown in Figure 13(c). However, the post-processed images will lose the features of the substrate and powder bed. Moreover, the clarity of the depression-zone boundary suffers from the superposition of two frames. To keep all the information, the original X-ray images were presented with highlighted melt pool boundaries.

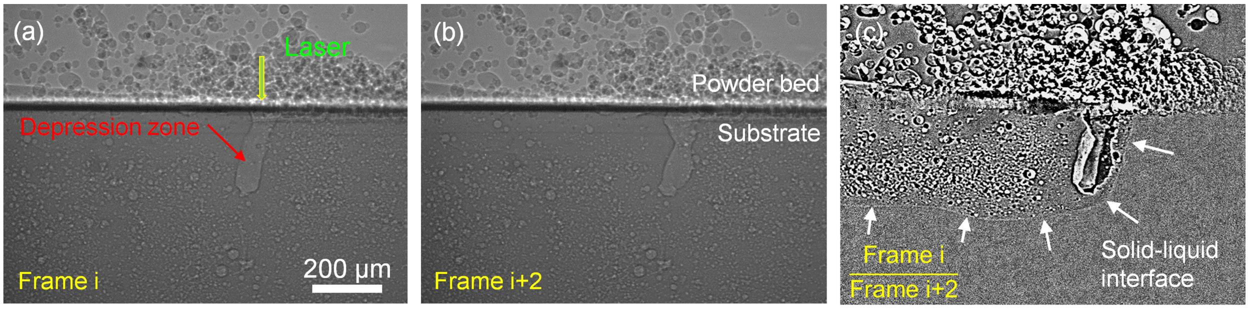

Figure 13. Image processing method to enhance melt pool boundary (solid-liquid interface). Original figure from [37].

The melt pool dimension values reported in the present work are the averages of the measurements from multiple frames. Depending on the period the melt pool stays in view, the number of images measured varies from 18 to 98. The corresponding standard deviations were also calculated and displayed as error bars when applicable. Since the apparent melt pool boundary and depression-zone boundary in X-ray images have a width of 2 pixels (4 μm), all measurements exhibit an inherent error of ±2 μm. The melt pool width was measured from the top view of a solidified track taken by a scanning electron microscope (Hitachi-S4700). A reported melt pool width is the average of 20 measurements along the solidified track (uniformly spaced, and leaving out 0.5 mm length at the beginning and the ending of the 2.5 mm-long track).

4.2 Melting Regime Change under Constant IED Level

X-ray images showing melt pool variations under three constant IED levels are displayed in Figure 14. Five combinations of laser power and scan speed were studied and are detailed in Table 1. The panels in Figure 14 display tests carried out with parameters arranged in the same order as in Table 1. The horizontal axis shows laser power, while the vertical axis shows the IED level. The corresponding scan speeds of each test are indicated in the bottom-left corner of the images. Outlines of the melt pool and the depression zone (cavity induced by the recoil pressure of metal vaporization) are highlighted by yellow dashed lines and red dashed lines, respectively.

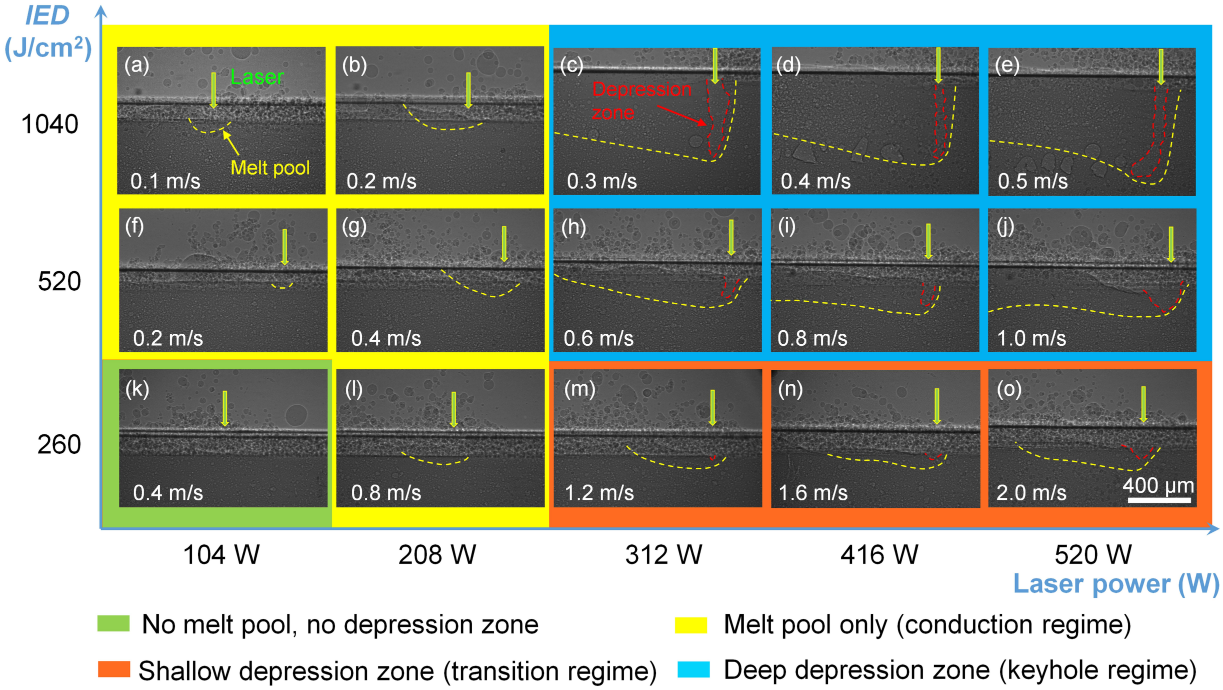

Figure 14. X-ray images showing melt pool variation under constant IED levels. Original figure from [37].

According to the presence and the geometry of the melt pool and depression zone, four regimes can be identified: (1) Neither the melt pool nor the depression zone appear, hereinafter referred to as no melt pool regime, as marked by green in Figure 14; (2) Only the melt pool appears, hereinafter referred to as no melt pool regime (namely "conduction regime" in the welding community), as marked by yellow; (3) Both the melt pool and the depression zone appear, and the 2D / W (depth over half width) ratio of the depression zone is less than 1, hereinafter referred to as shallow depression zone regime (namely "transition regime" in the welding community), as marked by orange; (4) Both the melt pool and the depression zone appear, and the 2D / W ratio of the depression zone is over 1, hereinafter referred to as the deep depression zone regime (namely "keyhole regime" in the welding community), as marked by blue. The no melt pool regime locates in the bottom-left corner of the figure. The absence of the melt pool and the depression zone in the no melt pool regime indicates that the energy absorbed by the material is insufficient under these conditions. The keyhole regime, located in the top-right corner of the figure, indicates that the absorbed energy is surplus and generates a deep depression zone. Below the keyhole regime, the transition regime is found in the bottom-right side of the figure, where the absorbed energy is relatively lower than that in the keyhole regime and results in a shallower depression zone. A conduction regime is mainly located on the left side of the area, surrounding the no melt pool regime, where the absorbed energy is intermediate, and only the melt pool is exhibited.

For each IED level, two or more melting regimes are observed. When simultaneously increasing laser power and scan speed, the melt regime changes from no melt pool regime to conduction regime to transition regime under the IED level of 260 J/cm^2, and changes from conduction regime to keyhole regime under IED levels of 520 J/cm^2 and 1040 J/cm^2. The change of melt regime indicates that a significantly different amount of energy was used for melting material under different combinations of laser power and scan speed within a constant IED.

Besides the melting regime variation within constant IED levels, the depression zone also undergoes variations in both size and shape under different processing conditions.

From the nine images in the transition regime and keyhole regime, the depression zone grows deeper at higher laser powers while tending to become wider at higher scan speeds.

4.3 Melt Pool Dimension Change under a Constant IED Level

The melt pool dimensions (length, depth, and width) and dimension ratios (length/width, length/depth, and width/depth) were measured and calculated for experiments conducted under various constant IED levels, as shown in Figure 15 and Figure 16, respectively. For each IED level, the laser power varies in a range of 104 W – 520 W with an increment of 104 W. The laser scan speed was altered simultaneously to maintain constant IED levels of 0.1–2 m/s.

The results show that all three dimensions of the melt pool exhibited a trend to increase, while the laser power and scan speed within the same IED were simultaneously increased, as depicted in Figure 15. The trend was confirmed under multiple IED levels (260 J/cm^2, 520 J/cm^2, 1040 J/cm^2). The length/width ratio and length/depth ratio presented in Figure 16 show an increasing trend, indicating that the melt pool prefers to elongate along the laser scan direction rather than spread in the transverse plane. This is because less time is permitted for heat transfer across the transverse direction at a higher laser scan speed. The width/depth ratio in Figure 16 exhibits a general trend to decrease at the conduction-transition regime (208–520 W for the IED of 260 J/cm^2, 104–312 W for IEDs of 520 J/cm^2 and 1040 J/cm^2), indicating that the melt pool prefers to penetrate the material rather than extend along the transverse direction when the laser power and laser scan speed within the same IED are simultaneously increased. The ratio remains stable in the keyhole regime (312–520 W for IEDs of 520 J/cm^2 and 1040 J/cm^2).

The overall trend for the width/depth ratio to decrease is mainly because the emergence of the depression zone will extend more energy beneath the surface.

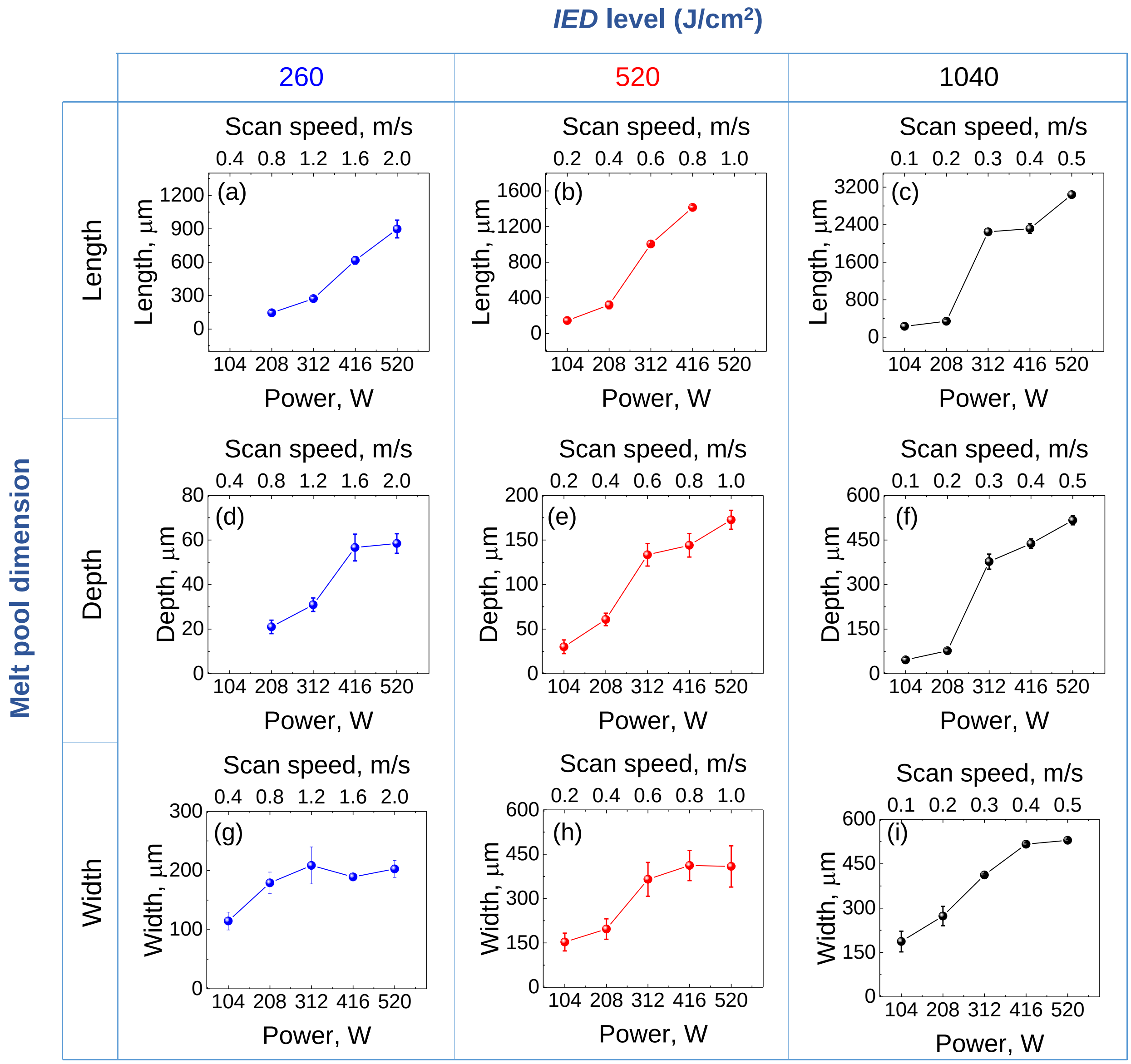

Figure 15. The melt pool dimension variations as functions of processing parameters under constant IED levels. Original figure from [37].

The significant variations in the melt pool dimensions and dimension ratios imply that a simultaneous change in laser power and scan speed under a constant IED would lead to a preferential dimension development rather than maintaining a consistent melt pool size or shape.

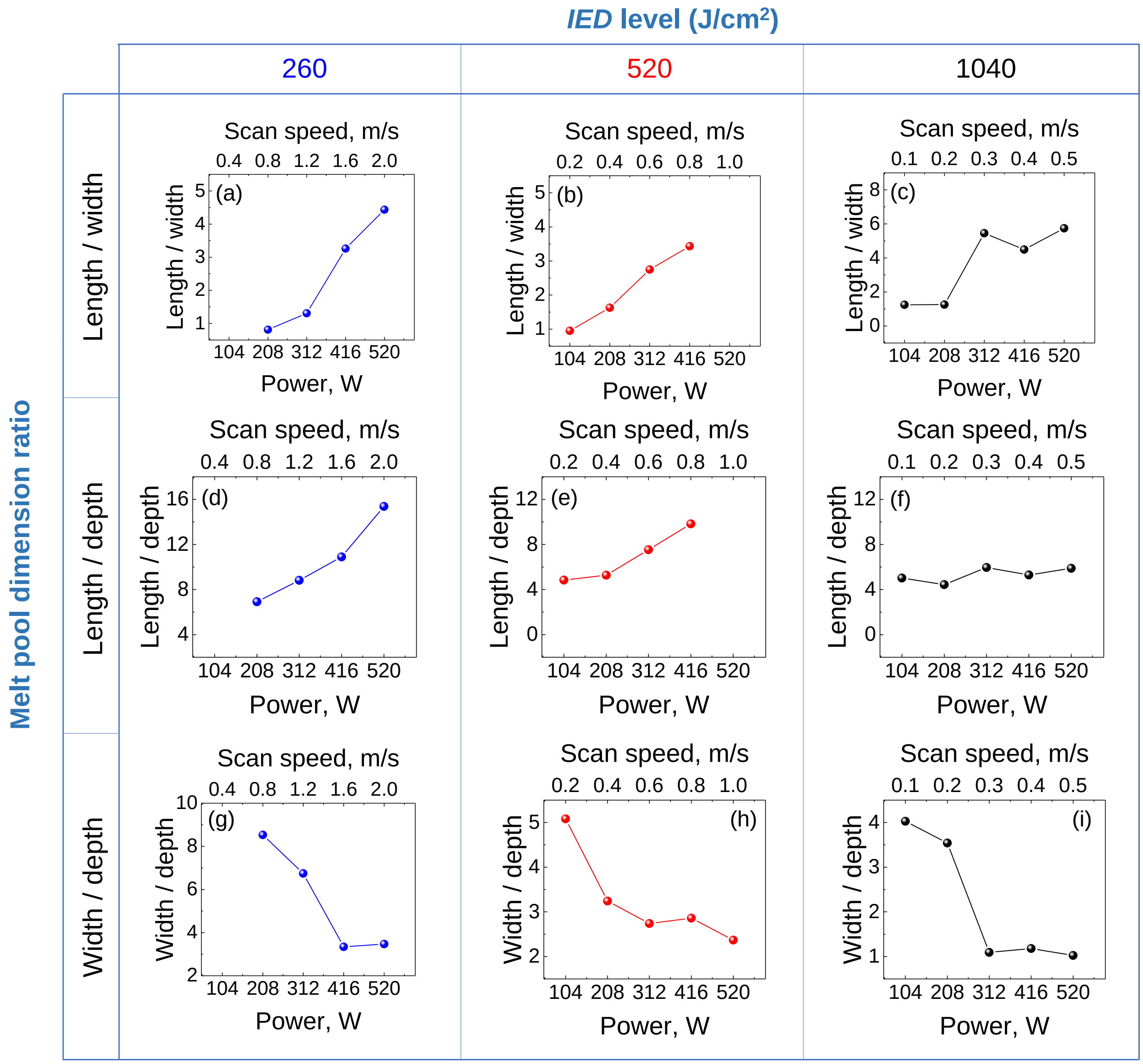

Figure 16. The melt pool dimension ratios as functions of processing parameters under constant IED levels. Original figure from [37]*.*

4.4 Melt Pool Volume Change under a Constant IED Level

The melt pool volume was calculated based on melt pool dimension measurements from X-ray images. To simplify the calculation of melt pool volume, the melt pool was divided into three regions, as shown in Figure 17(a): top melt pool (above the substrate, purple region), bottom melt pool (below the substrate, yellow region), and depression zone (orange region).

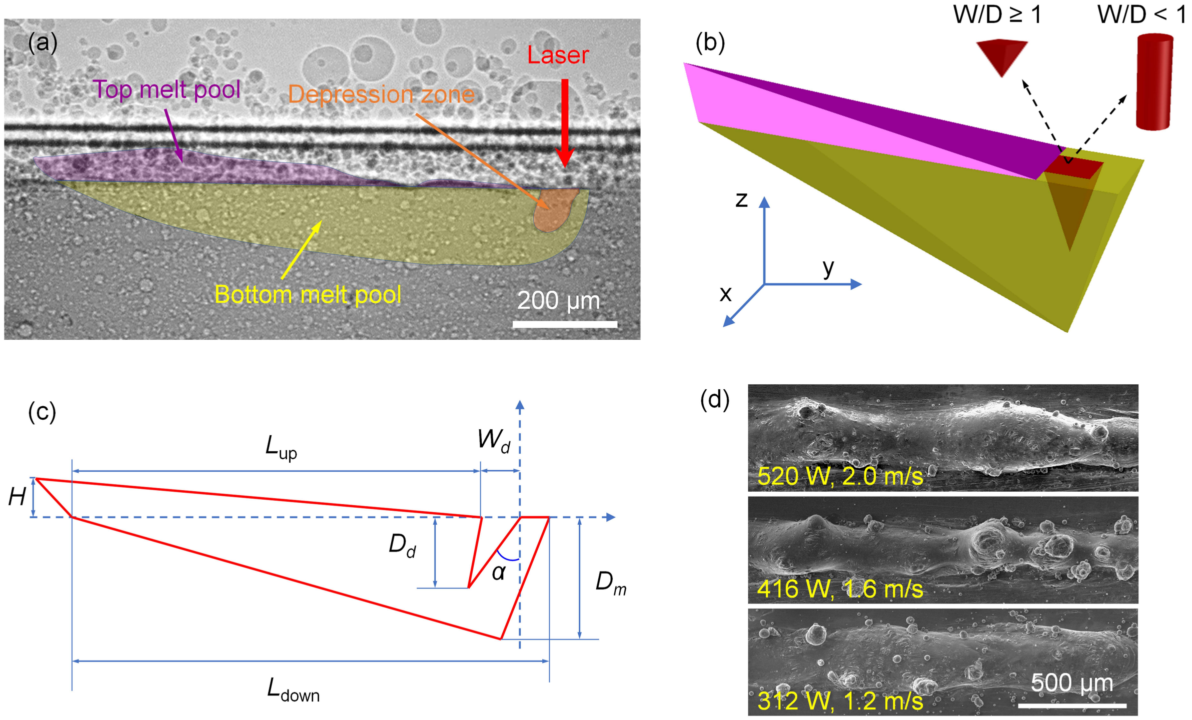

Figure 17. Calculation method for melt pool volume. (a) X-ray image showing the three regions in the melt pool. (b) Schematic showing the simplified three-dimensional model of melt pool geometry. The simplified geometry of the depression zone depends on the width/depth ratio. (c) Two-dimensional schematic showing the required dimensions for calculating the melt pool volume. (d) SEM images showing the top-view of three laser single scan track scan obtained with an energy density of 260 J/cm^2, with different combinations of laser power and scan speed. Original figure from [37]*.*

The melt pool volume is the sum of the top and bottom melt volume minus the volume of the depression zone. For fast calculation of melt pool volume, the top and bottom melt pools were treated as rectangular pyramids, as shown schematically in Figure 17(b). The shape of the depression zone depends on the width/depth ratio: when the W/D ⩾ 1, the depression zone was treated as a rectangular pyramid; when the W/D < 1, the depression zone was treated as a cylinder. Note that this approximation was only made for the convenience of calculation. Since the depression-zone volume only takes less than 6% (below 2% in most cases, up to 5.7%, as shown in Figure 18) of the melt volume, the geometry assumption of the depression zone does not have a significant impact on the melt pool volume calculation.

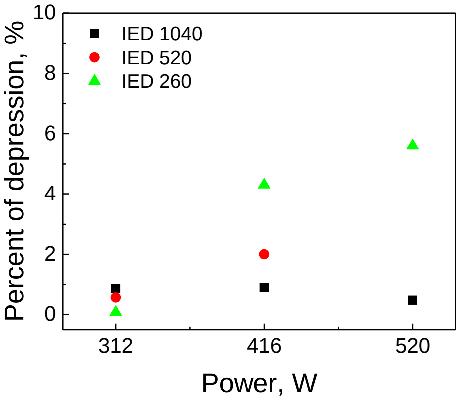

Figure 18. Percentage of depression zone volume over melt pool volume. Original figure from [37].

Most of the dimension values can be directly measured on the projection view of the sample provided by the X-ray images, including the length (L_{up}) and height (H) of the top melt pool, length (L_{down}) and depth (D_m) of the bottom melt pool, width (W_d) and depth (D_d) of the depression zone, as illustrated in Figure 17(c). The width of the top melt pool and the bottom melt pool, W_m, were assumed to be the same, measured from the SEM images (top view) of the laser scanned track, as shown in Figure 17(d). Hence, the melt pool volume (V) can be expressed by:

$$V = V_{top} + V_{bottom} - V_{depression} = \frac{1}{3} W_m L_{up} H + \frac{1}{3} W_m L_{down} D_m - \frac{1}{3} W_d^2 D_d \qquad \text{Eq. 3}$$

when W/D ≥ 1, or

$$V = \frac{1}{3}W_m L_{up} H + \frac{1}{3}W_m L_{down} D_m - \pi(\frac{W_d}{2})^2 D_d \qquad \text{Eq. 4}$$

When W/D < 1.

The calculated melt pool volume, as a function of laser power under constant IEDs, is displayed in Figure 19. The result shows that the melt pool volume has an increasing tendency toward higher laser power at each IED level. The percentage of change in melt pool volume, with respect to the first condition (104 W), was also calculated and plotted, and the equation is noted in Figure 19(b). The melt pool volume exhibits up to three orders-of-magnitude change within the experimental conditions.

Since a constant IED does not deliver the same melt volume, the final additive manufactured parts, built with various combinations of laser power and scan speed under the same IED, will unlikely have the same properties. This is because different melt volumes could affect a series of dynamic processes during laser scanning, such as the solidification rate (that will lead to different microstructures and phases), residual stress distribution, and melt pool-powder bed interaction (that may lead to different spattering patterns, denudation area, material deposition rate, etc.).

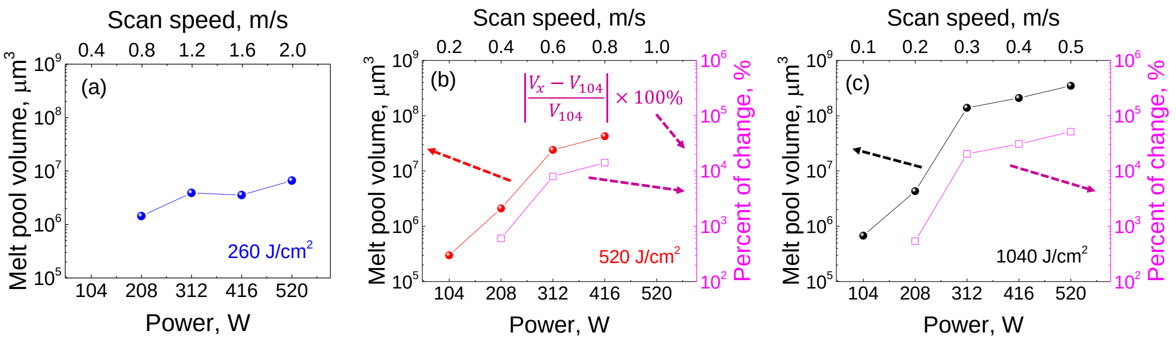

Figure 19. Melt pool volume as a function of processing parameters under constant IED levels. Original figure from [37].

4.5 Mechanisms of Melt Pool Variation under a Constant IED Level

4.5.1 Origin of Melt Pool Variation under a Constant IED Level

Section 4.4 revealed that the melt pool volume undergoes orders-of-magnitude change within the same IED, which indicates that simultaneously increasing laser power and scanning speed can significantly increase the amount of energy for melting the material. The energy variation for melting is a consequence of two competing factors: energy absorption and energy dissipation. Since a constant IED level ensures the same amount of energy being supplied from the heat source, the variation of energy dissipation within a constant IED level seems to account for energy variation. With the consideration of energy dissipation, a normalized enthalpy model that can predict the onset of keyholing has been proposed by King et al. [101] based on the work of Hann et al. [102] and was later validated by [103,104] and further developed by [18,105,106]. Bertoli et al. [107] have proven that the normalized enthalpy model can predict the keyholing threshold and the melt pool depth under a constant IED.

It is straightforward why the same IED can have different energy dissipation rates. By definition, the same IED means the same amount of energy is applied in a certain area. However, the time for energy dissipation differs for different laser-matter interaction times. When the laser scan speed is high, the shorter energy dissipation time will conserve more energy for melting. In other words, even with the same IED, the efficiency for melting the material could be different.

Melting efficiency (η_m) describes the ratio of energy for melting the material (and heating the molten material) over the total energy absorbed by the material, as expressed by:

$$\eta_m = \frac{E_m}{E_{ab}} \qquad \text{Eq. 5}$$

where E_m is the energy required to melt the material, E_{ab} is the total energy absorbed by the material. As will be explained in the next section 4.4.2, the energy absorption is mainly due to the Fresnel laser absorptivity (a_F), Eq. 5 can be re-written into:

$$\eta_m = \frac{E_m}{E_{ab}} = \frac{E_m}{a_F \cdot P \cdot \tau} \qquad \text{Eq. 6}$$

where P is the laser power, τ is the laser exposure time. Since the Fresnel laser absorptivity (a_F) can be calculated from the shape of the depression zone (and will be presented in section 4.4.2), the key to calculating the melting efficiency is to estimate the energy required to melt the material (E_m). To generate a certain size of a melt pool, an energy conservation equation can be established as:

$$E_m = m \cdot \left(\int CdT + L \right) \qquad \text{Eq. 7}$$

where m is the mass of the melt pool, C is the specific heat of the material, L is the latent heat during solid-liquid phase transformation. Taking $m = V \cdot \rho_{liq}$, where V is the volume of the melt pool, ρ_{liq} is the density of the liquid metal; $\int CdT = \int_{T_o}^{T_m} C_s dT + \int_{T_m}^{\frac{T_m+T_b}{2}} C_l dT$, where T_o, T_m, T_b are the room temperature (20°C), melting point, and boiling point of the material, C_s and C_l are the specific heats of solid and liquid material, Eq. 7 can be re-written into:

$$E_m = V \cdot \rho_{liq} \cdot \left(\int_{T_o}^{T_m} C_s \, dT + \int_{T_m}^{\frac{T_m+T_b}{2}} C_l \, dT + L \right) \qquad \text{Eq. 8}$$

For AlSi10Mg alloy, the physical properties were taken from [108]: T_m = 555°C, T_b = 2467°C, L = 476.5 kJ/kg, C_s = 1098 J/(kg·°C), C_l = 1175 J/(kg·°C), and ρ_{liq} = 2210 kg/m^3. The material process-related property, melt pool volume (V), has been calculated and presented in section 4.4. Substituting the above numbers into Eq. 8, the energy required to melt the material (E_m) can be obtained. Substituting E_m into Eq. 6, along with $\tau = L/v$ (where L is the length of melt pool, v is the laser scan speed), the equation of melting efficiency η_m can be solved. To be noted, since the upper limit of the integral $C_l dT$ is $(T_m + T_b)/2$, this term is overestimated for the case of elongated melt pool. Therefore, the calculated E_m is the upper limit of all possible conditions. The results of melting efficiency calculation under three constant IED levels are exhibited in Figure 20.

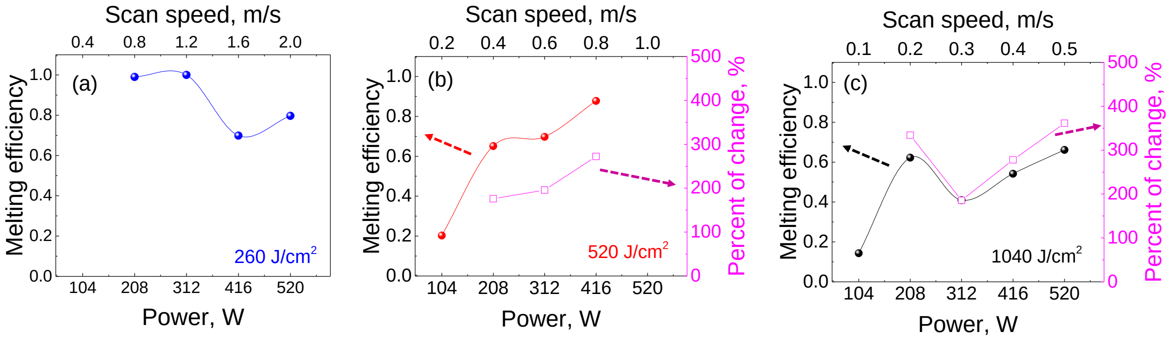

Figure 20. Melting efficiency as a function of processing conditions under constant IED levels. The hollow squares show the percentage of change under each processing condition with respect to the condition of 104 W. The percentage of change was not calculated in (a) due to the lack of a melt pool under 104 W. Original figure from [37].

The maximum efficiency is around four times as compared to the lowest efficiency, under all conditions in the present work. However, this amount of increase is insufficient to account for the orders-of-magnitude change of melt pool volume, which brings our attention back to examining the energy absorption variation within a constant IED level.

4.5.2 Laser Absorptivity Variation under a Constant IED Level

The absorbed energy usually originates from the primary energy transfer through direct laser-material interaction (Fresnel absorption) and the secondary energy transfer through plasma or metal vapor-material interaction [109,110]. Since the thermal effect of plasma is relatively small under additive manufacturing conditions [23,94,111,112], it was assumed here that the energy absorbed by the material entirely comes from Fresnel absorption.

Once a keyhole is generated, the laser beam will undergo multiple reflections in the keyhole. The Fresnel absorptivity can be reasonably calculated by considering the transverse-electric (TE) and transverse-magnetic (TM) polarization and multiple reflections of the laser beam inside the keyhole following [113]:

$$\text{TE: } r_{TE} = \frac{\cos\theta - \sqrt{\left(n_R^2 - n_I^2 - sin^2\theta\right) + i(2n_R n_I)}}{\cos\theta + \sqrt{\left(n_R^2 - n_I^2 - sin^2\theta\right) + i(2n_R n_I)}} \qquad \text{Eq. 9}$$

$$\text{TM: } r_{TM} = \frac{[n_R^2 - n_I^2 + i(2n_R n_I)]\cos\theta - \sqrt{\left(n_R^2 - n_I^2 - sin^2\theta\right) + i(2n_R n_I)}}{[n_R^2 - n_I^2 + i(2n_R n_I)]\cos\theta + \sqrt{\left(n_R^2 - n_I^2 - sin^2\theta\right) + i(2n_R n_I)}} \qquad \text{Eq. 10}$$

where r_{TE} is the reflection coefficient of the TE polarization mode, r_{TM} is the reflection coefficient of the TM polarization mode, θ is the incident angle, n_R and n_I are the real part and imaginary part of the complex refractive index of molten AlSi10Mg, respectively.

According to Eq. 9 and Eq. 10, the reflection coefficient for each polarization can be reduced to a ratio of complex numbers in the form of $(a+bi)/(c+di)$, so that

$$R_{TE} = r_{TE}^2 = ({a_{TE}}^2 + {b_{TE}}^2)/({c_{TE}}^2 + {d_{TE}}^2) \qquad \text{Eq. 11}$$

$$R_{TM} = r_{TM}^2 = ({a_{TM}}^2 + {b_{TM}}^2)/({c_{TM}}^2 + {d_{TM}}^2) \qquad \text{Eq. 12}$$

where R_{TE} and R_{TM} are the reflectance for TE mode and TM mode, respectively. Generally, the reflectance can be expressed as a combination of TE and TM:

$$R = (R_{TE} + R_{TM})/2 \qquad \text{Eq. 13}$$

Since the shape of the depression zone has been captured by the X-ray images, the reflection times and the incident angle for each reflection can be determined by tracing a ray of light to see how it propagates in the keyhole. To simplify the calculation, the following assumptions were made and schematically shown in Figure 21: (1) The first incidence acts at the center of the front depression wall. (2) The depression walls are flat. (3) The laser beam is treated as a “line” without thickness.

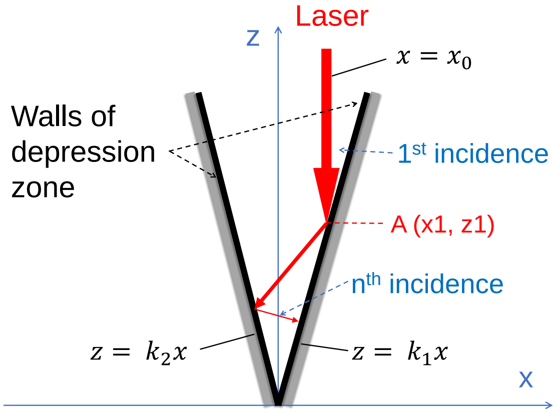

Figure 21. Schematic of a simplified ray-tracing model. Original figure from [37]

The front and rear depression walls can be expressed by:

Front wall: $z = f_f(x) = k_1 x + l_2$ Eq. 14

Rear wall: $z = f_r(x) = k_2 x + l_2$ Eq. 15

The equation of the initial ray of the laser beam can be expressed as:

$$x = x_0 \qquad \text{Eq. 16}$$

The first incident point A (x_1, z_1) can be calculated by solving the simultaneous equations Eq. 14 and Eq. 16. The slope of the normal line of the front depression wall at the first incident point is:

$$k_{n1} = -\frac{1}{k_1} \qquad \text{Eq. 17}$$

The equation for the normal line of the keyhole front wall at the first reflection can thus be obtained by the incident point A and normal line slope k_{n1}:

$$z = k_{n1} x + l_{n1} \qquad \text{Eq. 18}$$

With the aid of the normal line, one point located at the reflection ray, C (x_{r1}, z_{r1}), which is the symmetric point of B (x_0, 0) about the normal line, can be acquired. By the coordinates of A and C, the expression of the reflected beam, which is also the incident beam for the subsequent reflection, can be obtained. Similarly, the calculation could continue until the beam escapes from the depression zone. The incident angle θ at each incidence can be obtained. The laser absorptivity at nth incidence can thus be calculated as:

$$\alpha_n = [\prod_{j=1}^{n-1} R(j)][1 - R(n)] \qquad \text{Eq. 19}$$

where $R(n)$ is the reflectance at the nth incidence. The total laser absorptivity is the sum of all the absorptivities for each incidence.

The calculated absorptivity, as a function of laser power under constant IEDs, is shown in Figure 22. The error bars show the standard deviation of the dynamic depression zone measurements at different moments in the X-ray imaging video. Note that the data points highlighted by red dashed circles at 104 W and 208 W laser power were not calculated by the ray-tracing model due to the absence of a depression zone under those processing conditions. For comparison purposes, the absorptivity of liquid metal with a flat surface is plotted at these conditions because most of the laser beam interacts with the melt during laser scanning [94]. In general, absorptivity increases with increasing laser power for each of the three IED levels. A big jump in absorptivity occurs during the conduction-keyhole transition (208 W – 312 W) for IEDs of 520 J/cm^2 and 1040 J/cm^2 as a consequence of keyhole formation. The absorptivity in the keyhole regime becomes relatively consistent as a function of laser power for each IED level but still undergoes slow growth.

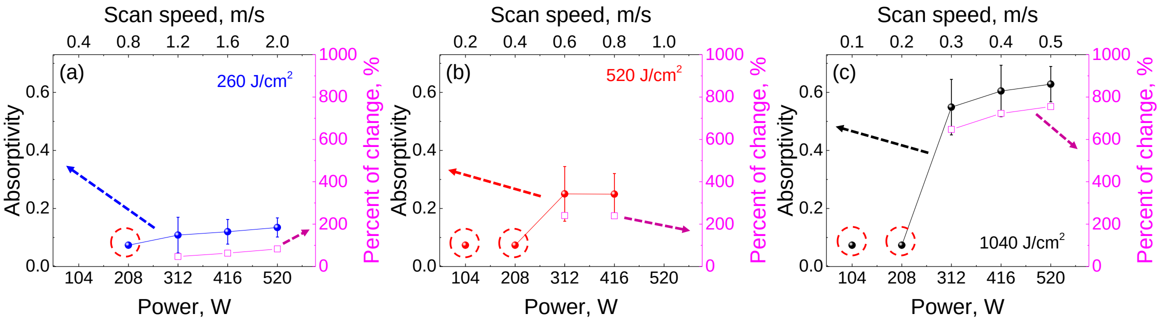

Figure 22. Laser absorptivity as a function of processing parameters under constant IED levels. Original figure from [37].

The above results show that, despite the output of the same amount of energy from the heat source, the amount of energy absorbed by the material can be very different under a constant IED level. Laser absorptivity increases with increasing laser power under constant IEDs.

4.5.3 Separate Roles of Laser Parameters in Depression Zone Development

Although it was demonstrated that different processing conditions under the same IED level have different energy absorption, the cause for this phenomenon is unclear. To be specific, since a higher laser power dumps more energy into the material, while a higher laser scan speed reduces the energy density output to the material, why simultaneously increasing laser power and laser scan speed (under a constant IED) cannot maintain a constant energy absorption, but increase it instead?

In practice, since the Fresnel laser absorptivity of the material is mainly determined by the shape and dimension of the depression zone, the fact that different combinations of processing parameters (with the same IED) lead to different absorptivity implies that laser power and laser scan speed may have separate impacts on the depression zone development. Therefore, the respective effects of laser power and laser scan speed on depression zone development were examined and described below.

- *Effect of laser power on depression zone development*

To investigate the effect of laser power on depression zone development, the variation in dimensions of the depression zone as a function of laser power is depicted in Figure 23. The experiments were carried out with a constant laser scan speed of 0.6 m/s, and the laser power varied in a range of 208 W – 416 W, with an increment of 52 W. The width and depth of the depression zone are displayed in Figure 23(a) and (b), while the width/depth ratio is shown in Figure 23(c). As seen in Figure 14, the depression zone is not exactly on the same axis as the incident laser beam but has a little backward tilt angle with reference to the axial direction of the beam. The tilt angle of the front depression-zone wall [schematically illustrated by α in Figure 17(c)], as a function of laser power, is also measured and plotted in Figure 23(d).

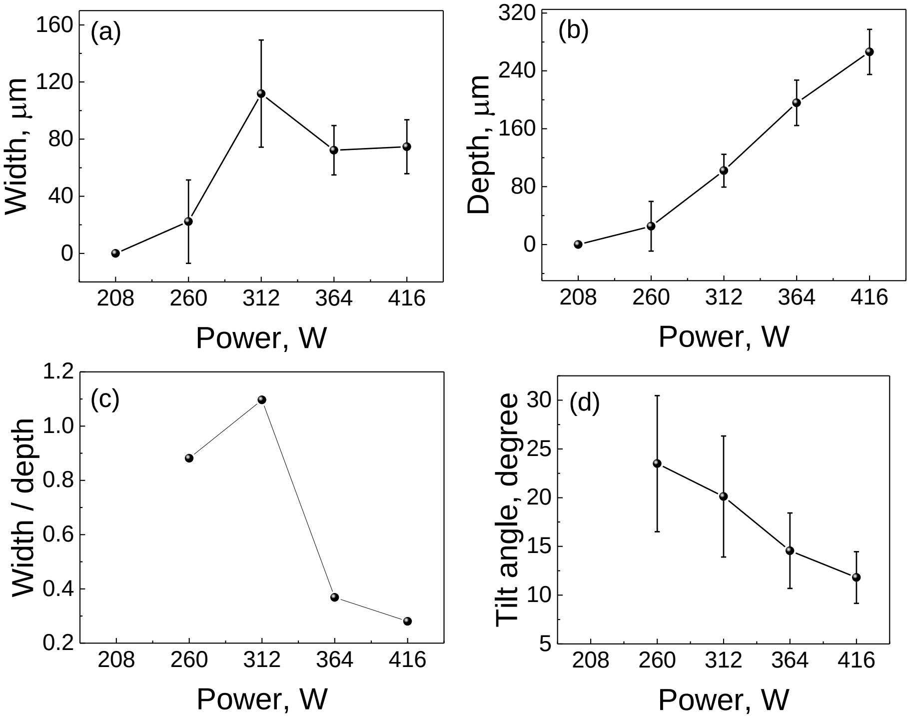

Figure 23. The depression zone dimensions as functions of laser power with a constant laser scan speed of 0.6 m/s. Original figure from [37].

In general, the depression zone dimension tends to increase with increasing laser power, especially for the depth of the depression zone Figure 23(b). Within 208–312 W, the width of the depression zone also increases with the increase of laser power. Note that the melting regime under 208 W is the conduction regime, where the depression zone is absent. At the stage of 364–416 W, the laser power is high enough to promote the drilling effect so that the depression zone grows deeper at higher laser power while the width of the depression zone remains constant. The tilt angle of the front depression wall decreases from 24° to 13° when laser power increases from 260 W to 416 W, as shown in Figure 23(d). The tilt angle has an impact on the laser absorptivity in terms of affecting the reflection times of the laser beam between the depression walls.

Despite some fluctuations in the width of the depression zone, with increasing laser power, the depression zone grows deeper into the material. Increasing the laser power has a positive effect on the depth of the depression zone.

- *Effect of laser scan speed on depression zone development*

To investigate the effect of laser scan speed on the development of the depression zone, experiments were carried out with laser scan speeds varied in a range of 0.4–1.6 m/s, with an increment of 0.4 m/s. The laser power was kept constant at 416 W. The depression zone variations as functions of laser scan speed are shown in Figure 24(a–d).

Compared with the effect of laser power, laser scan speed has a different influence on changing the dimensions of the depression zone. Based on the width/depth ratios shown in Figure 24(c), the melting regimes of 0.4 m/s and 0.8 m/s are keyhole regime, while the rest are transition regime. The shape of the width/depth ratio curve in Figure 24(c) is the inverse of that in Figure 23(c). When the laser scan speed shifts from the keyhole regime into the transition regime (0.8–1.2 m/s), the depression zone width starts to increase, which may be due to the moving speed of the rear depression wall cannot effectively catch up with the laser scan speed (i.e., the moving speed of the front depression wall). However, the width increase ceases when the laser scan speed increases to a certain level (1.2 m/s), at which the input energy density is insufficient to sustain the expansion of the depression zone. This explains the drop in the depression zone width and width/depth ratio between 1.2 m/s and 1.6 m/s.

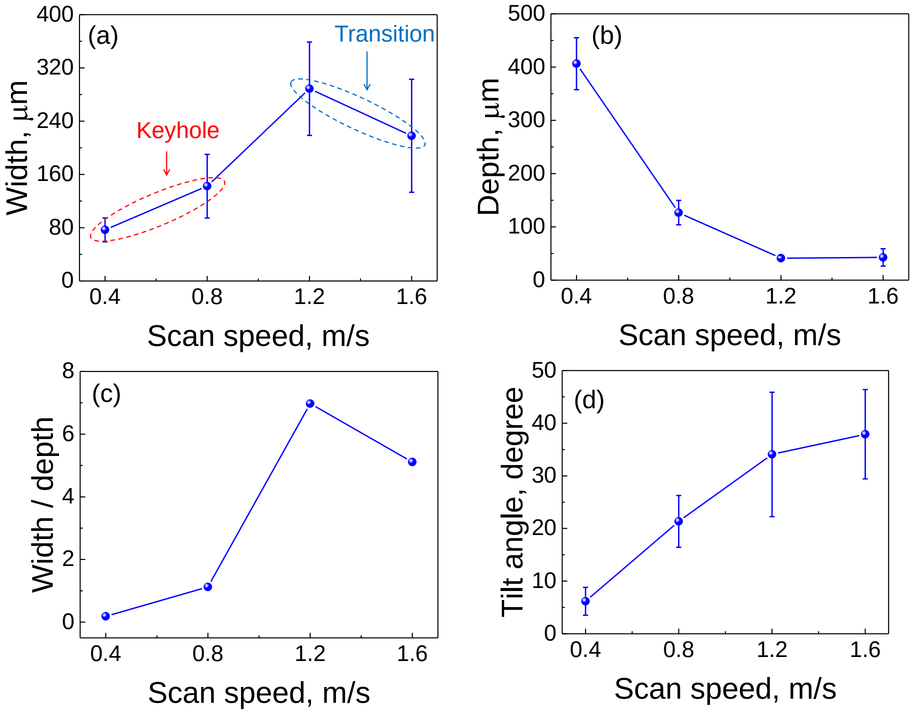

Figure 24. The depression zone dimensions as functions of laser scan speed with a constant laser power of 416 W. Original figure from [37].

The wider depression zone, higher width/depth ratio [about one order of magnitude higher than those of Figure 23(c)], and large tilt angle induced by high laser scan speed indicate that the laser scan speed has a major influence on the width of the depression zone.

The results in this section suggest that laser power and scan speed have different roles in determining the size and shape of the depression zone. Under the experimental conditions, depression zone depth development relies more on laser power, while the width of the depression zone is more sensitive to laser scan speed. Therefore, laser power and scan speed should be tuned separately during the LPBF additive manufacturing process to optimize the processing condition.

4.5.4 Importance of Considering Absorptivity Variation

A model established in [114] is discussed below to demonstrate the importance of considering absorptivity variation. The model is to predict the depression zone depth with the consideration of different processing parameters under low scan speeds (< 0.33 m/s) and uniform laser intensity profile, in the form of:

$$e = \frac{4kA}{\pi}\frac{P}{d \cdot v} \qquad \text{Eq. 20}$$

where e is the depression zone depth, k is a factor that mainly depends on the material's thermal properties, A is the laser absorptivity, P is the laser power, d is the laser spot size, v is the laser scan speed. To be noticed, $P/(d \cdot v)$ is the IED. k is constant when the material is chosen. In the reference paper [114], the laser absorption was assumed to be constant. Therefore, Eq. 20 can be rewritten into e = constant · IED, which means e should be constant for a fixed IED level. However, from our measurements in Figure 23(b) and Figure 24(b), that depression zone depth e varies in a wide range under a constant IED. Therefore, with the assumptions of constant laser absorptivity, low scan speed, and uniform laser intensity profile, the prediction from Eq. 20 is not consistent with our experimental results.

Once considering the variation of laser absorptivity in Eq. 20, which can be rewritten as e = constant · A · IED, the change of e will greatly rely on the variation of laser absorptivity (A) under a constant IED. This trend is verified in Figure 25, where the variation of depression zone depth and calculated laser absorptivity as a function of laser power [Figure 25(a)] and laser scan speed [Figure 25(b)] were plotted together, respectively. Since the absorptivity variation has a similar trend as the depression zone depth variation, it can be expected that the predicted depression zone depth e will also have a similar trend as the experimental measurements. Hence, the Eq. 20 have the potential to be extended to the processing conditions of high scan speeds ($\geqslant$ 0.4 m/s) and Gaussian laser intensity profile, with the consideration of variation in laser absorptivity.

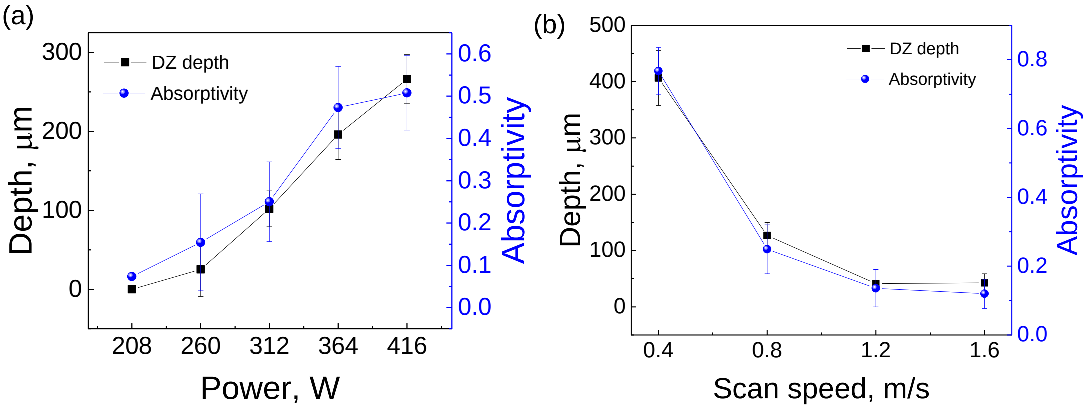

Figure 25. The comparison of the trend between depression zone depth and laser absorptivity variations. (a) Comparison under a constant laser scan speed of 0.6 m/s. (b) Comparison under a constant laser power of 416 W. Original figure from [37].

4.6 Summary and Conclusions

This chapter presents the direct observation and quantification of melt pool variation during the LPBF additive manufacturing process through in-situ high-speed high-energy X-ray imaging and uncovers the mechanism of melt pool variation under a constant IED level. The major conclusions are as follows:

(1) Under a constant IED level, different melting regimes, melt pool dimensions, and melt pool volumes were observed under different combinations of laser power and

laser scan speed under LPBF conditions. When simultaneously increasing laser power and laser scan speed within a constant IED level, the melting regime can shift from a no-melt pool regime to the conduction regime, transition regime, and keyhole regime. All three dimensions of the melt pool increase, and the melt pool volume exhibits up to three orders of magnitude increase.

(2) The energy dissipation variation is demonstrated to be insufficient to account for the significant melt pool change under a constant IED. The energy absorption variation under a constant IED level is found to be an important factor that induces the variations in the melt pool. Energy absorption exhibits a trend to increase when laser power and laser scan speed are simultaneously increased under a constant IED level.

(3) The variation in energy absorption (within a constant IED level) exists because laser power and laser scan speed play different roles in the development of the depression zone. Under the experimental conditions of this work, laser power is found to have a greater impact on the depth of the depression zone, while laser scan speed affects the width of the depression zone more. Therefore, instead of using IED to evaluate the combined effect of laser power and laser scan speed, these two factors should be tuned separately to achieve an optimized processing condition in the LPBF process.

Chapter 5: Full-field Mapping of Melt Flow Dynamics

This chapter contains experimental data and results that have been published in the following works:

Q. Guo, C. Zhao, M. Qu, L. Xiong, S.M.H. Hojjatzadeh, L.I. Escano, N.D. Parab, K. Fezzaa, T. Sun, L. Chen, In-situ full-field mapping of melt flow dynamics in laser metal additive manufacturing, Addit. Manuf. 31 (2020) 100939. [59]

Q. Guo, M. Qu, L.I. Escano, S.M.H. Hojjatzadeh, Z. Young, K. Fezzaa, L. Chen, Revealing melt flow instabilities in laser powder bed fusion additive manufacturing of aluminum alloy via in-situ high-speed X-ray imaging, Int. J. Mach. Tools Manuf. 175 (2022) 103861. [115]

The publication rights for this section are given in Appendix A. Appropriate recognition is given to the relevant citation for the material in which it was originally published. The presented material represents my contributions and material collected with or by a collaborator has been highlighted as such.

Melt flow determines the heat transfer and mass transfer within the melt pool, thus it is critical to characterize its behavior during the LPBF process. In this chapter, an approach was developed to experimentally study the melt flow behavior in the whole melt pool in laser additive manufacturing by tracing uniformly dispersed populous micro-tracers with in-situ high-speed high-resolution X-ray imaging. The melt flow dynamics in every location of the entire melt pool under conduction-mode and keyhole-mode laser melting were revealed and discussed.

5.1 Experiment Design and Melt Flow tracing Approach

5.1.1 Experiment Design

Since X-ray imaging only provides a projectional two-dimension view, two setups were made to obtain two orthogonal views for three-dimensional reconstruction. As shown in Figure 26, a longitudinal projection of the melt pool was obtained when the laser beam scans perpendicular to the X-ray beam. In contrast, a transverse projection of the melt pool was obtained when the laser scans parallel to the X-ray. The three-dimensional coordinate system used in this study, as indicated in Figure 26, was defined as follows: z is the normal direction of the powder bed, y is the laser scan direction, and x is the normal direction of the y-z plane, following the right-hand rule.

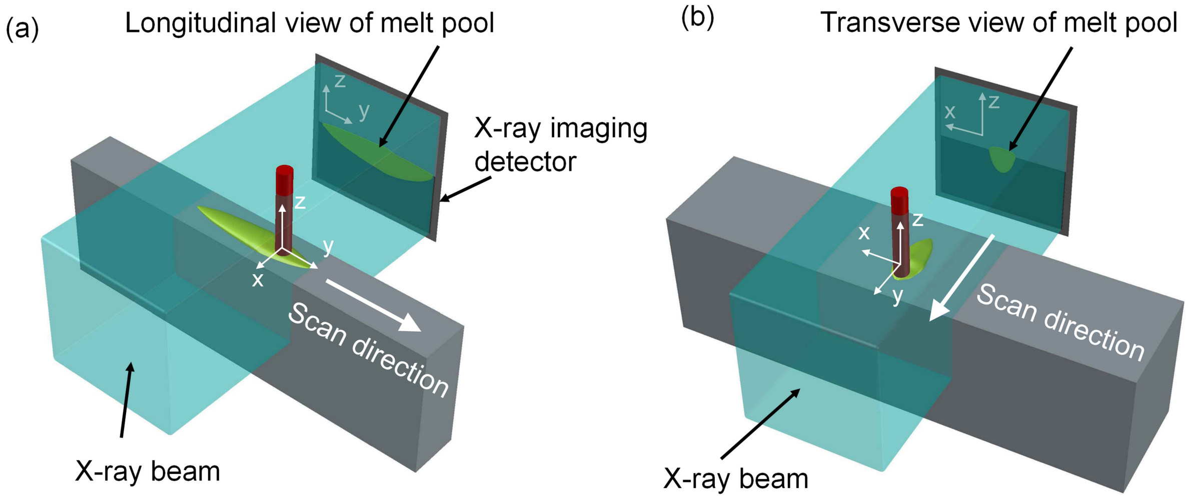

Figure 26. Schematic illustration of two projection views used in this work. The powder bed is not shown in the schematic. Original figure from [59].

Two aluminum alloys, AlSi10Mg and Al-6061, were used in this study. Aluminum alloys were selected because of their high X-ray transparency. This study mainly focuses on AlSi10Mg, a widely used material for additive manufacturing. Al-6061, a common aluminum alloy on the market, was chosen to check whether the melt flow pattern observed in AlSi10Mg can also be observed in another alloy with different composition. The powder bed is composed of either AlSi10Mg or Al-6061 aluminum alloy, with the substrate material identical to the powders. To ensure better X-ray transparency, the powder bed width (along X-ray incidence) was fixed at 0.5 mm when the laser scans perpendicularly to the X-ray beam (with a scan length of 2.5 mm), while 1.0 mm-thick substrates were used when the laser scan direction was parallel to the X-ray beam (with a scan length of 0.8 mm). Argon gas was used for process protection. Table 2 lists the materials and detailed processing parameters in this work. Each set of parameters was repeated three times. The parameter selection for generating conduction-mode and keyhole-mode melting was based on Chapter 4 [37].

Table 2. Materials and processing parameters.

Material	Processing parameter	Melting mode
AlSi10Mg	260 W, 0.6 m/s	Conduction mode
AlSi10Mg	364 W, 0.6 m/s	Keyhole mode
Al-6061	520 W, 0.4 m/s	Keyhole mode

5.1.2 Melt Flow Tracing Approach

Flow tracers were used to trace the melt flow during laser melting. The speed (v) of a tungsten tracer was calculated by dividing its displacement (d) by its traveling time (t), $v = d/t$. The tracer's displacement was calculated via its two-dimensional (2D) coordinates change ($\Delta x = |x_2 - x_1|$, $\Delta y = |y_2 - y_1|$) from one frame to the next frame in the 2D X-ray image planes, where $d = (\Delta x_2 + \Delta y_2)^{1/2}$. The tungsten tracer's traveling time is the time interval between two frames, determined by the recording frame rate of the X-ray imaging video (50 kHz or 140 kHz in the present work).

For the tracers to effectively reflect the movement of the surrounding liquid flow, several requirements must be fulfilled: (1) The tracer must remain solid in the molten metal, meaning that the tracer's melting temperature should be much higher than that of the matrix material (aluminum, in this case). (2) For the tracer to be detectable in X-ray images, the tracer must exhibit sharp contrast to the matrix material, meaning the tracer's density should be much higher or lower than the matrix material. (3) The gravity/buoyancy of the tracer should have a negligible effect on its movement. (4) The tracer must be accelerated fast enough by the surrounding liquid to avoid a noticeable delay to the flow. (5) The tracer should not significantly change the viscosity of the molten liquid in the melt pool. Taking all of the above into account, 1 vol.% tungsten micro-particles (with an average diameter of 5 µm) in metal powders were identified as effective tracers in this system. The effectiveness of tungsten micro-particles as flow tracers will be demonstrated in Section 5.5.

The tungsten micro-particles were uniformly mixed with the feedstock aluminum powders by ball milling, as shown in Figure 27(a). The size distribution of the aluminum powder after ball milling is shown in Figure 27(b). Both size and amount of the tracer particles were optimized to be able to trace the melt flow in every location of the whole melt pool yet impose a minimum effect on the viscosity of the molten aluminum. Also, the small tracers used here allowed us to embed a large number of tracers under a fixed volume fraction so that the fluid flow in every location of the melt pool could be traced accurately.

Uniformly dispersed micro-sized pores in AlSi10Mg were used as a complementary tracer, as marked in Figure 26(b). The pores in the AlSi10Mg sample were introduced in the LPBF building process. The mass density of the pore is much lower than that of aluminum melt, which was used to cross-check the effect of the tracer density on melt flow tracing results. The pore movement in the main body of the melt pool was consistent with the tungsten particle movement, except for the region around the keyhole. (The reason for this discrepancy will be explained in Section 5.5.)

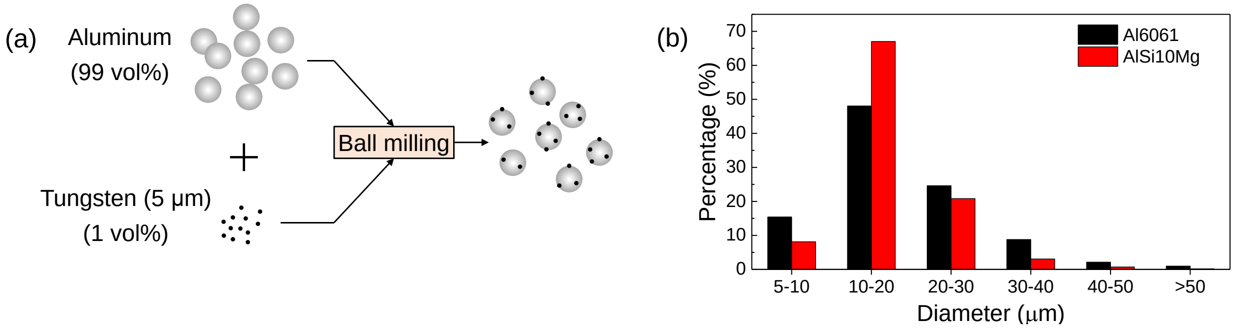

Figure 27. Powder preparation method for melt flow tracing. (a) The feedstock aluminum powder was mixed with 1 vol.% tungsten particles (~5 μm) by ball milling. (b) Aluminum particle size distributions of the feedstock Al-6061 and AlSi10Mg powder after ball milling with tungsten particles. The distribution calculation did not include aluminum particles smaller than 5 μm or any tungsten particles. Original figure from [115].

5.1.3 Image Processing

To clearly identify the melt pool boundary and tracer movement, the raw X-ray images were processed by ImageJ to reduce noise and enhance contrast, as illustrated in Figure 28. The image intensity at each pixel of Frame(i) was divided by the intensity of the corresponding pixel in Frame(i+3) so that the motionless part in the image was converted to a blank background. Figure 28(b) shows the representative post-processed image, where the tracer movement is much clearer, and the melt pool boundary is obvious. Note that the positions of a particular tracer in Frame(i) and Frame(i+3) will both appear in a processed image, but the resulting contrasts are different for each type of tracer. For the tungsten particles, the resulting contrast from Frame(i) appears to be dark in the processed image, while the resulting contrast from Frame(i+3) is bright, as illustrated in Figure 28(c). As for the pore, the contrast from Frame(i) is bright, but the contrast from Frame(i+3) is dark, as shown in Figure 28(d).

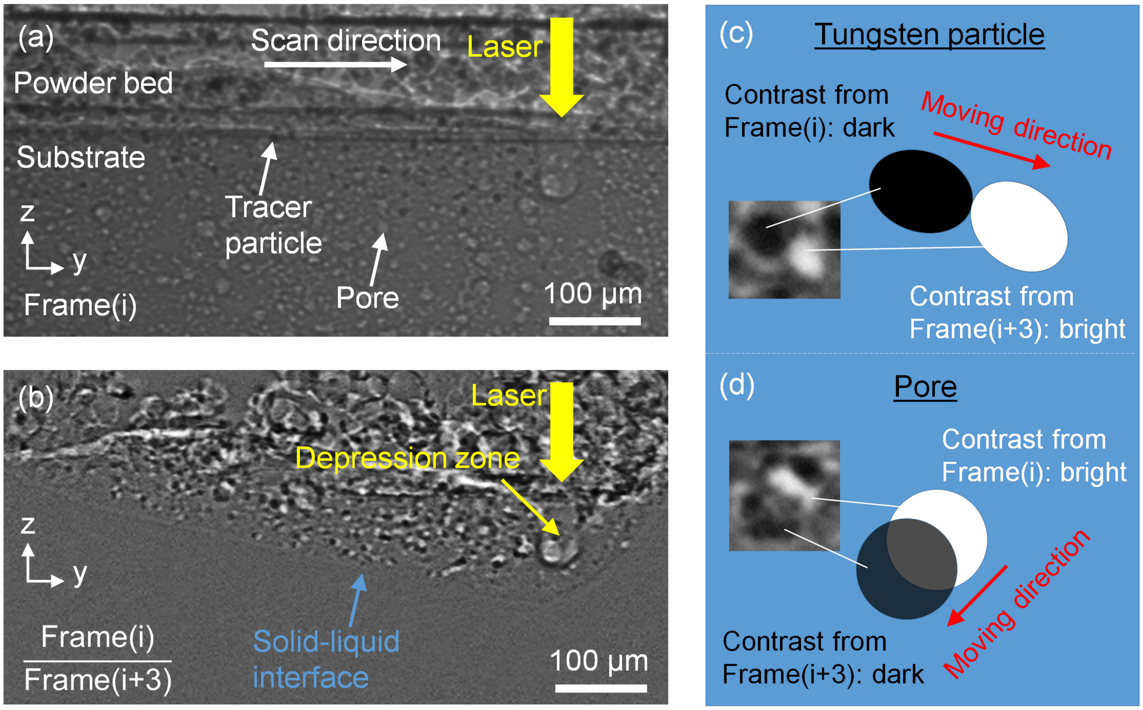

Figure 28. Image processing method for better detection of flow tracers. (a) Representative X-ray image before image processing. (b) X-ray image after image processing. (c, d) Schematics showing different contrasts of two types of flow tracers after image processing. Original figure from [59].

5.2 Melt Flow Pattern under Conduction-Mode Melting

The general shape of the melt pool under conduction mode in both the longitudinal view (projected in the y-z plane) and transverse view (projected in the x-z plane) are displayed in Figure 29(a) and (c), respectively. The test was on an AlSi10Mg powder bed with a laser power of 260 W and a scan speed of 0.6 m/s. The representative tracers were circled in the image, with their projectional moving directions in the y-z plane indicated by arrows. The moving trend of the tracers was summarized in the corresponding schematics shown in Figure 29(b, d).

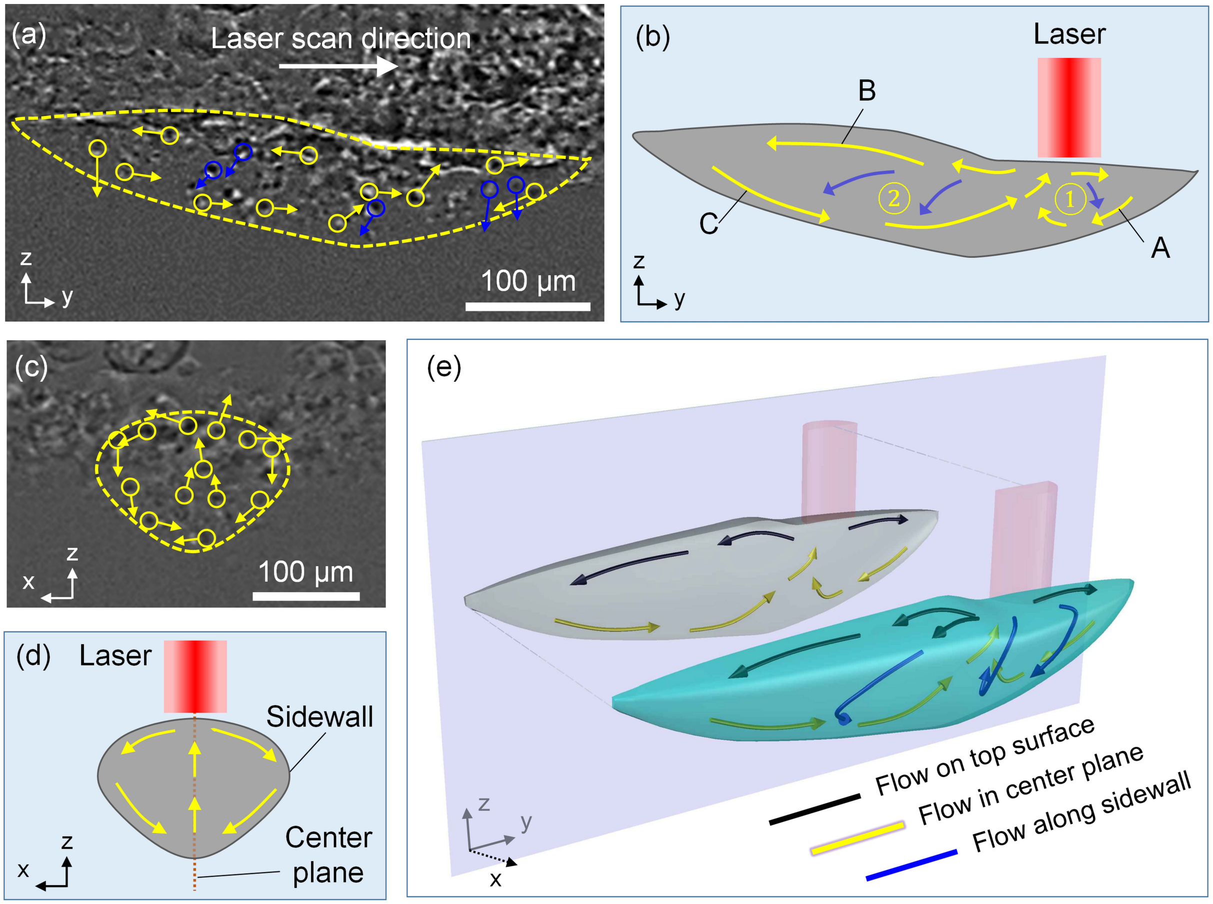

Figure 29. Melt flow pattern under conduction mode. (a, b) Melt flow pattern in longitudinal view. (c, d) Melt flow pattern in transverse view. (e) Reconstruction of three-dimensional melt flow pattern. Original figure from [59].

In the transverse view, as displayed in Figure 29(c), the tracers in the center plane of the melt pool move upward, while those close to the melt pool sidewalls move downward. Two vortices are thus formed with opposite circulating directions, as illustrated in Figure 29(d). In longitudinal view [Figure 29(a)], arrows in yellow and blue were used to distinguish the movement of tracers in the center plane and along the sidewalls. As depicted in Figure 29(b), the flow forms a clockwise vortex ① ahead of the laser beam and a counterclockwise vortex ② behind the laser beam. The projectional flow speed (the projection of the flow velocity in the y-z plane) of three representative streams, A, B, and C were quantified in [59]. The flow along the sidewalls in the longitudinal view, as indicated by blue arrows in Figure 29(b), travels from the top surface to the bottom of the melt pool, which is consistent with the observation in the transverse view [Figure 29(c)].

A three-dimensional reconstruction for conduction-mode melt flow is exhibited in Figure 29(e), based on the observations above. For the clarity of illustration, the melt pool is displayed in halves, with one half (colored by cyan, transparent) showing the three-dimensional flow inside the melt pool, and the other half (colored by gray, opaque) showing the two-dimensional flow pattern only in the middle cross-section (y-z plane). The arrows in black display the flow on the top surface of the melt pool, while the yellow arrows show the flow in the center plane, and the blue arrows represent the flow along the melt pool sidewalls.

5.3 Melt Flow Pattern under Keyhole-Mode Melting

With the formation of a keyhole, the laser beam directly interacts with the interior of the melt pool, which promotes the energy absorption that leads to a much larger melt pool with a more complex flow pattern than that under conduction mode. To facilitate the description, the keyhole-mode melt pool is divided into three regions [i.e., tail, body, and head, as shown in Figure 30(a–c), respectively] along the laser scan direction. The arrows in yellow and blue, similar to conduction mode, were used to distinguish the tracer motions in the center plane and along the sidewalls. In the transverse view of the melt pool, to differentiate the flow patterns around the keyhole from those in the body of the melt pool (behind the keyhole), the flow behavior was recorded during laser scanning [Figure 30(e)] and 50 μs after the laser was off [before the contraction of the melt pool boundary, as displayed in Figure 30(g)], respectively. Note that t_o is the moment when the laser was turned off.

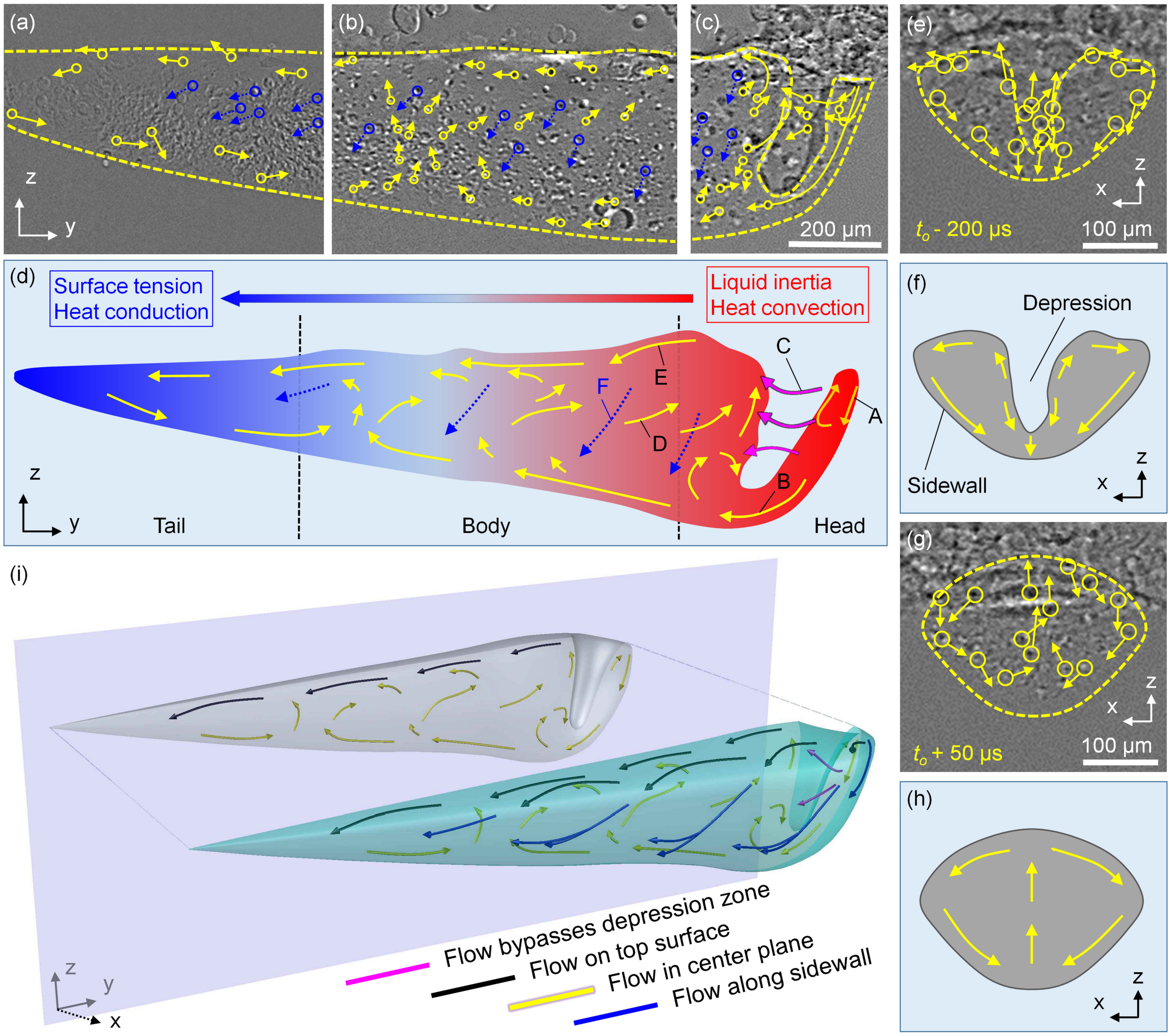

Figure 30. Melt flow pattern under keyhole mode. (a–d) Melt flow pattern in longitudinal view. (e, f) Melt flow pattern in transverse view at the keyhole cross-section. (g, h) Melt flow pattern in transverse view at the cross-section behind keyhole. (i) Reconstruction of three-dimensional melt flow pattern under keyhole mode. Original figure from [59].

The trend of tracer motions in Figure 30(a–c) was summarized and combined in the schematic Figure 30(d), while the tracer movement in Figure 30(e, g) was depicted in schematic Figure 30(f, h). Six types of flow that were marked by A-F in Figure 30(d) will be quantified in Section 5.4. In the center plane, as shown in Figure 30(d), the flow around the keyhole moves upward near the keyhole outlet while moving downward near the bottom of the keyhole, which is consistent with the flow pattern around the keyhole in the transverse view [Figure 30(f)]. The flow bypassing the keyhole travels opposite to the laser scan direction, as illustrated by flow C in Figure 30(d). The flow near the melt pool surface moves backward, from the keyhole outlet to the tail of the melt pool. The flow at the bottom of the melt pool (flow I) also has a main trend of moving backward, except a short forward flow (flow II) was observed at the rear bottom of the melt pool. Flow I and II collide to form a merged flow (flow III) which moves upwards and splits into flows of opposite directions. In the area between the top and bottom backward flow, as pointed out by flow D in Figure 30(d), the general flow movement in the center plane has a tendency to go forward and upward, which is consistent with the observation of flow pattern in transverse view [Figure 30(h)]. The flow along the sidewalls of the melt pool moves downward, as displayed by the blue arrows in Figure 30(d), which is in accordance with the transverse-view observations in Figure 30(f, h). Three-dimensional reconstruction of keyhole-mode melt flow is shown in Figure 30(i). The arrows in magenta show the flow bypassing the keyhole, while the black arrows display the flow on the top surface of melt pool, the yellow arrows indicate the flow in the center plane, and the blue arrows represent the flow along the melt pool sidewalls.

To confirm that the above melt flow pattern is not limited to an alloy with a specific composition, tests on Al-6061 were carried out. A similar size melt pool (and keyhole) was created on Al-6061 with 520 W laser power and 0.4 m/s laser scan speed. The melt flow pattern in Al-6061, as displayed in Figure 31, was consistent with the one in AlSi10Mg.

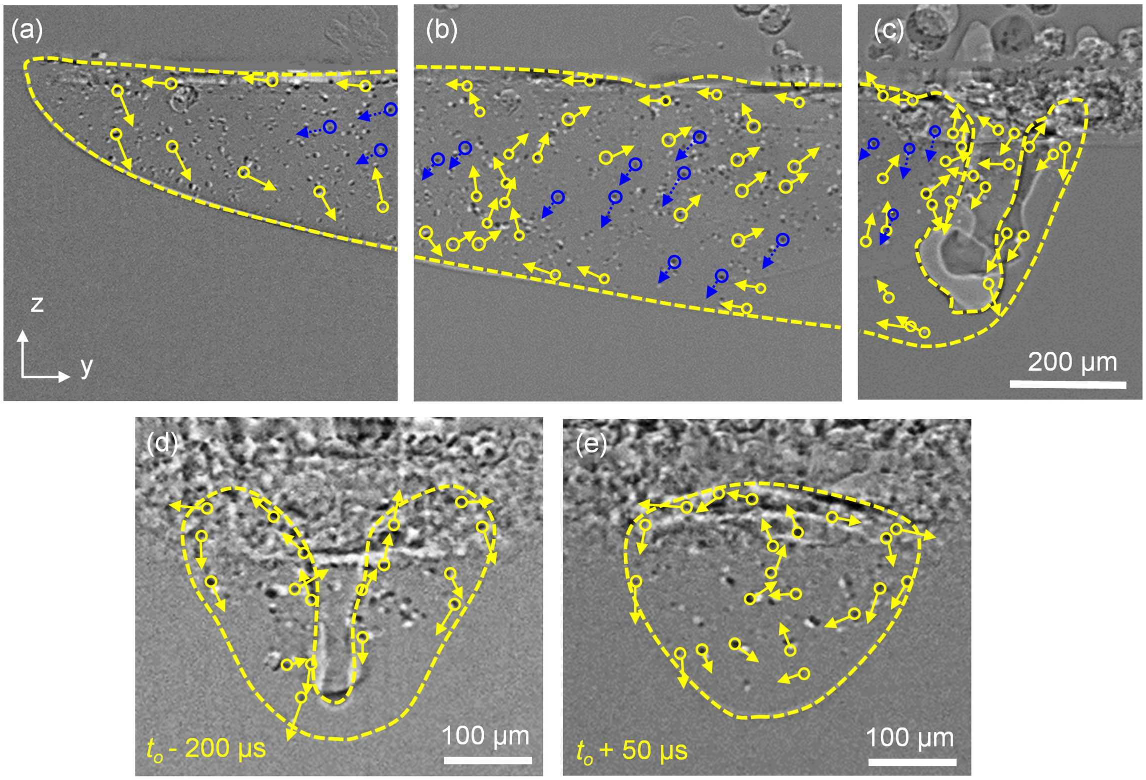

Figure 31. Keyhole-mode melt flow pattern in Al-6061. Original figure from [59]*.*

5.4 Quantification of Flow Speed

The projectional speeds of melt flow A, B, C [as marked in Figure 29(b)] in conduction-mode melt pool and flow A, B, C, D, E, F [as marked in Figure 30(d)] in keyhole-mode melt pool were measured and displayed in Figure 32. The flow direction and location are detailed in Table 3. Note that the flow E, D, and F in keyhole mode were only quantified within a 300 μm region after the keyhole (as will be shown later in Figure 33, that the flow speed attenuates fast at the tail of the melt pool). Since the tracers at different locations (e.g., in the center vs. near the edge) of a particular flow stream may have different speeds, the average speeds of each flow type and the standard deviations are calculated and displayed by blue bars. In addition, the maximum speeds of each type of flow are shown in histograms by red bars as a helpful reference, given that the three-dimensional motion of the tracers may have components perpendicular to the view plane. Under both conduction mode and keyhole mode, flow A (downward flow along the front melt pool boundary) has the highest speed, with maximum speed values of 2.83 m/s for conduction mode and 3.68 m/s for keyhole mode.

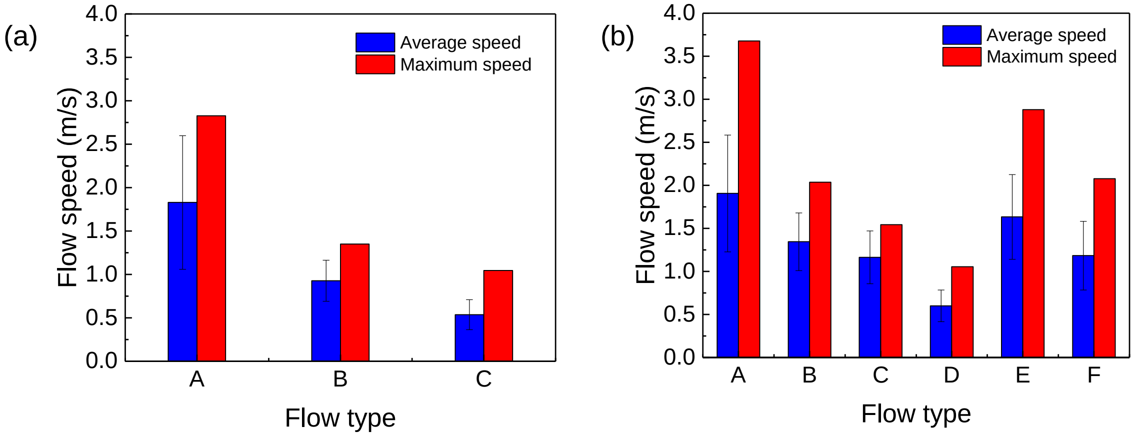

Figure 32. Quantification of flow speed as a function of flow type. (a) Flow speed in the conduction-mode melt pool. (b) Flow speed in the keyhole-mode melt pool. Original figure from [59].

Table 3. Types of flow and their locations.

Melting mode	Flow type	Flow direction	Flow location
Conduction	A	Backward	Along the front melt pool bottom
	B	Backward	Along the melt pool surface
	C	Forward	Along the rear melt pool bottom
Keyhole	A	Downward	Along the front keyhole wall
	B	Downward & backward	Along the keyhole bottom
	C	Backward	Around the keyhole zone
	D	Upward & forward	Toward the keyhole outlet
	E	Backward	Along the surface of melt pool
	F	Downward & backward	Along the sidewall of melt pool

Further quantification was carried out to analyze the general trend of the flow speed as a function of location across the melt pool, given that the above measurements only focused on the flow speed in localized regions. Quantifications were first carried out on AlSi10Mg [Figure 33(a, b)] and then on Al-6061 [Figure 33(c, d)].

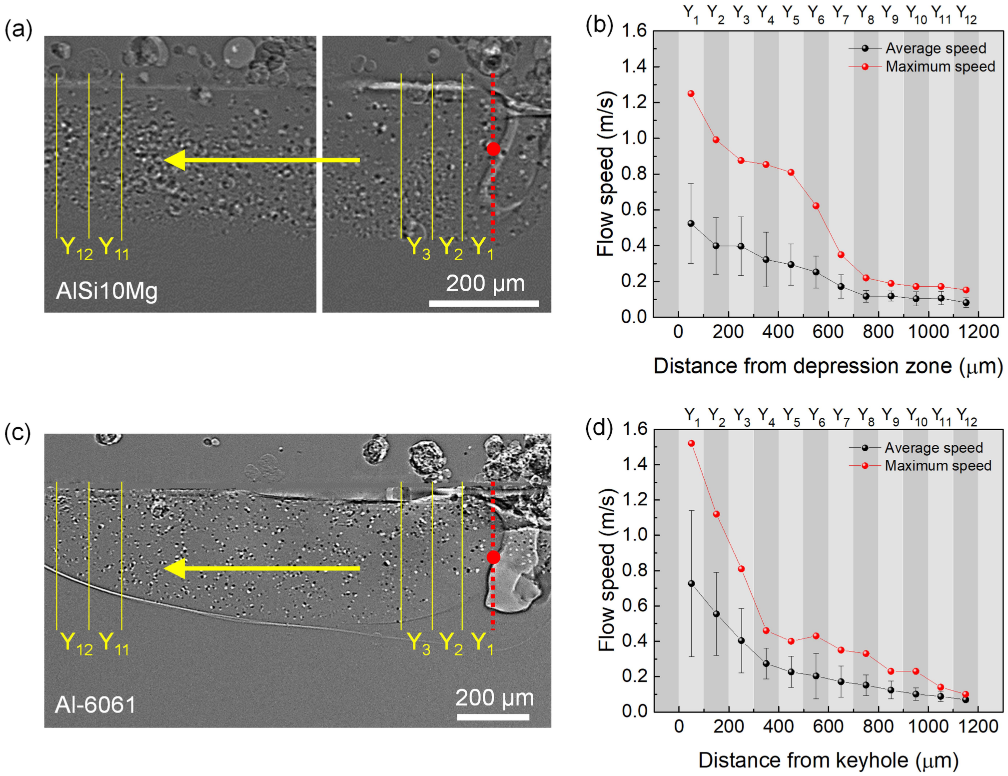

Figure 33. Quantification of flow speed along melt pool. (a, b) Quantification of flow speed in AlSi10Mg alloy. (c, d) Quantification of flow speed in Al-6061 alloy. Original figure from [59].

From the middle of the rear keyhole wall [as marked by the red dot in Figure 33(a)], the melt pool behind the reference position was divided into 12 sections with 100 μm segment width. The projectional speed of the tracers in each section (Yi) was measured and plotted in Figure 33(b). The average and maximum speeds both exhibit a general decreasing trend as a function of the distance from the keyhole. In the first section, Y1, the average speed is 0.52 m/s, and the maximum speed is 1.25 m/s. In the last section, Y12, the average speed is 0.08 m/s, and the maximum speed is 0.15 m/s, which are both an order of magnitude lower than those in section Y1. The quantification stopped at Y12 because the flow speed was so low that it approached the measurement precision (0.025 m/s). The same quantification strategy was applied to the Al-6061 melt pool, as shown in Figure 33(c). A similar decreasing trend in the speeds was observed, as shown in Figure 33(d).

Due to the highly dynamic nature of the keyhole, the general flow speed ahead of the rear keyhole wall was not quantified in the above analysis. Instead, a particular tracer that moved all the way down in the thin liquid film ahead of the keyhole was tracked to reveal the flow behavior at the keyhole area, as shown in Figure 34(a).

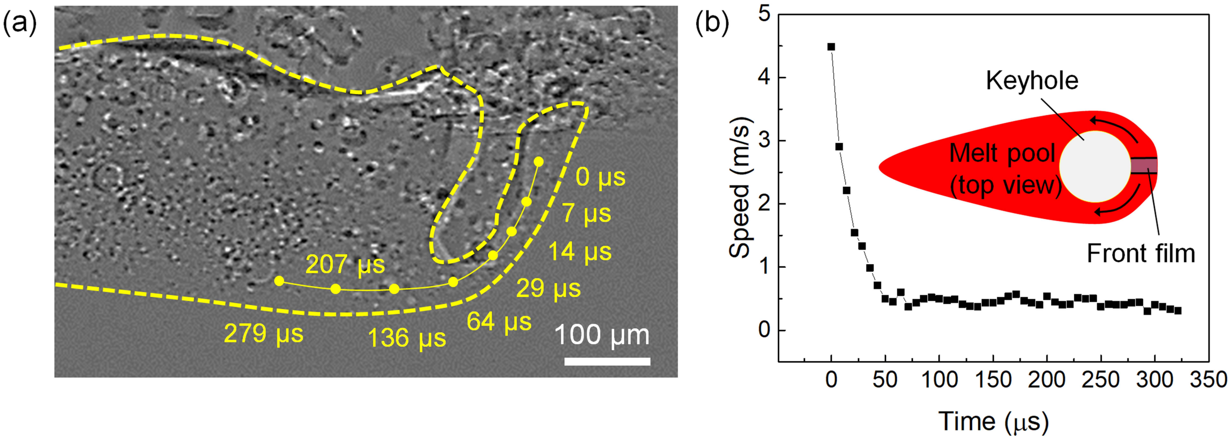

Figure 34. Quantification of a flow tracer moving along the front keyhole wall. (a) X-ray image showing a tracer's trajectory traveling along the front keyhole wall. Note that the yellow dot size does not represent the actual size of the tracer. (b) The speed of the tracer as a function of time. Original figure from [59].

This tracer is unique because its trajectory was rarely seen during the experiments. As illustrated in Figure 30(d), if a tracer wants to move down along the liquid film ahead of the keyhole, it needs to experience flow A and then flow B. However, due to the coaction of the vortex ① and the strong side flow C, most tracers entering the keyhole front will be dragged to other directions. Only the ones that happen to be at the exact center of the keyhole front film could continue to flow downward, as illustrated by the inset in Figure 34(b). Therefore, the tracer being tracked in Figure 34(a) must have moved in the y-z plane with a minimum speed component in the x-direction. This tracer's speed can then reflect the speed of the downward flow ahead of the keyhole. Figure 34(b) indicates that its speed dropped dramatically in the liquid film ahead of the keyhole, decreasing by around 90% from 4.5 m/s (at 0 μs) to 0.45 m/s (at 64 μs), and then became relatively stable when it entered the main body of the melt pool.

5.5 Validity of Flow Tracing by Tracer Particles

The major assumption of the flow tracing approach is that the tracer movement can reflect the surrounding liquid flow movement. The validity of this assumption is evaluated and demonstrated in this section.

5.5.1 Settling Velocity of Tracer Particles

Settling velocity is the terminal velocity for a free-fall particle in the liquid that only has gravity, buoyancy, and friction force. A large settling velocity of an object usually means it tends to "sink" in the liquid. The settling velocity of a tungsten particle in liquid AlSi10Mg can be calculated by Stokes's law:

$$v_p = \frac{\rho_p - \rho_f}{\gamma \mu_f} g d_p^2 \qquad \text{Eq. 21}$$

where, g is the gravitational acceleration, d_p is the diameter of the particle, ρ_p is the mass density of the particle, ρ_f is the mass density of the fluid, μ_f is the dynamic viscosity of the fluid, γ is a coefficient that depends on the fluid and particle viscosity: $\gamma = 12[(\mu_f + \frac{3}{2}\mu_p)/(\mu_f + \mu_p)]$. γ = 18 in the case of solid particles ($\mu_p = \infty$). Taking g = 9.8

m/s^2, d_p= 5×10^{-6} m, ρ_p= 19,300 kg/m^3, ρ_f= 2,440 kg/m^3 (at T_m = 870 K), μ_f = 0.00175 kg/(m·s), the settling velocity is calculated to be v_p = 1.3×10^{-4} m/s.

The calculated settling velocity is at least two orders of magnitude lower than the flow speeds measured in the experiments, meaning that the surrounding flow must strongly influence the detected tracer speed. Otherwise, the tracer velocity will be closer to the settling velocity. To further confirm that the high-density tungsten micro-tracer does not affect the tracing results in this work, gas pores (almost zero density) were used as complementary tracers. It was observed that the pore movement in the main body of the melt pool is consistent with the tungsten particle movement. However, pores cannot be used as melt flow tracers in the keyhole region. The mechanism for this discrepancy was reported in [39].

5.5.2 Acceleration of Tracer Particles

To examine whether the tracer can be accelerated fast enough by the surrounding liquid, the tracer in Figure 34(a) was investigated as an example because this tracer represents the highest speed (> 4.5 m/s) measured in the present work. Assuming the particle was accelerated from the top surface at the keyhole front (with an initial speed of zero) to the position marked by 0 µs (with a speed of 4.5 m/s) within one frame (7 µs), the maximum acceleration can be calculated as 6.4×10^5 m/s^2, which is equivalent to a force of 0.81 µN by Newton’s second law. Given the driving force of the particle is the drag force by the molten aluminum, the drag force was calculated by the Schiller-Naumann drag law [116] as:

$$F_d = \frac{3m_p}{4d_p} C_D v^2 \qquad \text{Eq. 22}$$

where m_p is the particle mass, d_p is the particle diameter, v is the relative velocity, C_D is the Schiller-Naumann drag coefficient, which is given by:

$$C_D = \frac{24}{Re_p}(1 + 0.15 Re_p^{0.687}) \qquad \text{Eq. 23}$$

where the particle Reynolds number is $Re_p = \rho d_p v / \mu$, with the viscosity μ. Taking v = 4.5 m/s, ρ = 1,740 kg/m^3 (near T_b = 2,743 K), μ = 0.0004 kg/(m·s) (near T_b = 2,743 K), the drag force was calculated to be F_d = 4.2 μN, which can give the particle an acceleration of 5 times as much as it really needs.

Considering that the drag force will decrease when the speed difference between the tracer and the flow becomes smaller, the total acceleration time can be estimated by iteration with small time steps. Assuming the initial tracer speed is zero, the surrounding flow speed is 4.5 m/s, and the iteration time step is 1×10^{-8} s, it was calculated that the tungsten particle can be accelerated to over 50% of the surrounding flow speed within 1.4 μs. Furthermore, within one frame (~7 μs), the tracer speed can be accelerated to over 85% of the flow speed. Since the motion delay between the micro-tracer particle (5 μm in size) and the surrounding flow is negligible, the tracers' movement can reasonably reflect the liquid flow in the present experimental conditions.

5.5.3 Effect of Tracer Particle on Liquid Properties

To ensure the tungsten tracer particles do not have a significant impact on the liquid aluminum property, the viscosity of the mixture was calculated by [117]:

$$\mu_m = \mu_f(1 + 2.5\phi + 10.05\phi^2) \qquad \text{Eq. 24}$$

where ϕ is the volume fraction of the tungsten particle. Taking ϕ = 0.01, the mixture viscosity was calculated to be μ_m = 1.026μ_f. Therefore, the liquid mixture with 1 vol.% tracer particles has a viscosity of 2.6% higher than the pure liquid aluminum. In practice, the viscosity will increase by less than 2.6% because the tracer concentration in the liquid will be lower than 1 vol.%, considering that the substrate does not contain tracer particles before melting. Besides, none of the experiments exhibited significant local particle density variation, e.g., clusters or aggregations, in the melt pool. Thus, mixing 1 vol.% tungsten particles into feedstock powder will not significantly alter the viscosity of the liquid and the flow pattern in the melt pool.

To examine whether adding 1 vol.% tungsten particles to the aluminum powder bed could change the laser absorption behavior, two laser-melting experiments were conducted using different powders on the powder bed but with identical laser processing conditions (364 W, 0.5 m/s). The results are displayed in Figure 35. Figure 35(a) shows that AlSi10Mg powder mixed with 1 vol.% tungsten particles generated a keyhole depth of 200 ± 24 μm (averaged over 100 frames). The keyhole developed with pure AlSi10Mg powder bed exhibited an average depth of 197 ± 31 μm, as shown in Figure 35(b), which is only 1.5% smaller than the keyhole depth generated with a mixed powder bed. Therefore, the influence of 1 vol.% tungsten on laser absorption is minimal.

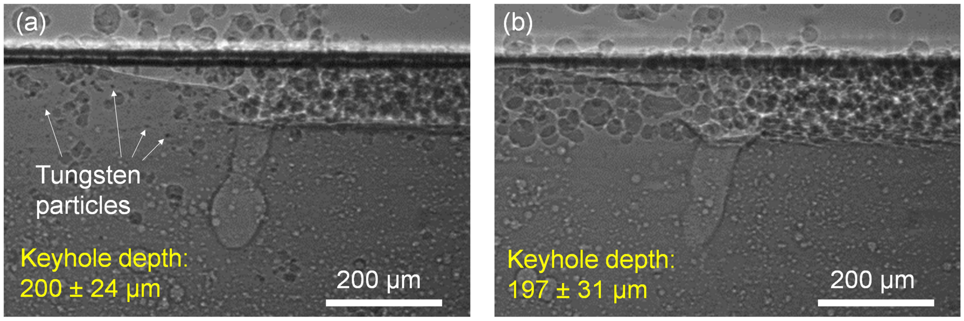

AlSi10Mg + 1 vol% tungsten AlSi10Mg

Figure 35. Comparison of keyhole depth during laser melting of AlSi10Mg + 1 vol.% tungsten mixed powder and pure AlSi10Mg powder. The laser processing parameters are identical between experiments. Original figure from [59].

5.6 Analysis of Driving Forces for Liquid Flow in the Melt Pool

The complex flow patterns revealed in this work have not been completely replicated by the models and simulations published. To understand the physics underlying melt flow pattern, the driving forces in the melt pool that account for the various flow patterns observed in different regions are analyzed and discussed in this section.

5.6.1 Types of Driving Forces in the Melt Pool

There are five major driving forces in the melt pool. Marangoni force drives the flow from high-temperature region to low-temperature region for a material with a negative temperature coefficient of surface tension (from low surface tension region to high surface tension region, most metals and alloys exhibit negative temperature coefficient of surface tension) [36,55,118–120]. Vaporization-induced recoil pressure exerts an inward pressure normal to the vaporization surface [121,122]. A high-speed vapor plume (which can reach 10^2–10^3 m/s [93]) can induce shear force through friction at the liquid-gas interface [119,123]. Hydraulic pressure can exchange energy by either pressure (hydrostatic pressure) or by momentum (hydrodynamic pressure) [124]. Buoyancy force drives liquid along density gradient [29,124,125]. The details about each type of driving force are discussed below.

- *Marangoni effect in the melt pool*

The Marangoni effect is a major driving force in the melt pool [36,118–120]. A dimensionless number, Marangoni number (Ma), is often used to evaluate the relative effect of Marangoni flow over liquid viscosity [126] as:

$$Ma = -\frac{d\sigma}{dT} \cdot \frac{L\Delta T}{\mu\alpha} \qquad \text{Eq. 25}$$

where $d\sigma/dT$ = -0.31×10^{-4} N/(m·K) is the surface tension coefficient for AlSi10Mg alloy, L = 2.0 mm is the length of the melt pool, $\Delta T = T_b - T_m$ = 1,873 K, $\mu_{1000\ K}$ = 0.014 [g/(cm·s)] is the dynamic viscosity of the liquid AlSi10Mg, and $\alpha_{1000\ K}$ = 4×10^{-5} m^2/s is the thermal diffusivity of liquid AlSi10Mg. The Marangoni number in the AlSi10Mg melt pool was calculated to be Ma = 2,074, indicating a strong Marangoni flow. Physically, a Marangoni flow occurs in liquid with a surface tension gradient induced by the temperature gradient as well as the concentration gradient, as described by [27]:

$$\frac{\partial\sigma}{\partial T} = -A - R\Gamma_s \ln(1 + K\alpha_s) - \frac{K\alpha_s\Gamma_s\Delta H_0}{T(1 + K\alpha_s)} \qquad \text{Eq. 26}$$

and

$$K = k_1 \exp\left(-\frac{\Delta H_0}{RT}\right) \qquad \text{Eq. 27}$$

where A is the absolute value of the surface tension temperature coefficient, R is the universal gas constant, Γ_s is the surface excess at saturation, k_1 is a constant related to the segregation entropy, ΔH_0 is the standard heat of adsorption, α_s is the activity of an active element. Since there is usually no surface-active agent in aluminum alloys [127], the surface tension coefficient is always negative ($\partial\sigma/\partial T$ < 0) in the present work, which means the Marangoni flow in the melt pool is temperature-dependent, thus has a trend of moving from the hotter region to cooler region. A flow driven purely by thermal gradient is also called thermocapillary flow. The typical feature of Marangoni flow in a melt pool is the outward flow at the laser heating spot, i.e., the surface flow ahead of laser beam moves forward while the surface flow behind the laser beam moves backward. However, extra attention must be paid to the following circumstances: adding surface active agents [27,34,55,128,129], applying high-speed shielding/carrier gas directly to the melt pool (such as DED additive manufacturing) [130], changing processing atmosphere [34,35,116,131,132], and applying electromagnetic field (such as laser-arc hybrid melting) [34,127,133]. These operations can potentially reverse the direction of thermal-induced Marangoni flow.

- *Vaporization-induced forces in the melt pool*

Vaporization is another major driving force for liquid flow in laser melting [28,29,52], particularly under the keyhole mode in which intense vaporization occurs. Vaporization has two simultaneous—yet different—effects on the keyhole: the recoil pressure pushing the liquid downward [121,122] and the upward metallic vapor plume sprouting out of the keyhole outlet [119,123]. Consequently, the flow around the lower part of the keyhole tends to move down, while the flow near the upper keyhole walls tends to move up [28,122,128]. Vaporization is an essential factor that accounts for some defects in laser-processed parts. For instance, the excess recoil pressure can change the local curvature of the keyhole and generate pores in the melt pool [31]; also, the high-speed vapor plume may interact with the keyhole rim and shear off droplets out of the melt pool as spatters [32,42].

- *Hydraulic pressure in the melt pool*

The effect of hydraulic pressure includes hydrostatic pressure and hydrodynamic pressure. Assuming the liquid is incompressible and the variation of gravitational acceleration is negligible (g = constant), the hydraulic pressure can be approximated by [124]:

$$P_h = P_{static} + P_{dynamic} = \rho g \Delta h + \frac{1}{2}\rho v^2 \quad \text{Eq. 28}$$

where Δh is the depth of the test area from the reference position, v is the fluid speed. Since the hydraulic pressure is determined by the position and the velocity of the flow, it plays an important role in the following events happening in the melt pool: (1) evacuating the fluid out of the liquid film ahead of the keyhole, (2) rebounding the flow at the melt pool boundary, (3) changing the flow direction by dragging the fluid into low hydraulic pressure region, (4) exchanging momentum when two flows encounter each other.

- *Buoyancy force in the melt pool*

The density of liquid metal varies with temperature. In a melt pool, the buoyancy force (B) is a function of density gradient [29,124,125], as expressed by:

$$B = \rho g \beta \Delta T \quad \text{Eq. 29}$$

where β is the thermal expansion coefficient, ΔT is the temperature difference among the convective liquid flow. Generally, the effect of buoyance force is believed to be less significant than the Marangoni force in laser processing [116,123]. The dynamic Bond number (Bo) [126] can be used to assess the relative effectiveness of buoyance force and Marangoni force in the form of:

$$Bo = \frac{\rho g \beta L^2}{d\sigma / dT} \qquad \text{Eq. 30}$$

Taking β = 2×10^{-4} K^{-1} for liquid AlSi10Mg, the dynamic Bond number is estimated to be Bo ≈ 0.1, which indicates the density effect is less than the surface tension effect. However, the buoyance force does play a role in the melt pool in the case where the hot liquid enters the melt pool bottom and floats up [134]. The buoyance force may also assist the upward flow along the upper keyhole walls [133], but the contribution may be small compared with the strong effect of the vapor plume.

5.6.2 Effect of Driving Forces on the Melt Flow Pattern

In a conduction-mode melt pool, the dominating driving force is the Marangoni force, which drives the melt flow from the hotter region to the cooler region (the materials in this study have a negative temperature coefficient of surface tension), i.e., from laser heating spot to melt pool boundary. Therefore, in the longitudinal view [Figure 29(b)], the surface flow ahead of the laser beam moves forward, while the one behind the laser beam moves backward. When the flows reach each edge of the melt pool, they will move downward and return to the laser heating spot under the effect of hydraulic pressure. Thus, two close loops are formed: a clockwise loop ahead of the laser beam and a counterclockwise loop behind the laser beam. Driven also by Marangoni force, the flows in the transverse view [Figure 29(d)] form another two close loops (also observed by [55]), following a similar mechanism as in the longitudinal view.

The flow pattern in the keyhole-mode melt pool is rather complex due to the intense vaporization-induced keyhole. The vaporization-related forces, i.e., the recoil pressure and the vapor plume friction, dominate the flow pattern around the keyhole [the "Head" region in Figure 30(d)]. The flow around the upper part of the keyhole moves upward under the effects of both Marangoni force [28] and the vapor plume friction [14,30], while the flow close to the bottom of the keyhole moves downward due to the recoil pressure, as can be seen in both longitudinal view [Figure 30(d), flow B] and transverse view [Figure 30(f)]. The flow that bypasses the keyhole is mainly driven by a hydraulic pressure gradient, as a high-hydraulic pressure region is formed in the liquid film ahead of the keyhole while the front keyhole wall keeps "pressing" the front liquid during its traveling. Note that the upward flow VI in vortex ① may temporarily disappear or enhance, which is hypothesized to depend on the competition between the downward recoil pressure and the upward vapor plume friction on the front keyhole wall [119,122,123]. With the proceeding of the keyhole, a low hydraulic-pressure region forms behind the bottom of the keyhole [135], which drains the surrounding liquid into this region and thus induces the vortex ②.

For the "Body" part of the melt pool, as shown in Figure 30(d), the surface flow moves backward from the high-temperature region to the low-temperature region (Marangoni force), similar to the condition of conduction-mode melting. The flow at the bottom (flow I) inherits the momentum from flow B and thus moves backward. Being freshly heated up at the keyhole, the flow I carries higher temperature liquid (with lower density) than those in the upper level within the melt pool. Therefore, the molten metal in flow I floats up (flow IV) under the buoyancy force during the backward transportation.

The flow in the middle level of melt pool (flow D and V), aside from the upward movement, has a main tendency of moving forward, attracted by the low hydraulic pressure region around keyhole induced by the high-speed flows under Bernoulli's effect. At the "Tail" region of melt pool, the backward flow on the surface is driven by Marangoni force, while the flow II is generated when the surface flow bounces back at the melt pool rim. During the colliding of flows I and II, the momentum transfers from flows I and II to their merged flow—flow III.

5.7 Analysis of Physical Processes in the Melt Pool

Based on the quantitative analysis in Section 5.4, physical processes associated with kinetic energy damping and heat transfer were analyzed at different locations in the melt pool and discussed below.

5.7.1 Liquid Momentum versus Surface Tension

The extent of damping the flow, especially on the surface (mainly dominated by Marangoni convection), can be expressed by Weber number (We) as [133]:

$$We = \frac{\rho v^2 L}{\sigma} \qquad \text{Eq. 31}$$

where ρ is the liquid density, v is the flow speed, L is the characteristic length, and σ is the surface tension. The Weber number was calculated to be We = 1.78 near the keyhole and We = 0.007 near the melt pool tail. It means that the inertia of the liquid overcomes the surface tension near the keyhole region (where Marangoni convection and recoil pressure are strong), then becomes much less critical when approaching the tail of the melt pool, as schematically shown in Figure 30(d). Consequently, the melt pool surface at the head of the melt pool is more rippled, caused by the momentum of upward liquid along the rear keyhole wall, while the surface at the tail of the melt pool is relatively flat and smooth because the surface tension will damp out the surface wave.

5.7.2 Heat Conduction versus Heat Convection

To improve the computing efficiency and speed, some modeling work (based on heat transfer theories) on laser processing choose only to consider the effect of heat conduction while neglecting the impact of heat convection [28,136]. However, the heat convection could be significant at the heat of the melt pool. With the flow speed measured in this study, the relative effect of heat convection over heat conduction can be evaluated by the Péclet number (Pe), which is the product of the Reynolds number (Re_L) and Prandtl number (Pr), in the form of:

$$Pe = Re_L \cdot Pr = \frac{\rho v L}{\mu} \cdot \frac{c_p \mu}{k} = \frac{L v}{\alpha} \qquad \text{Eq. 32}$$

where L is the characteristic length, v is the local flow speed, and α is the thermal diffusivity. Based on the measurement in Figure 33(a), v = 1.25 m/s, α = 6.6×10^{-5} m^2/s in section Y1 near the keyhole; and v = 0.08 m/s, α = 3.54×10^{-5} m^2/s in section Y12 near the tail of melt pool. The characteristic length (L) is chosen as the hydraulic diameter (D_h) of the melt pool. Hydraulic diameter is commonly used to describe flow moving through non-circular pipes or channels, as defined by:

$$D_h = \frac{4A}{P_w} \qquad \text{Eq. 33}$$

where A is the cross-section area of the flow and the P_w is the wetted perimeter of the cross-section. Considering the melt pool as a channel with a cross-section shape of half ellipse, one radius of the ellipse is the melt pool depth, while the other radius is half of the melt pool width. In Figure 33(a), section Y1, the melt pool depth is 313 µm, with a width of ~500 µm. The hydraulic diameter was calculated to be 539 µm. In section Y12 of Figure 33(a), the melt pool depth is 248 µm with a width of 396 µm. The hydraulic diameter is calculated to be 427 µm.

The Péclet number was calculated to be Pe(head) = 10.2 at the head of the melt pool and Pe(tail) = 0.9 at the tail. When Pe $\geqslant$ 10, qualitatively, heat convection is considered to make a greater contribution to the thermal energy transportation [128]. The results suggest a strong heat convection could occur at the head of the melt pool while heat conduction dominates at the tail of the melt pool. The prevailing physical processes along the melt pool are indicated in Figure 30(d).

5.8 Summary and Conclusions

For the first time, the present work revealed and quantified the melt flow dynamics in every location of the entire melt pool in laser metal additive manufacturing under conduction-mode and keyhole-mode melting. The major conclusions are detailed below:

(1) A full-field melt flow mapping method was developed to reveal the detailed melt flow dynamics under laser metal additive manufacturing conditions by tracing uniformly dispersed populous micro-tracers through in-situ high-speed high-resolution X-ray imaging.

(2) The melt flow behaviors were revealed in every location of the whole melt pool under conduction-mode and keyhole-mode melting in the laser additive manufacturing process. The conduction-mode melt pool possesses a simple flow pattern that is mainly driven by the Marangoni effect. The flow pattern in the keyhole-mode melt pool is rather complex, under the coaction of multiple driving forces. The flow pattern and flow speed are location-dependent. The detailed

(projectional) flow speeds in different regions of the melt pool under both conduction-mode and keyhole-mode melting were quantified in terms of average speed and maximum speed. Decreasing flow speed from the keyhole to the melt pool tail was observed and statistically analyzed.

(3) The driving forces for different types of melt flow were analyzed. The Marangoni effect accounts for the flow movement from the high-temperature region to the low-temperature region (for a material with a negative temperature coefficient of surface tension) on the surface of the melt pool. Vaporization dominates the fluid flow along depression-zone walls. Hydraulic pressure drives fluid flow from high-pressure region to low-pressure region. Buoyancy force accounts for liquid convection from low-density region to high-density region.

(4) The prevailing physical processes concerning kinetic energy damping and heat transfer at the head of the melt pool were experimentally identified to be liquid inertia and heat convection, respectively. In contrast, at the tail of the melt pool, the corresponding physical processes were determined to be surface tension and heat conduction.

Chapter 6: Melt Flow Related Process Instabilities

This chapter contains experimental data and results that have been published in the following work:

Q. Guo, M. Qu, L.I. Escano, S.M.H. Hojjatzadeh, Z. Young, K. Fezzaa, L. Chen, Revealing melt flow instabilities in laser powder bed fusion additive manufacturing of aluminum alloy via in-situ high-speed X-ray imaging, Int. J. Mach. Tools Manuf. 175 (2022) 103861. [115]

The publication rights for this section are given in Appendix A. Appropriate recognition is given to the relevant citation for the material in which it was originally published. The presented material represents my contributions and material collected with or by a collaborator has been highlighted as such.

This chapter reports the mechanisms of the melt flow instabilities in the LPBF process revealed by in-situ X-ray imaging with the flow tracing approach developed in Chapter 5. Unlike Chapter 5, which focuses on characterizing the regular melt flow (ideal, stable flow without disturbances), this chapter (Chapter 6) focuses on revealing the stochastic melt flow instabilities intrinsic to the process. The first half of this chapter (Sections 6.1–6.3) introduces the formation mechanisms of three major types of melt flow instabilities and their influences on the part quality. The second half of this chapter (Sections 6.4 and 6.5) provide new insights into the melt flow evolution path and keyhole oscillation mechanisms.

6.1 Powder/Droplet Impact Induced Melt Flow Instability

The flowable powder, as the core and unique element in the dominating powder-based laser metal additive manufacturing technologies, enables great flexibility for process design but also brings frequent disturbances to the process [46]. Two types of powder-induced melt flow instabilities are reported below.

6.1.1 Local Instability Induced by Powder/Droplet Impact

In the laser metal additive manufacturing process, a laser-driven proceeding melt pool continuously captures the powder on the powder bed to grow into a part. However, the incorporating powder can be large (more than three times larger than the feedstock powder) due to agglomerations or the merging of small droplets. The impact of large powder clusters or droplets into a melt pool with a large melt volume (i.e., keyhole-mode melt pool) could locally disturb the regular melt flow pattern, as elucidated in Figure 36.

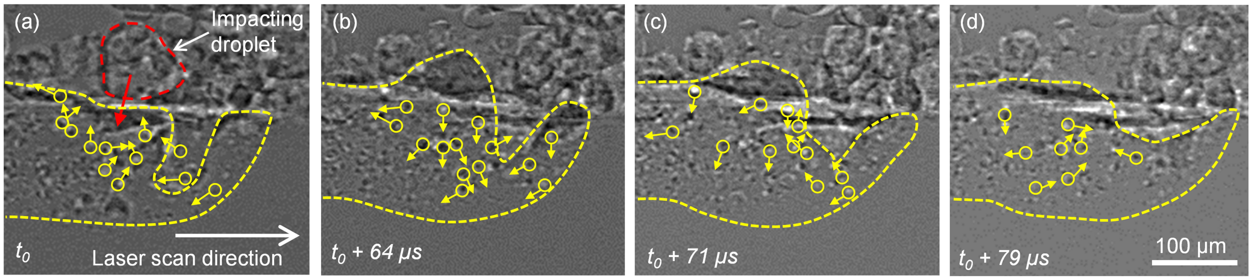

Regular flow Powder/droplet impact Momentum transfer Keyhole vanishing

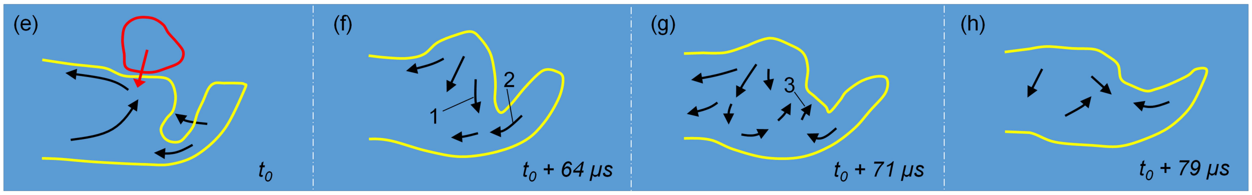

Figure 36. Powder/droplet impact induced local melt flow instability. (a–d) X-ray images showing the melt flow change during a droplet impacting keyhole-mode melt pool. The laser power is 312 W with a scan speed of 0.6 m/s. The material is AlSi10Mg. (e–h) Schematic illustration of the melt flow change in (a–d). Original figure from [115].

Figure 36(a–d) displays X-ray images where a melt pool moves from left to right in the field of view. Yellow dashed lines marked the melt pool boundaries. The laser is invisible in the view, whereas its location was indicated by the moving keyhole. The flow tracers were circled with arrows pointing out their instant moving directions. By connecting the movements of individual tracers, the melt flow patterns were deducted and schematically exhibited in Figure 36(e–h).

During an impact, the droplet transfers kinetic energy and potential energy into the melt pool, locally altering the original flow direction [Figure 36(a, e)] into the droplet momentum direction [Figure 36(b, f)] at the impact location. The collision between foreign flow (carrying liquid from the droplet) and the original flow (carrying liquid from the melt pool) exhausted the impact energy and dampened the droplet impact from spreading further. The downward flows 1 and 2 [Figure 36(f)] collided at the keyhole bottom and formed an upward flow 3 [Figure 36(g)], pushing the keyhole bottom surface upward till the depression almost vanished [Figure 36(d, h)]. Although keyhole vanishing is momentary, it can reduce the local laser absorption and cause undesired energy fluctuation in the process [37].

6.1.2 Global Instability Induced by Powder/Droplet Impact

Compared with the above keyhole-mode laser melt pool, a conduction-mode laser melt pool contains much less liquid volume, which cannot efficiently dampen and confine the powder/droplet impact within a local region. Rather, the melt flow instability brought by the impact on the conduction-mode melt pool is global and more detrimental, as demonstrated in Figure 37.

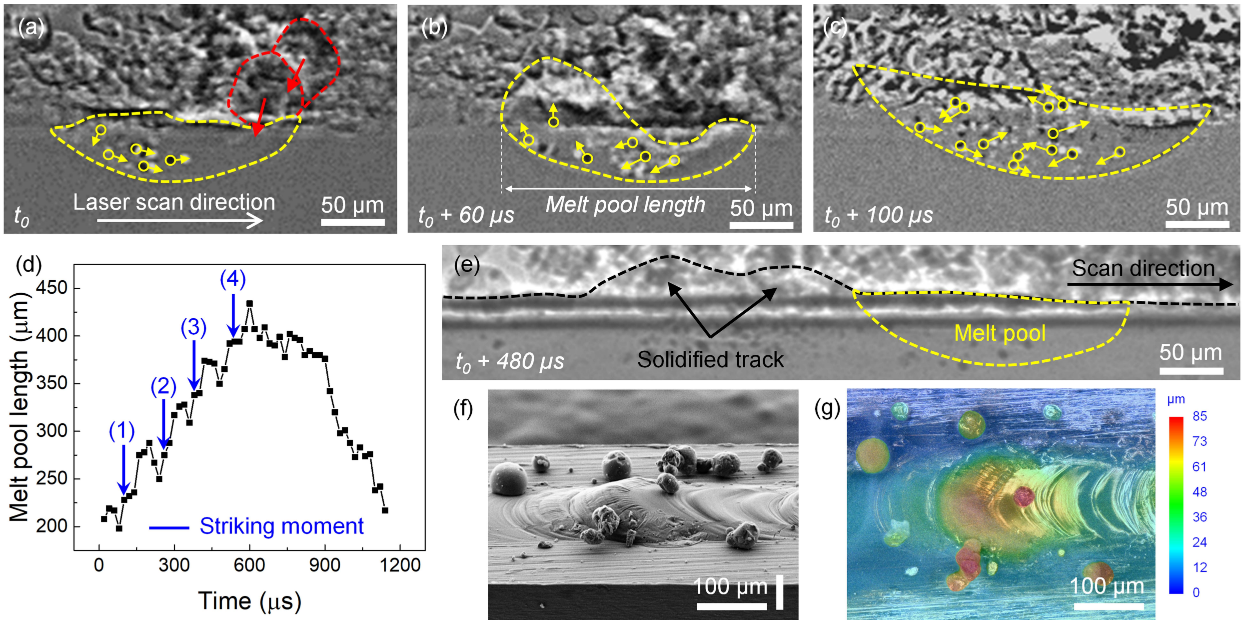

Figure 37. Powder/droplet impact induced melt flow instability. (a–c) X-ray images showing the melt flow change during a droplet impacting to conduction-mode melt pool. The laser power is 312 W with a scan speed of 0.6 m/s. The material is Al-6061. (d) Effect of droplet striking on the melt pool length development as a function of time. (e) X-ray image showing the profile of the solidified melt track resulting from droplet impact. (f) SEM image showing the solidified track at the same region as in (e). (g) The surface profile of the solidified track at the same imaging area as in (e) and (f). Original figure from [115].

During an impact, as shown in Figure 37(a), two droplets carrying a liquid volume of nearly one-third of a conduction-mode melt pool struck on the front melt pool surface. The impact broke the original regular flow pattern in the whole melt pool, as evidenced by the reversed flow direction at the rear-bottom of the melt pool, which changed from moving forward [Figure 37(a)] to backward [Figure 37(b)]. The surface level at the rear melt pool was kicked up by the striking [Figure 37(b)] and rapidly solidified as it is [Figure 37(e, f)], adding up to the surface roughness of the as-printed layer. Surface profiling measurement in Figure 37(g) shows the elevated track height can be 50 μm higher than the average solidified track height. The impact droplet also increases the volume of liquid metal in the melt pool, leading to melt pool elongation, as shown in Figure 37(c).

Large powder/droplet impact is not a rare event in the laser metal additive manufacturing process. The striking incidence was quantified by evaluating the melt pool length change in 1200 μs during laser scanning, as shown in Figure 37(d). Four striking events happened within the first 600 μs, leading to a continuous elongation of the melt pool from ~200 μm to 434 μm (over 100% increase). It was observed that the droplet-striking event did not elongate the melt pool immediately. The elongation usually occurs 20-60 μs after the striking because the striking liquid takes time to travel along the melt pool. No striking event happened for the remaining 600 μs [from 600 μs to 1200 μs in Figure 37(d)], during which the melt pool length gradually recovered to the original size. This result demonstrates that the powder/droplet striking occurs frequently and randomly during laser scanning, which brings uncertainty to the qualification of additively manufactured parts.

6.2 Significant Keyhole Oscillation Induced Melt Flow Instability

The melt flow patterns around the keyhole highly depend on the keyhole behavior. A significant keyhole oscillation with amplitude over twice as large as the original keyhole size can override the original flow patterns in adjacent areas.

6.2.1 Local Instability Induced by Significant Keyhole Oscillation

When a significant keyhole oscillation happens, the liquid at the rear keyhole wall was pushed backward to form a surface wave, as shown by the X-ray images in Figure 38(a, b) and the schematic illustrations in Figure 38(e, f). The wave front I [Figure 38(f)] squeezed the rear rim of the keyhole to generate a protruding surface wave, which propagated backward against the laser scanning direction.

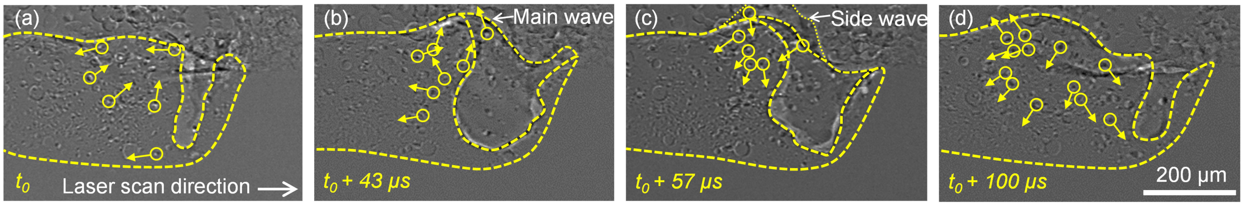

Regular flow   Keyhole oscillation   Wave formation   Wave propagation

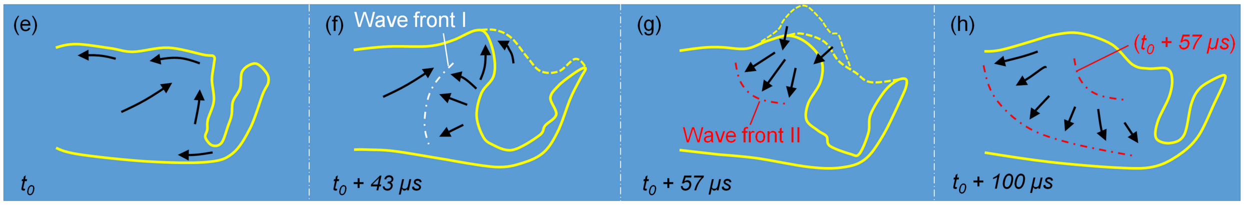

Figure 38. Significant keyhole oscillation induced local melt flow instability. The laser power is 364 W with a scan speed of 0.6 m/s. The material is AlSi10Mg. Original figure from [115].

Aside from the main surface wave [as shown in Figure 38(b)], a secondary wave possibly locating at the side of the melt track formed afterward, as displayed in Figure 38(c). The possible configuration that could cause overlaying contrast in X-ray images is demonstrated in Figure 39. The liquid beneath the surface wave got compressed and spread away to a broader area with a speed of ~0.6 m/s [measured by tracing the displacement of wave front II in Figure 38(g, h)]. With the spreading of the compressed wave, the liquid metal in the affected area temporarily moved along the wave-propagating direction. At the same time, the original flow pattern was temporarily erased and overridden.

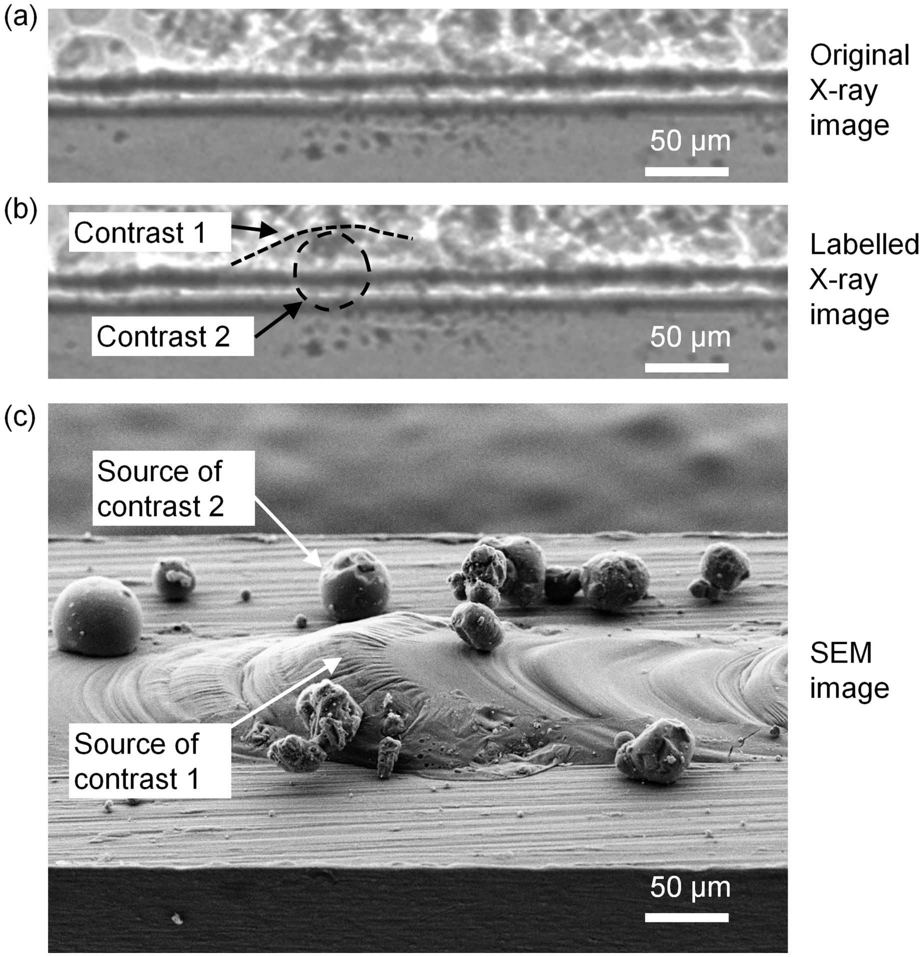

Figure 39. Possible mechanism of causing overlaying contrast in X-ray images. Two contrasts occur at the same location in X-ray images (a, b). However, their locations along the X-ray path are different, as illustrated in (c). Original figure from [115].

6.2.2 Global Instability Induced by Significant Keyhole Oscillation

A global effect takes place when a significant keyhole oscillation occurs in a moderate-size keyhole-mode melt pool or a transition-mode melt pool, as shown in Figure 40. Initially, the oscillation created a backward-moving wave that compressed the liquid behind the keyhole, as shown in Figure 40(b, e), which is similar to the event in Figure 39. However, different from Figure 39, the compressed liquid did not spread far before it touched the bottom of the shallow melt pool, where the liquid split into two flows [Figure 40(c, f)]: flow-1, moving backward to the rear melt pool; and flow-2, moving forward to the front melt pool. The splitting flows initiated a series of instabilities in the process, as demonstrated in Figure 40(g–i):

(1) A reduction in solidification rate occurred at the tail of the melt pool, as indicated by the red arrow in Figure 40(h). Under regular melt flow patterns, as shown in Figure 40(a), the solid-liquid interface at the melt pool bottom was smooth and convex. However, the significant keyhole oscillation pushed a large volume of liquid backward to the rear melt pool, slowing down the solidification at the rear bottom of the melt pool. As a result, a concave was observed on the solid-liquid interface at the middle of the melt pool bottom, as pointed out in Figure 40(h).

(2) The forward-moving flow filled up the keyhole cavity, as shown in Figure 40(g, h), following a similar mechanism to the flow-colliding-induced keyhole closure in Figure 36(f–h).

(3) The backward-moving flow delayed the solidification at the tail of the melt pool due to the extra mass of molten alloy transported to the rear area. As a result, the melt pool elongated from 605 ± 9 μm to 691 ± 10 μm during the event.

(4) An uneven surface of the solidified track was left when the surface wave reached the tail of the melt pool and solidified with an elevated liquid level, as exhibited in Figure 40(i, j). The surface roughness is characterized by surface profiling, as shown in Figure 40(k). The highest point at the uneven solidified track is ~40 μm higher than the average height of the solidified track.

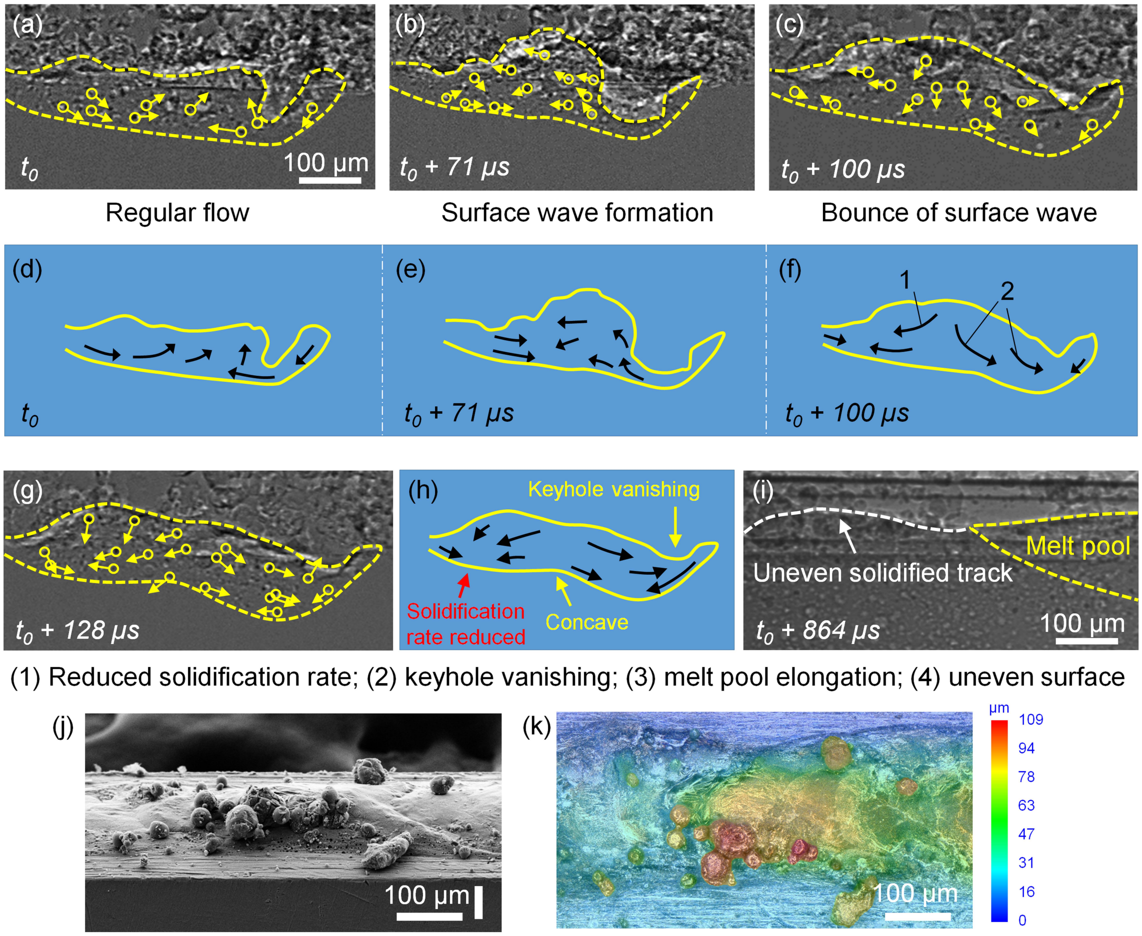

Figure 40. Significant keyhole oscillation induced global melt flow instability. The laser power is 312 W with a scan speed of 0.6 m/s. The material is AlSi10Mg. (a–c) X-ray images showing the formation and propagation of an abnormal surface wave. (d–f) Schematic illustration of the melt flow pattern in (a–c). (g, i) X-ray images showing the consequences induced by the melt flow instability. (h) Schematic illustration of the melt flow pattern in (g). (j) SEM image of the solidified track in (i). (k) Surface profile of the solidified track in (i) and (j). Original figure from [115].

So far, Sections 6.1 and 6.2 have revealed the melt flow instabilities induced by powder/droplet impact and significant keyhole oscillation. Their individual effects on various sizes of melt pools were demonstrated to be different. In brief, the instabilities occurring in a large melt pool tend to influence a portion of the melt pool. In contrast, those occurring in a relatively small melt pool usually trigger a global reaction to the whole melt pool and can be more detrimental to the process.

6.3 Melting-Mode Switching Induced Melt Flow Instability

The aforementioned instabilities occur under a single melting mode without melting-mode transition during scanning. However, a distinct type of melt flow instability can be triggered by the switching of melting modes, which is a common yet often overlooked phenomenon due to the difficulties of investigating/recognizing by ex-situ examinations.

A melting-mode switching event was captured by in-situ X-ray imaging during a continuous laser scanning of a 100 μm thick AlSi10Mg powder on an AlSi10Mg substrate, with a constant laser power of 312 W and a scan speed of 0.6 m/s. Initially, as shown in Figure 41(a), the melt pool was in conduction mode, with no visible keyhole under the laser beam. Indicated by the motion of tracers, the melt flow in the melt pool exhibited a pattern consistent with the conduction-mode flow pattern reported in Chapter 5. However, the melting mode switched into transition mode after 0.5 ms without any change in processing parameters, as shown in Figure 41(b). By connecting the moving directions of individual tracers, the overall flow pattern in the transition-mode melt pool was mapped out and schematically illustrated in Figure 41(c). The front half (keyhole-adjacent region) of the melt pool exhibited a distinct pattern from the conduction-mode flow due to the intensive interruption caused by the keyhole. In contrast, the rear half of the melt pool maintained a similar pattern as the conduction-mode flow. The newly-formed keyhole enhanced the laser absorption [137] and increased melt pool volume. As a result, the melt pool depth increased from 208 ± 10 μm (conduction-mode) to 331 ± 7 μm (transition-mode).

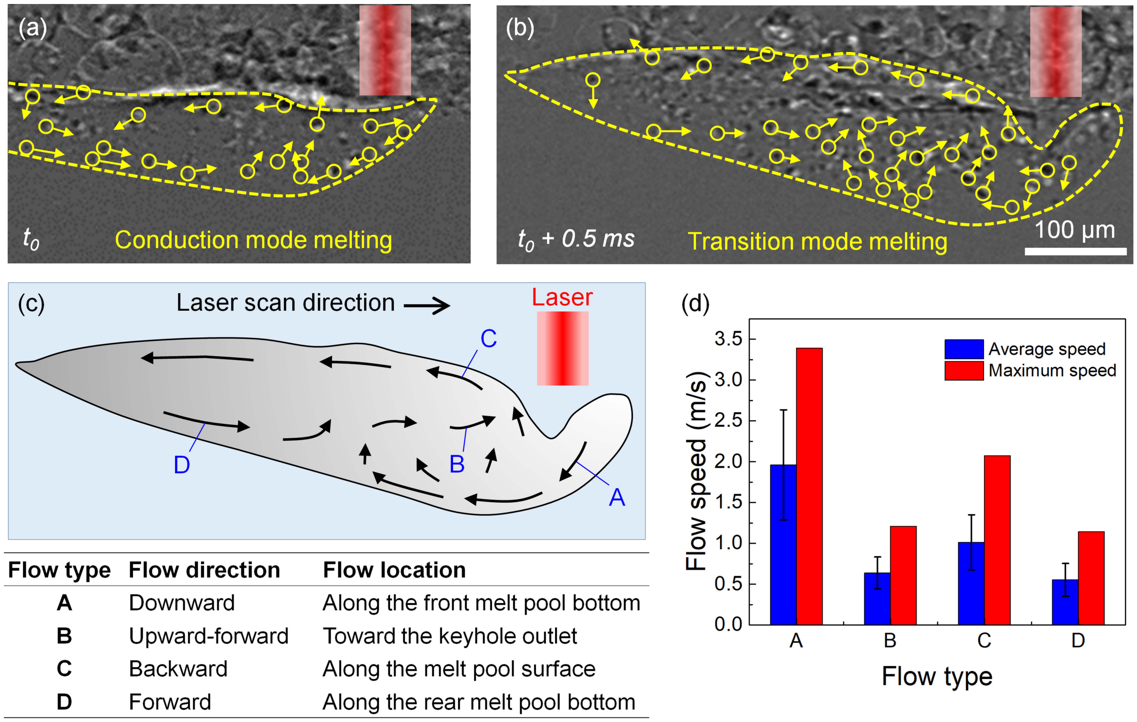

Flow type	Flow direction	Flow location
A	Downward	Along the front melt pool bottom
B	Upward-forward	Toward the keyhole outlet
C	Backward	Along the melt pool surface
D	Forward	Along the rear melt pool bottom

Figure 41. Melting mode switching induced melt flow instability. (a, b) X-ray images showing the melt flow change from conduction mode melting to transition mode melting within 0.5 ms. The laser power is 312 W with a scan speed of 0.6 m/s. The material is AlSi10Mg. (c) Schematic illustration of the melt flow pattern in transition mode melt pool (b). (d) Measurement of melt flow speed in transition mode melt pool. Error bars represent standard deviation, n ⩾ 21 independent replicates. Original figure from [115].

The 2D flow speed in the transition-mode melt pool was quantified by evaluating the tracers' speed at four locations, as shown in Figure 41(c): A—downward flow along the front melt pool bottom; B—upward-forward flow toward the keyhole outlet; C—backward flow along the melt pool surface; and D—forward flow along the rear melt pool bottom. Figure 41(d) displays the four flows' average and maximum speeds. Flow-A has the highest average speed of 1.96 ± 0.68 m/s and a maximum speed of 3.39 m/s. Flow-D exhibited the lowest average speed of 0.55 ± 0.2 m/s and the lowest maximum speed of 1.14 m/s.

The melting-mode switching during laser scanning was not observed with a particular frequency (or period). As shown in Figure 42, the melting-mode switching seems to happen randomly under the processing condition specified in the figure caption.

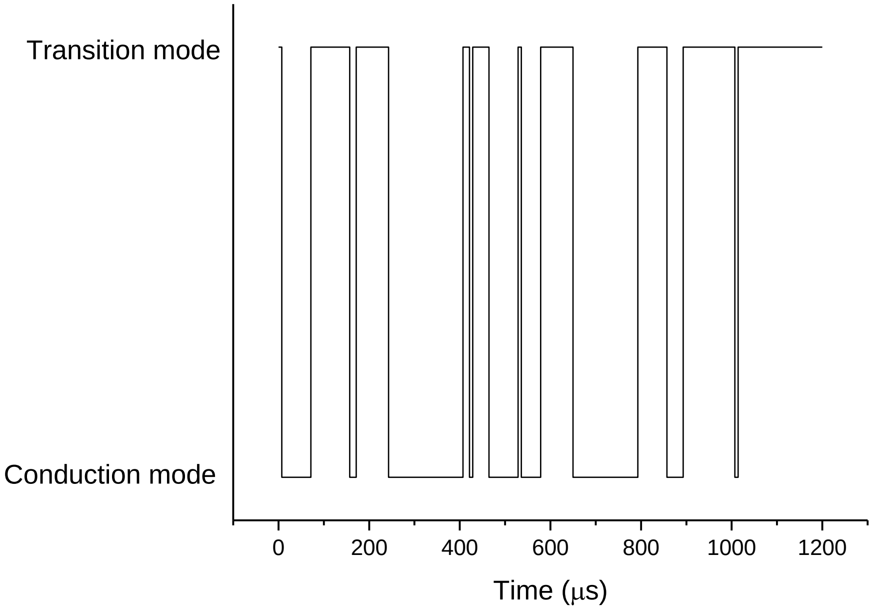

Figure 42. Melting mode switching during a laser single-track scanning experiment. The laser condition is 312 W with 0.6 m/s scan speed. The material is AlSi10Mg alloy. Original figure from [115]

6.4 Melt Flow Evolution among Different Melting Modes

Although the regular melt flow patterns under conduction-mode and keyhole-mode laser melting have been revealed in Chapter 5, it remains unclear how the melt flow pattern changes from a simple flow [conduction-mode flow pattern, Figure 43(a)] to a complex flow [keyhole-mode flow pattern, Figure 43(c)]. Is such change arbitrary? Or is there a pattern to follow? Here, with the missing link identified in this work (transition-mode flow pattern), the complete evolution path of melt flow among different melting modes can be unveiled, as demonstrated in Figure 43.

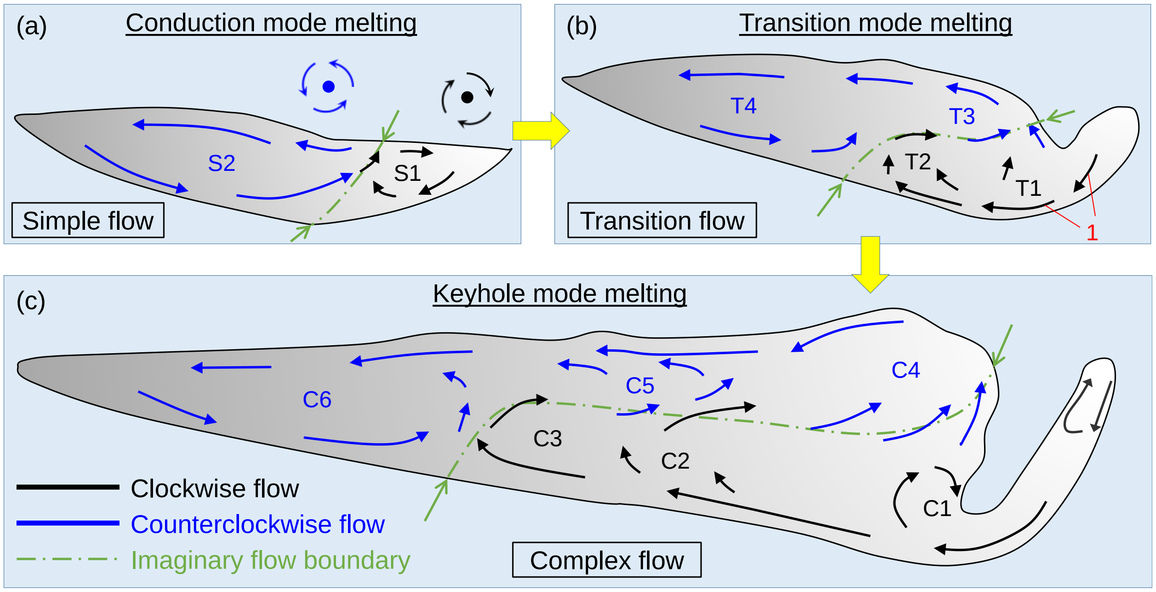

Figure 43. Melt flow evolution among different melting modes. The conduction-mode flow pattern in (a) is adapted from Figure 29(b). The transition-mode flow pattern is adapted from Figure 41(c). The keyhole-mode flow pattern is adapted from Figure 30(d). Original figure from [115]

In general, the complexity of the melt flow increases in scale with the melt pool size (or aspect ratio). The simple flow pattern in a conduction-mode melt pool contains two circulations—a clockwise circulation S1 and a counterclockwise circulation S2, as shown in Figure 43(a). In the transition-mode melt pool [Figure 43(b)], the shallow keyhole exerted extra momentum on the downward flow (flow-1) along the front melt pool boundary, transporting the flow further into the body of the melt pool. Compared with the clockwise circulation S1 in the conduction mode, this region was stretched into two clockwise vortices, T1 and T2, in transition mode. Similarly, the counterclockwise circulation S2 was also elongated into two partial counterclockwise vortices, T3 and T4, as shown in Figure 43(b). When it comes to keyhole mode, in Figure 43(c), the deep keyhole pushed the clockwise flow deeper into the melt pool. Thus, several vortices, C1, C2, and C3, formed along the path. The counterclockwise region was stretched even longer, partitioned by several counterclockwise flows, C4, C5, and C6. Therefore, the melt flow patterns from conduction mode to keyhole mode gain complexity by the expansion of the clockwise region and counterclockwise region, with more vortices forming in each region.

6.5 Mechanisms for Significant Keyhole Oscillation

Section 6.2 has identified keyhole oscillation as an important source of melt flow instabilities. However, the mechanisms for causing significant keyhole oscillation are also various. Previous modeling works have proposed the reflection of the laser beam within the keyhole as a source for causing keyhole fluctuations [138,139]. The uneven distribution of laser energy on the keyhole surface was also identified by multi-physics modeling to cause keyhole fluctuations [65]. Experimental work based on in-situ synchrotron imaging has revealed keyhole oscillations could be induced by opposite flows around the keyhole or by the variation of laser absorption on a nonuniformly-packed powder bed [140]. It was also reported that the presence of powder could also induce keyhole fluctuations [46], yet no detailed mechanisms were revealed. Here in this section, two new powder-based mechanisms for causing significant keyhole oscillations are revealed and discussed.

The first mechanism is laser-blocking induced keyhole oscillation, as demonstrated in Figure 44(a–e). At the stable stage, the laser beam will incident the front keyhole wall [Figure 44(a)]. However, sometimes the powder agglomerate ahead of the laser and form a large, floating droplet on the powder bed [42], as circled by the dashed line in Figure 44(a). Once the moving laser catches up with the droplet, the laser beam could be partially blocked by the droplet [Figure 44(b)]. The front keyhole wall under the blocked beam rose due to the less-intensive vaporization, as shown in the inset of Figure 44(b), leaving a reduced inclination angle (β) of the front keyhole wall as compared with the large inclination angle (α) under regular laser radiation. The overall keyhole size also shrank due to insufficient laser radiation. In the next moment, in Figure 44(c), the localized vaporization on the droplet pushed the droplet to move along the laser scanning direction and left the laser radiation area. A sudden release of the laser energy to the keyhole promoted the intensive vaporization-induced recoil pressure, which expanded the keyhole cavity rapidly. In this manner, the keyhole completed an oscillation cycle by the laser block-unblock-induced keyhole shrinkage-expansion process. The oscillation frequency depends on how often the laser is blocked. For example, two laser-blocking events within 40 μs were captured and displayed in Figure 44(b–d). The oscillation amplitude depends on how much of the laser energy is blocked. For example, the keyhole size only shrank when the laser was half-blocked in Figure 44(b), while the keyhole cavity almost vanished when the laser is nearly fully-blocked in Figure 44(e).

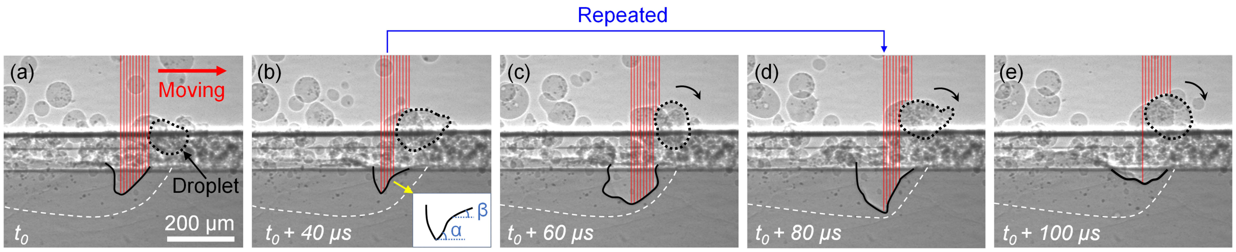

Stable stage | Laser blocking I | Keyhole expansion | Laser blocking II | Laser blocking II-continue

Figure 44. Laser-blocking induced keyhole oscillation. Original figure from [115].

The second mechanism is powder-incorporation-induced keyhole oscillation, as shown in Figure 45(a–e). The beginning of this event is similar to the first mechanism, where a floating droplet on a powder bed formed ahead of the laser beam during laser scanning in Figure 45(a). However, instead of being pushed away, the droplet was captured by the front rim of the melt pool and formed a “tongue”-shape protrusion [Figure 45(b)]. The tongue then collapsed into the keyhole by moving downward along the front keyhole wall [Figure 45(c)]. The inclined tongue, together with the rear rim of the keyhole, formed a throttle at the keyhole outlet [Figure 45(d)], which restricted the exhaust of metal vapor and also guided more laser reflection from the front keyhole wall toward the rear keyhole wall [141]. As a result, the keyhole developed into a pocket shape, with an increased width over three times large as the regular keyhole width. The expanded keyhole persists as long as the throttle exists. However, the keyhole profile will keep being reshaped by the throttle displacement, as shown in Figure 45(e), leading to continuous disturbances to the surrounding area before the throttle fades away.

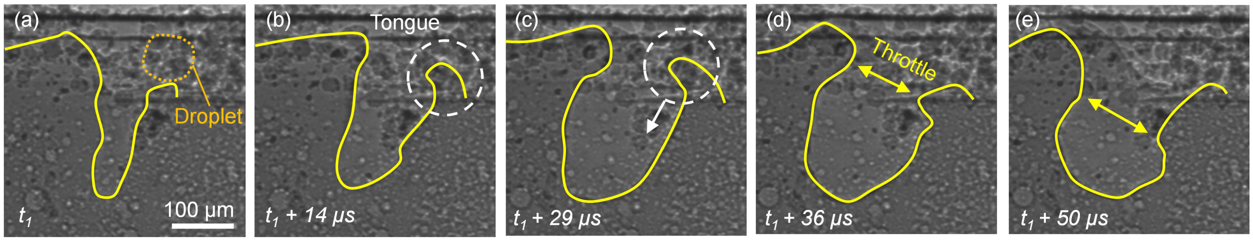

Regular Tongue formation Tongue collapse Throttle formation Keyhole reshape

Figure 45. Powder-incorporation induced keyhole oscillation. Original figure from [115].

It should be noted that all the observations reported here are the projected information on the 2D imaging plane. Although the selected 2D imaging plane does not account for the out-of-plane (3D) particle movement, the tracer movement within the selected imaging plane can fairly reflect the physics underlying flow instabilities. The reasons are: (1) Statistically, the tracers tend to move within the selected imaging plane rather than out of the plane because the melt pool shape in LPBF is usually elongated along the laser scan direction. Chapter 4 has shown that the melt pool length can be several times larger than the width during the LPBF process. (2) The melt flow patterns exhibit more complexity on the selected imaging plane (perpendicular to the X-ray beam) than on the plane parallel to the X-ray beam, as shown in Chapter 5.

Therefore, the instabilities observed on the 2D projection plane are valid and not affected by the out-of-plane (3D) particle movements. However, there may be chances that the instability within the plane parallel to the X-ray beam was missed.

6.6 Summary and Conclusions

In this chapter, the melt flow instabilities in the laser metal additive manufacturing process were experimentally revealed by in-situ high-speed high-resolution synchrotron X-ray imaging. The major conclusions are drawn below:

(1) Three major mechanisms for causing melt flow instabilities were identified as: powder/droplet impact, significant keyhole oscillation, and melting-mode switching. These instabilities can roughen the part surface finish, break the energy balance within the melt pool (by changing the instant laser absorption), and disturb the solidification process at the melt pool solid-liquid interface.

(2) The evolution path of melt flow pattern among different melting modes was unveiled. The melt pool was found to be separated into a clockwise flow region and a counterclockwise flow region. The elongation of the two regions facilitated the melt pool development from simple flow to complex flow.

(3) Two new mechanisms for causing significant keyhole oscillation were identified. One mechanism is the laser-blocking-induced keyhole oscillation, where powder droplets could occasionally block the laser path and reduce the energy input to the

keyhole. The other one is the powder-incorporation-induced keyhole oscillation, where the capturing of new particles reshapes the keyhole profile.

Chapter 7: Phase Transformation Dynamics Informed Alloy Development

---

This chapter contains experimental data and results that have been published in the following work:

Qilin Guo, Minglei Qu, Chihpin Andrew Chuang, Lianghua Xiong, Ali Nabaa, Zachary A. Young, Yang Ren, Peter Kenesei, Fan Zhang, Lianyi Chen, Phase transformation dynamics guided alloy development for additive manufacturing, Addit. Manuf. 59 (2022) 103068. [142]

The publication rights for this section are given in Appendix A. Appropriate recognition is given to the relevant citation for the material in which it was originally published. The presented material represents my contributions and material collected with or by a collaborator has been highlighted as such.

As discussed in section 1.6, the complex heating/cooling condition during AM often leads to undesired phases in the as-printed parts. In this chapter, a 17-4PH stainless steel (UW_17-4) with a redefined composition was developed to withstand the complex thermal condition during AM and can reliably produce the desired martensite phase in the LPBF as-printed part. The alloy development was informed by the understanding of the phase transformation dynamics in 17-4PH stainless steel, which was enabled by the in-situ high-energy high-resolution X-ray diffraction (HRXRD) technique. The experimental method for in-situ HRXRD will be introduced in Section 7.1 instead of in Chapter 2 because this technique is only used in this chapter.

7.1 Materials and Methods

7.1.1 In-Situ Laser-Melting High-Resolution X-Ray Diffraction Experiment

In-situ laser-melting high-resolution X-ray diffraction experiments were performed to probe the phase transformation dynamics in 17-4 PH stainless steel. The experiments were conducted at beamline 1-ID-E of the Advanced Photon Source (APS), Argonne National Laboratory. The experiment used the same laser setup as the X-ray imaging, as described in Chapter 2. The configuration of the laser beam, the X-ray beam, and the sample positioning is schematically shown in Figure 46(a). The sample was placed in a chamber with high purity argon (99.999%) protection during experiments. During laser scanning, a stationary micro-focused high-energy high-flux synchrotron X-ray beam with a wavelength of 0.2022 Å and a beam size of 50 μm × 30 μm (horizontal × vertical) was transmitted through the sample (0.5 mm thick) to form Debye-Scherrer diffraction cones, which were continuously recorded as diffraction rings on a flat plate detector (PILATUS3X-2M, DECTRIS, Switzerland) with a recording frame rate of 250 Hz. The X-ray exposure time for every frame was 1 ms.

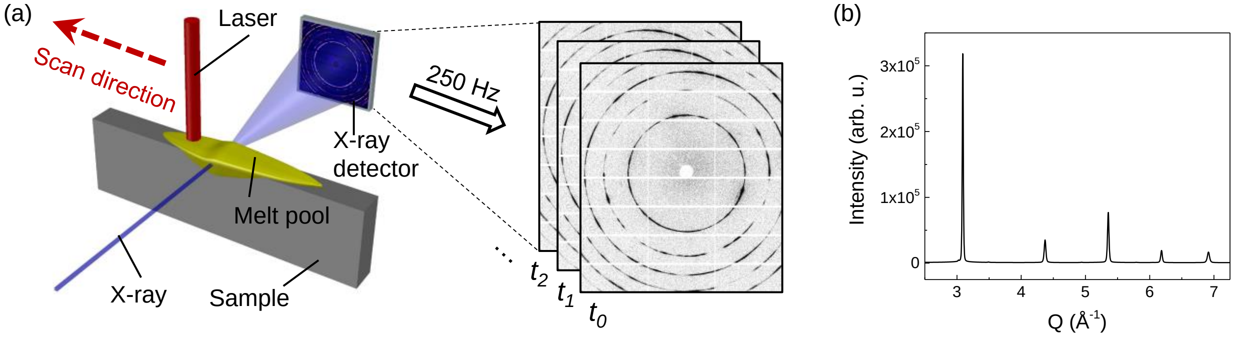

Figure 46. Experimental method for in-situ laser-melting high-resolution X-ray diffraction. (a) Schematic illustration of in-situ laser-melting X-ray diffraction experiment. (b) An example of an integrated 1D XRD pattern from the 2D diffraction pattern in (a). This figure is adapted from [142].

The synchrotron X-ray's high brilliance and high energy (short wavelength) properties ensured the XRD data with a high signal-to-noise ratio and a broad Q-space range (covering more families of crystallographic planes) [143,144]. They also enabled quantitative analysis of the specimen's bulk structural information and prevented uncertainties introduced by surface effect (deformation-induced γ–α' transformation) from sample preparation [78].

7.1.2 XRD Data Analysis

The diffraction rings from each frame were radially integrated by FIT2D software along the entire azimuthal range (0°–360°) to obtain intensity versus Q-vector patterns. Here, $|\boldsymbol{Q}| = 4\pi \times sin(\theta)/\lambda$, where λ is the X-ray wavelength and θ is one-half of the diffraction angle 2θ. Each integrated pattern included 2048 bins in a $|\boldsymbol{Q}|$ range of 26 nm^{-1} to 55.5 nm^{-1}. The peak position and peak intensity were determined by a Voigt function. An example of the integrated XRD pattern is shown in Figure 46(b), revealing the room-temperature phase constitution of commercial additively-manufactured 17-4 PH stainless steel (hereinafter, C_17-4) after laser melting.

Rietveld refinement was performed to quantify the phase fraction from the XRD pattern using GSAS-II software. The reference phase information was from Inorganic Crystal Structure Database (ICSD) with IDs of ICSD-53449 (austenite), ICSD-53452 (delta-ferrite), and ICSD-53451 (alpha-ferrite). A standard CeO2 powder specimen was used to calibrate the experiment configuration. The background, scale factor, lattice constants, grain size, and microstrain were all considered in the refinement.

7.1.3 Small-Angle X-Ray Scattering Experiment

Small-angle X-ray scattering (SAXS) measurement was performed and analyzed by a collaborator (Fan Zhang, Physicist at the U.S. Department of Commerce's National Institute of Standards and Technology) at the ultra-small-angle X-ray scattering beamline 9-ID-C of the Advanced Photon Source, Argonne National Laboratory, to determine the nanoscopic microstructural features in the as-printed 17-4 steel. Because of its Bonse-Hart crystal optics, this instrument provides primary intensity calibration, enabling analysis of absolute volume fraction of scattering inhomogeneities [145]. A standard configuration of this instrument was used to acquire ultra-small-angle X-ray scattering, SAXS, and X-ray diffraction data of the same sample volume across a broad $|\boldsymbol{Q}|$ range from 1×10^{-4} Å^{-1} to 6.5 Å^{-1}. [146] A detailed description of this setup can be found in reference [147]. The X-ray energy was 21 keV, corresponding to an X-ray wavelength of 0.5904 Å. A thin foil of as-built 17-4 steel with a thickness of ~100 µm (transmission of ~14%) was carefully polished to ensure penetration. The data analysis was performed using standard small-angle scattering software Irena [148].

7.1.4 Atom Probe Tomography

The needle-shaped specimen for the atom probe tomography (APT) test was prepared by focused ion beam (FIB) milling (FEI Helios Nanolab SEM/FIB). Before FIB milling, the sample surface was polished following the EBSD specimen preparation procedure, as detailed in the last section. The APT test was conducted on a CAMECA LEAP 5000 XS with a 355 nm wavelength ultraviolet laser. The test was run under an ultra-high vacuum at ~2×10^{-11} torr. The tip base temperature was set to 50 K. The laser pulse energy was 20 pJ, with a pulse frequency of 250 kHz. The detection rate was 2.0–

4.0% of the laser pulse frequency. The run stopped after 60M detection events at 7.4 kV applied voltage.

7.1.5 Electron Microscopy

Scanning electron microscopy (SEM) and electron backscatter diffraction (EBSD) were performed on a Zeiss LEO-1530 field emission scanning electron microscope. The samples were mechanically polished with 0.05 μm diamond suspension followed by ion milling (Leica EM TIC 3X). For general SEM observation, the ion milling was conducted with 3 kV, 1.5 mA at a milling angle of 30° for 3 minutes. For EBSD purposes, the samples were ion milled with 3 kV, 1.8 mA at a milling angle of 4.5° for 1 hour. The EBSD was performed under a 30 kV accelerating voltage with a step size of 0.2–1 μm.

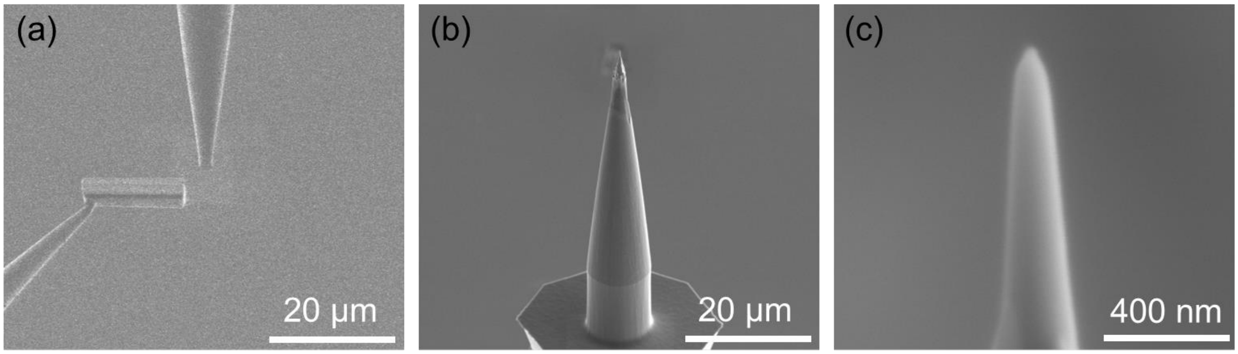

Figure 47. Sample preparation for atom probe tomography. (a) Mounting lift-out sections on microtips. (b) Sharpening lift-out blank. (c) Final APT-read tip.

7.1.6 Materials

The commercial additively-manufactured 17-4 PH stainless steel (C_17-4) specimens for in-situ XRD experiments and tensile testing were fabricated by a laser powder-bed fusion machine with commercial feedstock powder (argon-atomized). The chemical composition was analyzed by inductively coupled plasma (ICP) analysis, except that the C and S were analyzed by combustion method while O and N were quantified by inert gas fusion. The detailed composition is shown in Table 4. Before tests, the C_17-4 samples were in the as-printed state without any post-build heat treatment.

The alloy developed in this work (hereinafter, UW_17-4) for in-situ XRD experiments was cast in an arc melter (model SP-MSM20-8, MTI Corporation, USA) with metal elements pre-weighted by a high-precision balance (model PA224C, OHAUS Corporation, USA) with an accuracy of 0.0001 g. The purity of base elements is 99.98% for Fe, 99.995% for Cr, 99.995% for Ni, 99.995% for Cu, and 99.97% for Nb. The arc melting current was 185 A with a melting duration of 15–25 s until the material was fully melted. The ingot was flipped and re-melted six times to ensure composition uniformity. The cast ingot underwent a condition-A solution heat treatment (heating rate 15 °C/min, holding at 1038 ± 5°C for 45 minutes) in a KSL-1500 Muffle Furnace (MTI Corporation, USA) followed by a water quench. The final phase after quenching was fully martensitic [confirmed by synchrotron XRD and electron backscatter diffraction (EBSD)].

Table 4. Chemical composition (mass %) of 17-4PH stainless steels used in this work.

17-4 PH	**Cr**	**Ni**	**Cu**	**Mn**	**Nb**	**C**	**N**	**O**	**Si**	**S**	**P**	**Fe**
Specification	15.0-17.5	3.0-5.0	3.0-5.0	1.0 max.	0.15-0.45	0.07 max.	-	-	1.0 max.	0.03 max.	0.04 max.	Bal.
C_17-4	16.7 ±0.84	4.3 ±0.43	4.0 ±0.4	0.22 ± 0.02	0.3 ±0.03	0.02 ±0.005	0.027 ±0.007	0.058 ±0.015	0.34 ± 0.03	0.003 ±0.0008	0.011 ±0.003	Bal.
UW_17-4 (Nominal)	15.2	4.8	5.0	-	0.3	-	-	-	-	-	-	Bal.
UW_17-4 (Arc-melt)	15.29 ±0.76	4.78 ±0.48	4.91 ±0.49	<0.001 ±0.0003	0.311 ±0.031	0.002 ±0.0005	0.005 ±0.001	0.019 ±0.005	0.009 ±0.002	0.002 ±0.0005	0.007 ±0.002	Bal.
UW_17-4 (Atomized)	15.53 ±0.78	4.92 ±0.49	4.99 ±0.50	0.012 ± 0.003	0.42 ±0.11	0.001 ±0.0003	0.001 ±0.0003	0.022 ±0.006	<0.001 ±0.0003	0.002 ±0.0005	<0.001 ±0.0003	Bal.
UW_17-4 (As-printed)	15.72 ±0.31	4.84 ±0.24	4.91 ±0.25	0.011 ± 0.002	0.27 ±0.04	0.006 ±0.001	0.001 ±0.0002	0.034 ±0.005	0.01 ±0.002	0.003 ±0.0005	<0.005 ±0.001	Bal.

The as-printed UW_17-4 part was made in a powder bed fusion system under a high-purity argon environment (>99.999%). The feedstock powder was argon-atomized in the Arcast HELGA system (Arcast Inc., USA) using as-cast ingots. The laser power was 520 W with a nominal D4σ beam size of ~170 μm, a wavelength of 1070 nm, and a scan hatch spacing of 80 μm. The chemical compositions of UW_17-4 at different fabrication stages (arc-melt, atomization, LPBF) were characterized by a combination of ICP analysis, combustion method (for C and S), and inert gas fusion method (for O and N). The results are displayed in Table 4.

The wrought 17-4 PH steel was purchased from McMaster-Carr in an annealed state. Condition-A solution heat treatment (1038 ± 5°Cfor 45 min) was performed for the tensile testing specimens.

7.2 In-situ Characterization of Phase Transformation Dynamics in C_17-4

To visualize the phase transformation dynamics in C_17-4 during laser melting, the integrated XRD patterns were organized as a function of time to form an XRD intensity map, as shown in Figure 48(b). The time axis is magnified between 0–1 s to highlight the structural transformation details during laser melting. The evolution of XRD intensities includes three stages, as illustrated by the schematics in Figure 48(b): (1) a heating stage when the moving laser was approaching the X-ray-illuminated area; (2) a melting stage where all the diffraction signals disappeared because X-ray intersected with the melt pool and the molten alloy was in an amorphous state; and (3) a cooling stage when the melt pool moved away from the X-ray and the material started to solidify and cool down.

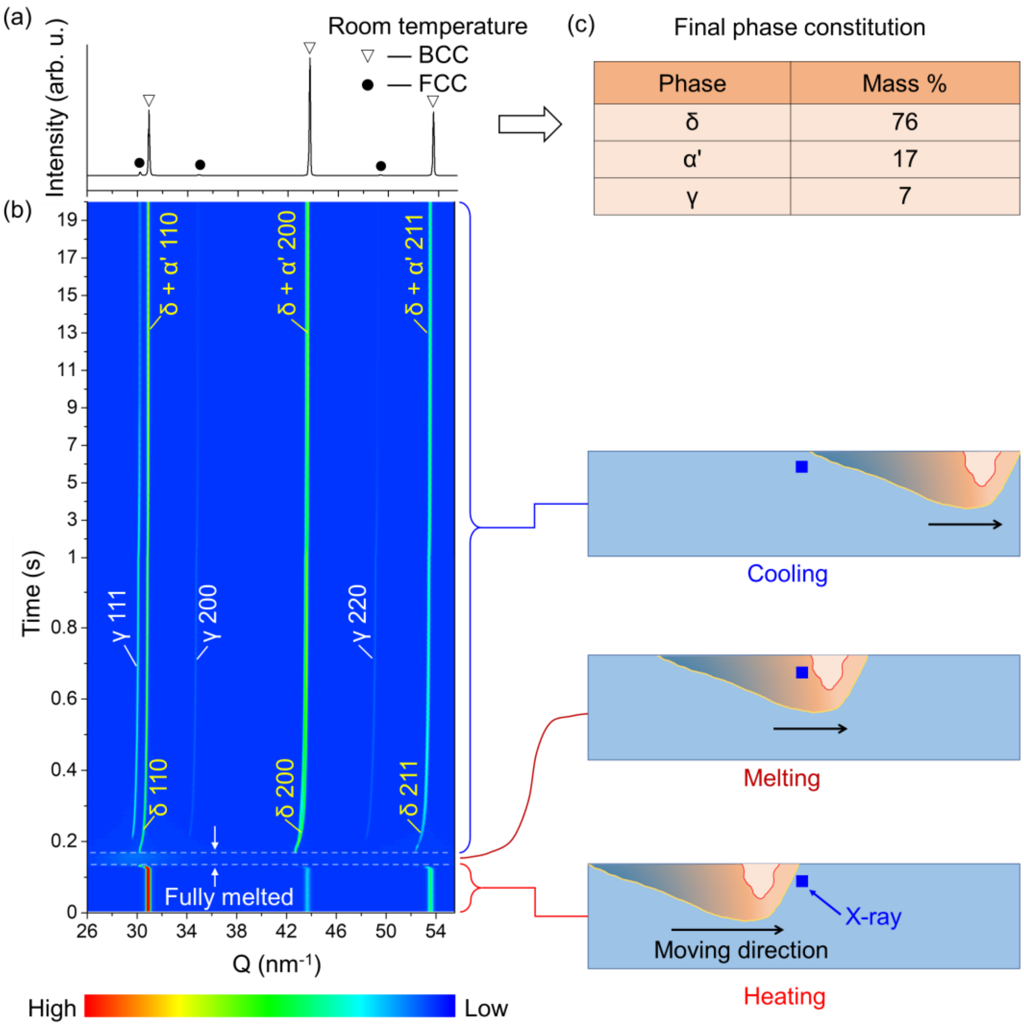

Figure 48. Phase transformation dynamics of C_17-4 during laser melting. (a) Room temperature XRD pattern of as-solidified C_17-4 after laser melting. (b) XRD intensity map (XRD peak intensity evolution as a function of time) during laser melting of C_17-4 from 0 s to 20 s. The time axis is enlarged in the 0–1 s range to highlight the phase transformation details during the initial solidification of laser melting. (c) Final phase constitution of as-solidified C_17-4 after laser melting. The figure is partially adapted from [142].

During initial solidification, Figure 48(b) indicates that the δ-ferrite (δ) phase emerged first from the liquid, followed by the formation of austenite (γ). In conventional manufacturing with a slow cooling rate, a complete phase transformation of δ–γ and then γ–α' was expected, resulting in a final microstructure dominated by martensite (α').

However, during laser melting of C_17-4, neither of these two transformations was completed, as indicated by the continuous δ peaks in the intensity map [Figure 48(b)] and the presence of FCC diffraction peaks in the room-temperature XRD [Figure 48(a)]. As a result, the final microstructure in laser melted C_17-4 is dominated by coarse δ-ferrite grains developed epitaxially along the building direction, as shown by the EBSD characterization in Figure 49. A small amount of mixed martensite and austenite grains were observed along the δ-ferrite grain boundaries.

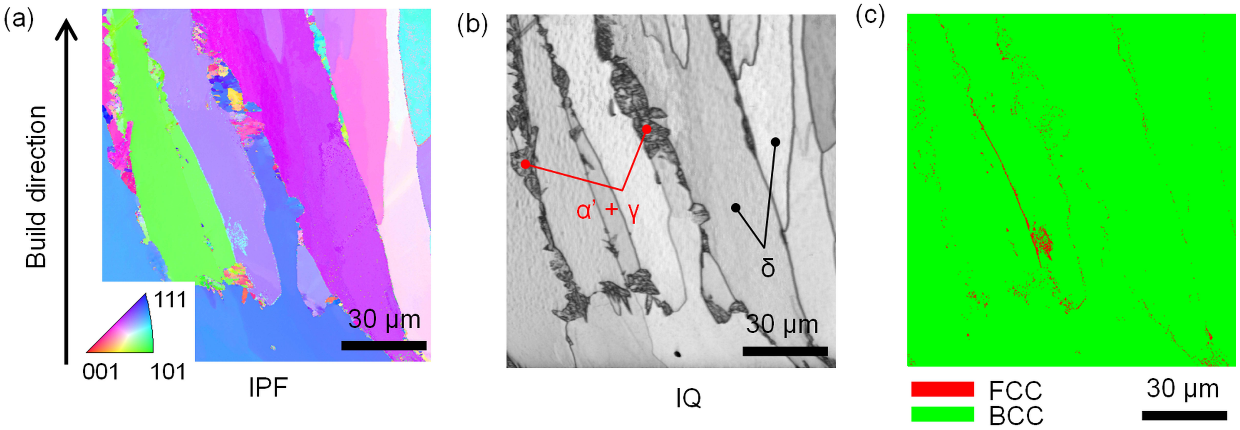

Figure 49. EBSD characterization of as-solidified C_17-4 microstructure after laser melting. (a) Inversed pole figure. (b) Image quality map. Martensite (α') phase and a mixture of austenite (γ) and δ-ferrite (δ) phases were pointed out in the microstructure. (c) Phase map. The figure is adapted from [142].

To further confirm that the initially solidified δ-ferrite can survive into the final structure, the 2D in-situ XRD patterns associated with Figure 48(b) were examined to analyze the development of δ-ferrite during laser melting of C_17-4. The 2D diffraction patterns/rings at representative moments from initial solidification to room temperature are displayed in Figure 50. [Figure 50 and Figure 48(c) share the same time scale.] The horizontal and vertical black bands in the figures are no-signal zones due to the configuration of the X-ray detector.

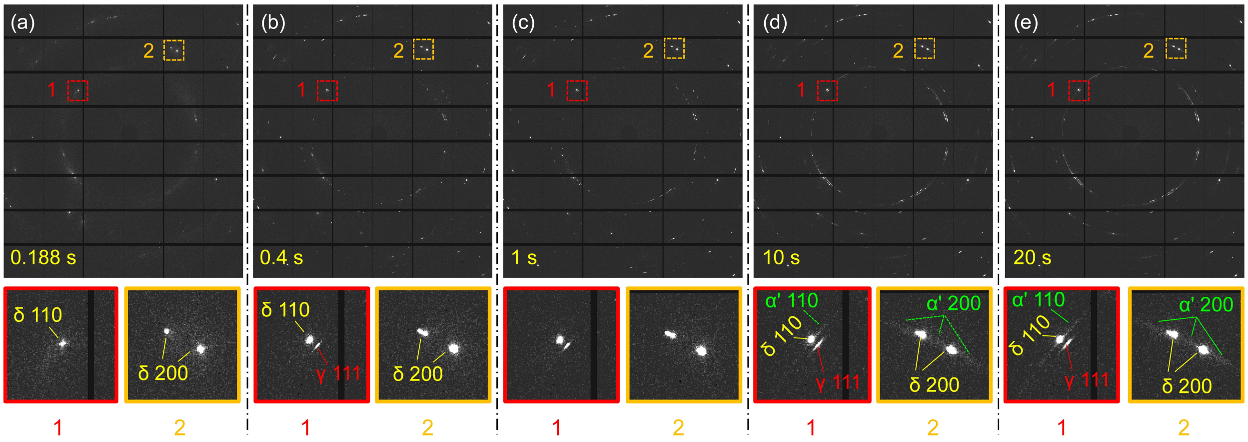

Figure 50. Evidence of initially solidified δ-ferrite retaining in the as-solidified C_17-4 after laser melting. The 2D diffraction patterns at different moments from Figure 48(b) are shown in (a–e), respectively. Figure 50 and Figure 48(b) share the same time scale. Two signature diffraction areas, 1 and 2, were marked using red and orange lines. Areas 1 and 2 at each moment were enlarged and displayed below the whole-field diffraction images. The horizontal and vertical black bands in the figures are no-signal zones due to the configuration of the X-ray detector. Original figure from [142].

At 0.188s, Figure 50(a) shows the diffraction pattern at initial solidification, where only δ-ferrite was just formed from the liquid. Since the δ-ferrite grains are large (as shown in Figure 49) and the number of grains along the X-ray path is small, the diffraction pattern appears scattered. Two signature diffraction areas, 1 and 2, were enlarged to clearly show the diffraction spots from several δ-ferrite grains. During cooling, austenite was formed, as indicated by the γ 111 diffraction pattern in Figure 50(b and c). The formation of austenite did not have a significant influence on the brightness of δ-ferrite diffraction spots. When the temperature went below the martensite start temperature (Ms), martensite started to form, as indicated by the ribbons overlapped with the δ-ferrite diffraction spots in Figure 50(d). Since martensite structure is fine and rather randomly oriented, its 2D diffraction pattern appears to be a ring/ribbon rather than scattered spots. When the material cooled down to room temperature [Figure 50(e)], the diffraction pattern exhibited a mixture of three phases: martensite (as indicated by the α' 110 and 200 diffraction ribbons), austenite (as indicated by the γ 111 diffraction ribbon), and δ-ferrite (as indicated by the δ 110 and 200 diffraction spots retained from the initial solidification). Please refer to Appendix B, Figure A5, for the analysis of more δ-ferrite diffraction spots.

A Rietveld refinement analysis was adopted at two stages during cooling to estimate the final phase constitution of C_17-4 after laser melting. Firstly, the FCC and BCC phase fractions at 0.6 s from Figure 48(b) were determined. At this moment, both δ-ferrite and austenite were fully developed (as indicated by the plateau of peak intensity–time curve in Figure 51), yet the austenite-to-martensite transformation has not started (validated from the 2D diffraction pattern). Therefore, the BCC diffraction at this moment solely came from the residual δ-ferrite and will retain to room temperature.

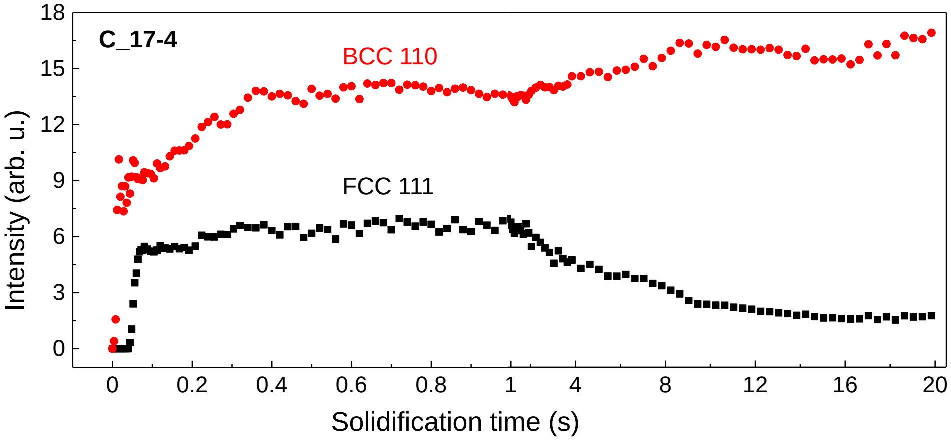

Figure 51. XRD intensity evolution of C_17-4 from Figure 48(b) during solidification. The time axis is enlarged in the 0–1 s range. The uncertainty for BCC intensity measurement is 1%. The uncertainty for FCC intensity measurement is 2%. Original figure from [142].

Next, the FCC and BCC phase fractions at room temperature were determined. The additional fraction of the BCC phase at room temperature compared to the BCC fraction at 0.6 s was attributed to the martensite formed from γ–α' transformation. It should be noted that the phase fraction analysis from Rietveld refinement was based on the assumption of powder diffraction. The discrete diffraction spots of δ-ferrite added to the uncertainty of the phase fraction estimation. Therefore, the analysis here is rather qualitative than quantitative. Hence, the final phase constitution in laser-melted C_17-4 was estimated to contain 76 mass % residual δ-ferrite, 7 mass % residual austenite, and only 17 mass % desired martensite.

For the first time, the existence of a substantial amount of δ-ferrite in the as-printed 17-4 PH steel is directly and unambiguously demonstrated. Due to the low carbon content in the 17-4 stainless steel, the tetragonal distortion of the BCC structure induced by martensite transformation cannot be detected by XRD, resulting in difficulty distinguishing δ-ferrite and martensite in the as-printed part. The direct observation of the phase evolution from 2D diffraction patterns by our in-situ experiment provides a definitive conclusion.

The cooling rate in the laser-melting experiment during the initial solidification was estimated based on the thermal expansion-induced change in lattice parameters. The temperature (T) dependent lattice parameter (a) was measured by an in-situ furnace heating/cooling XRD experiment performed at beamline 11-ID-C of the Advanced Photon Source. Figure 52(a and b) show the constructed a–T relationship of BCC and FCC phases during heating and cooling of C_17-4, respectively. Separately, an intensity-versus-temperature curve [Figure 52(c)] marks the phase transformation events during the thermal process. The temperatures were further calibrated using thermomechanical analysis (TMA) on C_17-4 [Figure 52(d)] by assigning the martensite start temperature (Ms) and BCC–FCC transition temperature measured from the TMA test [Figure 52(d)] to the corresponding events denoted by X-ray intensity evolutions from in-situ testing [Figure 52(c)]. With the calibrated a–T relationship, the cooling rate during the initial solidification of C_17-4 in Figure 48(b) was estimated to be 1.7 × 10^4 °C/s by evaluating the lattice parameter change within a certain period (da/dt). To be noted, all the cooling rates in this work refer to the initial solidification cooling rate measured based on the diffraction peak shift in the solid phase within a 50 μm × 30 μm sampling area under a 250 Hz recording frame rate (1 ms exposure for each frame).

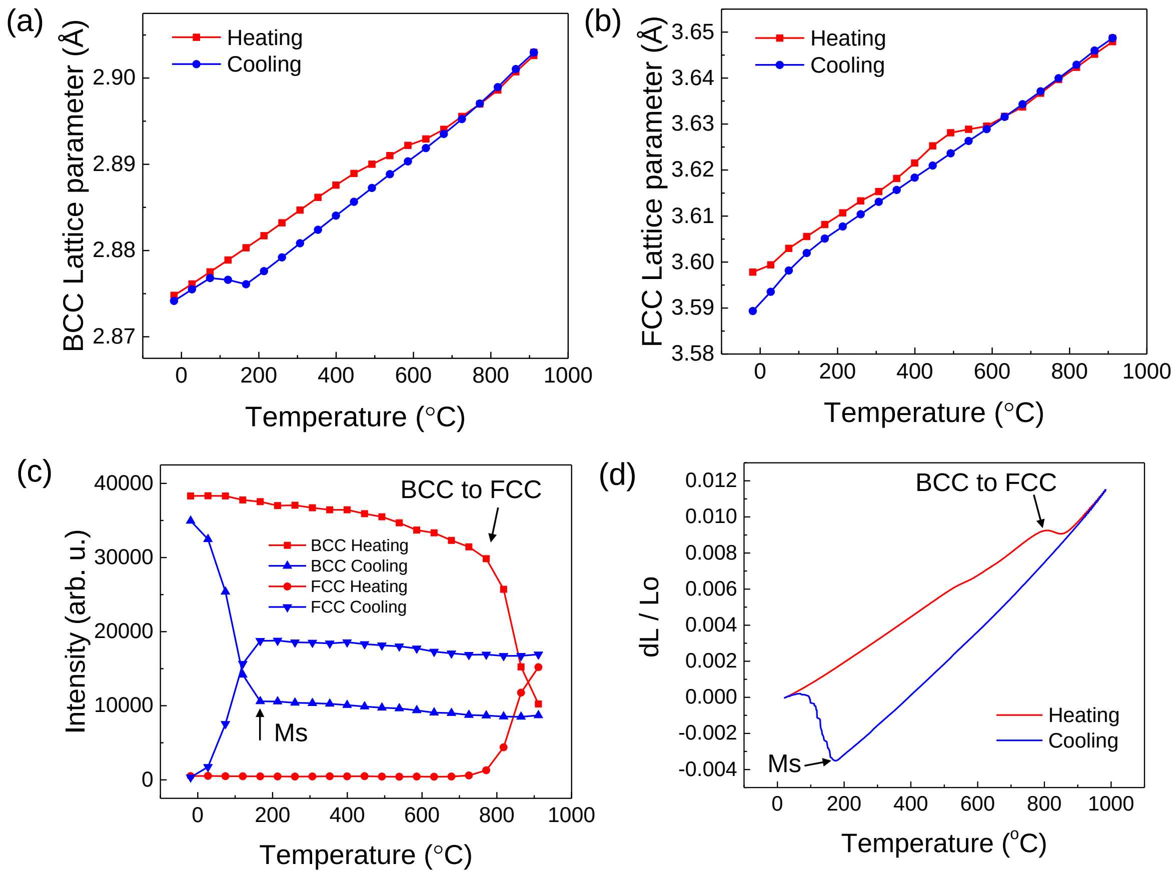

Figure 52. Estimation of cooling rate. (a) BCC lattice parameter change measured by in-situ furnace heating-cooling XRD test. (b) FCC lattice parameter change during in-situ furnace heating-cooling XRD test. (c) BCC and FCC diffraction peak intensity change as a function of temperature during in-situ furnace heating-cooling XRD test. (d) Thermomechanical analysis (TMA) test showing the dilation as a function of

temperature. The material is C_17-4, and the heating/cooling rate was set to 20 ℃/min for all tests. The uncertainty for lattice parameter measurements in (a) and (b) is 0.0002 Å. The uncertainty for intensity measurement in (c) is 0.4%. The uncertainty for thermal expansion measurement in (d) is 2%. Original figure from [142].

7.3 Phase Transformation Dynamics Informed Alloy Development Strategy

Under the cooling rate of 1.7×10^4 °C/s, it is observed that a highly stabilized δ-ferrite sustained to room temperature, as indicated by Figure 50 and the quantified XRD intensity evolution as a function of time in Figure 51. Previous studies reported that high cooling rates of 10^5–10^6 °C/s were required to bypass the δ–γ transformation in 17-4PH stainless steel due to the insufficient time (up to ~6 ms) spent within the δ–γ transformation temperature range (roughly from 600–800°C to 1250–1450°C, depending on specific compositions) [71,82,149–151]. However, the experiment in this work, conducted under a lower cooling rate on the order of 10^4 °C/s, extended the time spent in the δ–γ transformation range by tenfold (on the order of ~60 ms). Yet, the δ–γ transformation still did not occur, suggesting that the initially solidified δ-ferrite was highly stable.

Previous alloy development work focused on tuning the solid-solid phase transformation (δ–γ) to obtain more martensite in the final 17-4 structure [150]. The strategy was to increase the austenite stabilizing temperature range so that the δ–γ transformation could have more time to complete during solidification, which leaves more austenite available to transform into martensite. However, the results in this work suggest that the initially solidified δ-ferrite can be too stable to transform into austenite, even with extended time spent during δ–γ transformation.

In light of such findings, a different alloy development strategy was adopted in this work by targeting the liquid-solid phase transformation (liquid–δ) instead of the solid-solid phase transformation (δ–γ). Specifically, the goal is to minimize the formation of δ-ferrite during initial solidification. By decreasing the initially solidified δ-ferrite, more austenite will form during initial solidification. Next, to facilitate the austenite-to-martensite transformation, several minor alloying elements were removed from the alloy composition, including C, Mn, and Si, as they are known to reduce the Ms temperature and delay the γ–α' transformation [152,153]. As a result, more martensite could be obtained in the final as-solidified 17-4 structure based on the two-step design.

To minimize initially solidified δ-ferrite, the individual effects of three major alloying elements (Cr, Ni, Cu) on the maximum solidified δ-ferrite fraction during equilibrium solidification were investigated using the CALPHAD (Calculation of Phase Diagrams) method, with the assumption that phase evolution under equilibrium condition may provide some guidance to the alloy development for rapid cooling conditions. The calculation included all the major alloying elements (Cr, Ni, Cu) and necessary element (Nb) from the 17-4 specification. When varying the concentration of a specific alloying element, the rest alloying elements were kept constant at the median of the 17-4 specification: Cr-16.3%, Ni-4%, Cu-4%, Nb-0.3%. The calculation results in Figure 53 suggest that, to obtain less δ-ferrite during initial solidification, it is necessary to reduce the Cr concentration while increasing the Ni and Cu concentration in the alloy.

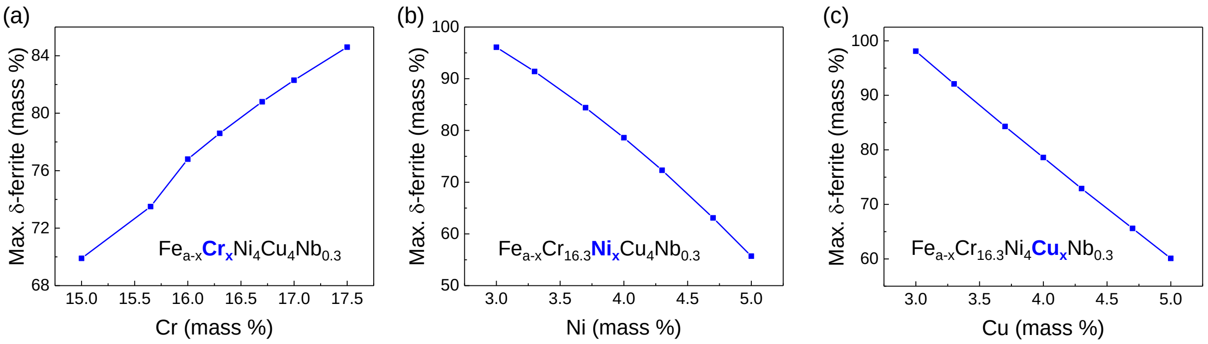

Figure 53. CALPHAD calculation showing the effects of alloying elements (Cr, Ni, Cu) on the maximum δ-ferrite fraction during equilibrium solidification of 17-4PH stainless steel. Original figure from [142].

To check whether the CALPHAD calculation results can provide any indication of the phase transformation trend under rapid cooling conditions, an in-situ laser-melting XRD experiment was performed to examine the real phase transformation dynamics on a developed alloy fabricated with low Cr but high Ni and Cu (within the 17-4PH specification). The nominal alloy composition is $Fe_{74.7}Cr_{15.2}Ni_{4.8}Cu_{5.0}Nb_{0.3}$ (UW_17-4), fabricated by arc melting. During fabrication, the following strategies were taken into consideration:

1. Only major alloying elements (Cr, Ni, Cu) and necessary elements (Nb) were included in the alloy fabrication, while the minor elements (C, Mn, Si, S, P) were excluded for several reasons: (I) C, Mn, and Si can reduce the Ms temperature. They were removed to promote a complete austenite-to-martensite transformation and avoid having residual austenite in the final structure. (II) Minor elements are mostly volatile elements (Mn, Si, S, P) during laser processing, which increases the risk of introducing porosity into the part during laser metal additive manufacturing [61]. (III) The minor elements are allowed to be zero from the 17-4 specification.

The developed alloy with an adjusted composition can still be classified as 17-4 stainless steels without requiring additional certification. (IV) Excluding the minor elements simplifies the alloy fabrication process, as it is difficult to accurately maintain the concentration of minor elements. The uncertain concentration of minor elements also poses challenges for evaluating the effects of major elements on the phase transformation dynamics.

2. Cr and Ni fractions were close to but not exactly at the limit of the specification, to accommodate the concentration fluctuations during fabrication. The total mass fraction of Cr and Ni was set to 20% for the convenience of weighing.
3. The fraction of Cu was set to 5% (maximum allowable concentration in 17-4 specification) for all compositions for two reasons: (I) More Cu can potentially reduce the stability of initially solidified δ-ferrite, as suggested by Figure 53. (II) More Cu can potentially promote Cu precipitate formation during intrinsic heat treatment caused by the layer-by-layer repetitive thermal cycling [88], if the alloy is going to be fabricated via additive manufacturing.

The actual UW_17-4 alloy compositions during each fabrication step were tested by a combination of ICP analysis, combustion method (for C and S), and inert gas fusion method (for O and N). The results are displayed in Table 4.

7.4 Characterization of Phase Transformation Dynamics in UW_17-4

To confirm that UW_17-4 favors the formation of martensite by reducing the amount of initially solidified δ-ferrite (increasing the amount of austenite from initially solidification), the phase transformation dynamics in UW_17-4 during laser processing were examined from both the XRD intensity map (Figure 54(b)) and the 2D diffraction patterns (Figure

55). The XRD intensity map in Figure 54(b) was converted from the same set of 2D patterns as in Figure 55. Figure 54(b) and Figure 55 share the same time scale.

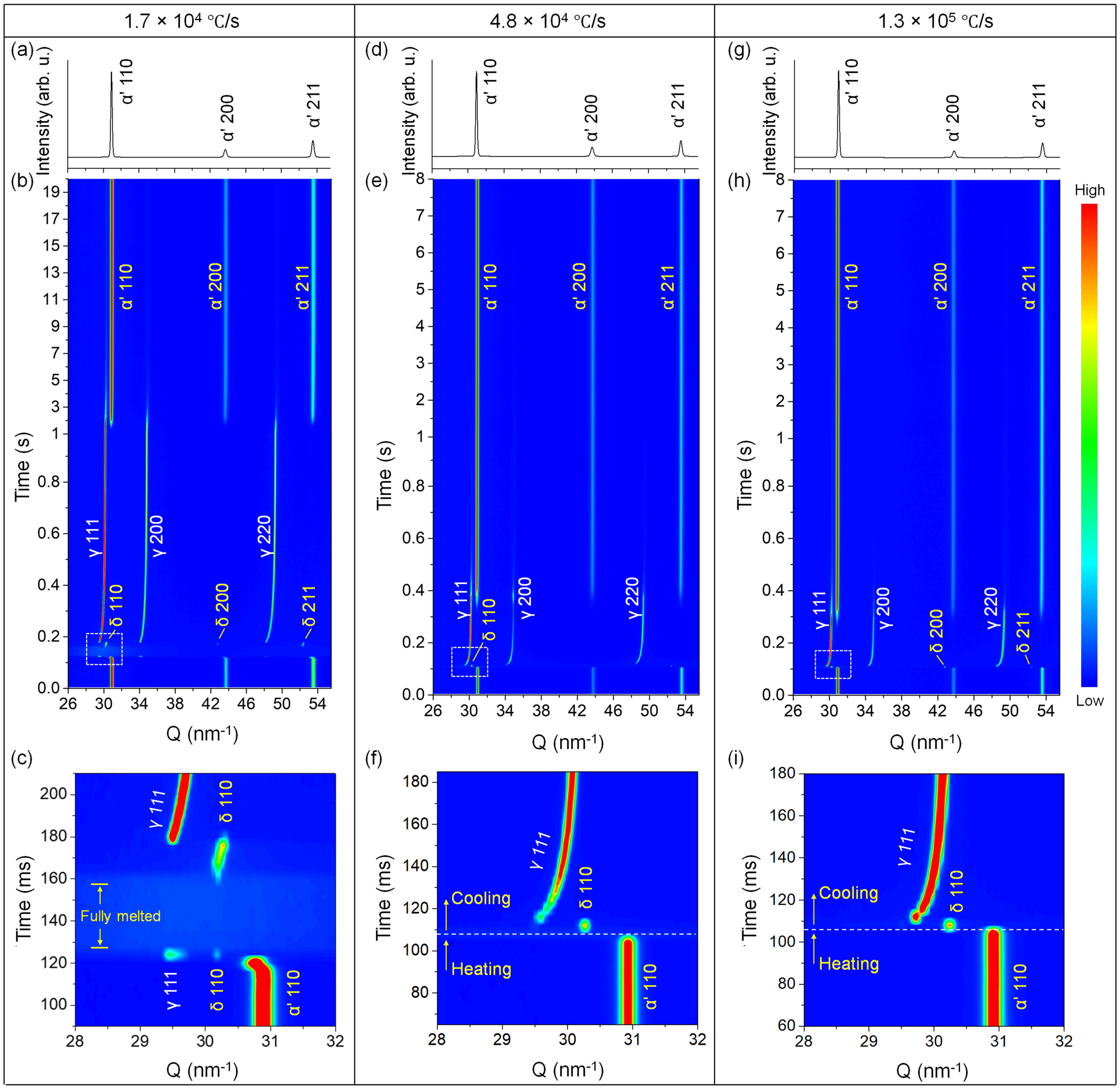

Figure 54. Phase evolution of UW_17-4 under various cooling rates. (a) Room temperature XRD of as-solidified UW_17-4 after laser melting with a cooling rate of 1.7 × 10⁴ °C/s. (b) XRD intensity map during laser melting from 0 s to 20 s with a cooling rate of 1.7 × 10⁴ °C/s. (c) Zoom-in view from (b) highlights the phase transformation during the initial solidification. (d–f) In-situ XRD results under a cooling rate of 4.8 × 10⁴ °C/s. (g–i) XRD results under a cooling rate of 1.3 × 10⁵ °C/s. Original figure from [142].

From the XRD intensity map in Figure 54(a–c), δ-ferrite is still the first phase formed from the liquid under a cooling rate of 1.7 × 10^4 °C/s. Soon, the short-lived δ-ferrite transformed into austenite completely, as indicated in Figure 54(c). In contrast to C_17-4, no δ-ferrite peaks sustained into the austenite regime, suggesting reduced stability of the δ-ferrite in UW_17-4 compared with that of C_17-4. Subsequently, the fully austenite structure started transforming into martensite at a lower temperature [$t \approx 1.5$ s, Figure 54(b)]. The austenite-to-martensite transformation is completed before room temperature, leaving a fully martensitic as-solidified structure, as evidenced by the room-temperature XRD pattern in Figure 54(a).

The 2D diffraction patterns in Figure 55 told the same story from another angle. During initial solidification (0.172 s), δ-ferrite first came out from the liquid, as indicated by the bright spots in Figure 55(a). Shortly afterward (0.4 s), austenite was formed and consumed all the δ-ferrite, as indicated by the γ 111, γ 200, and γ 220 diffraction patterns in Figure 55(b) and the absence of δ 110 and δ 211 diffraction spots. Martensite started to form when the temperature dropped below the Ms point, as shown in Figure 55(c). The martensite’s α' 110 and α' 211 diffraction patterns appeared as uniform, continuous rings, like powder diffraction, because martensite structure is fine and rather randomly oriented. During further cooling (10 s), as shown in Figure 55(d), more austenite transformed into martensite, and the austenite diffraction rings almost vanished. When the material cooled down to room temperature [Figure 55(e)], only uniform, continuous martensite diffraction rings were observed, suggesting that the final material structure is fully martensitic.

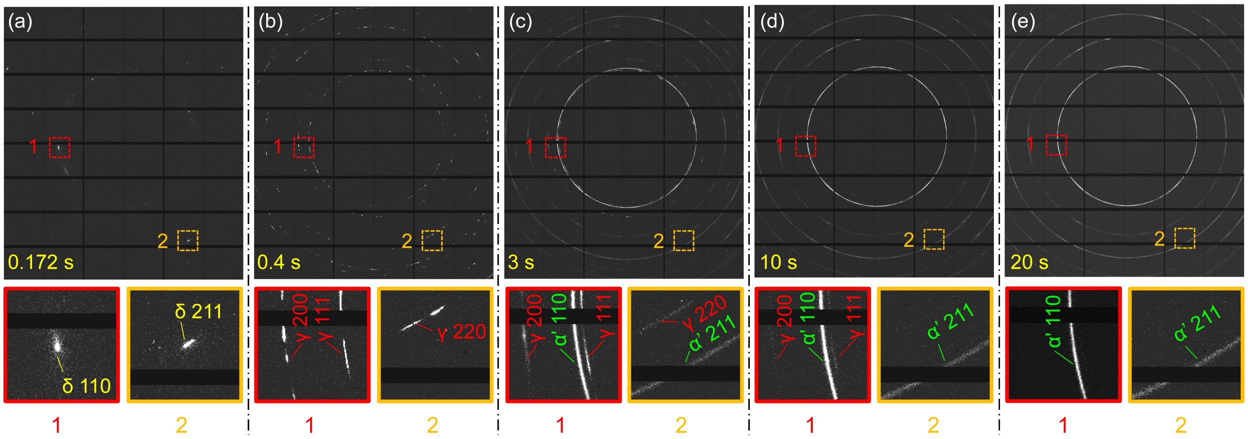

Figure 55. Analysis of phase evolution in UW_17-4 after laser melting. The 2D diffraction patterns at different moments from Figure 54(b) are shown in (a–e), respectively. Figure 55 and Figure 54(b) share the same time scale. Two signature diffraction areas, 1 and 2, were marked using red and orange lines. Areas 1 and 2 at each moment were enlarged and displayed below the whole-field diffraction images. The horizontal and vertical black bands in the figures are no-signal zones due to the configuration of the X-ray detector. Original figure from [142].

7.5 Tolerance of UW_17-4 to Various Processing Conditions

A robust alloy should tolerate various processing conditions to accommodate different manufacturing methods. In this section, experiments were conducted to test the tolerance of UW_17-4 to different cooling rates and environmental impurities.

To examine whether the UW_17-4 can maintain its phase transformation behavior across various cooling conditions, in-situ laser-melting XRD experiments under the cooling rates of 4.8×10^4 °C/s and 1.3×10^5 °C/s were performed. Together with the experiment under the cooling rate of 1.7×10^4 °C/s, the complete phase transformation history under each condition was presented in Figure 54(b, e, and h), with the initial solidification enlarged in Figure 54(c, f, and i).

Taking Figure 54(a–c) as a reference, it can be observed that the phase transformation behaviors at higher cooling rates followed the same trend as those under

1.7 × 10^4 °C/s. Under all conditions, δ-ferrite first solidified from the liquid, then fully transformed into austenite. The fully austenitic structure of UW_17-4 started to transform into martensite at a Ms temperature of 233 ± 21°C (averaged from the three experiments in Figure 54), resulting in a fully martensitic final structure, as evidenced by the room-temperature XRD patterns in Figure 54(a, d, and g). Therefore, the UW_17-4 can reliably produce a fully martensitic structure under the examined cooling rates.

Since the feasible cooling rate window for in-situ observation is limited, ex-situ laser melting and casting experiments were conducted to further study the as-solidified microstructure in UW_17-4 with an extended range of cooling rates by electron backscatter diffraction (EBSD), as shown in Figure 56. On the orders of 10^2 °C/s, 10^4 °C/s, and 10^7 °C/s, three cooling rates were accomplished by casting (arc-melting), single-layer laser melting, and laser spot welding, respectively. To be noticed, the cooling rate of 2 × 10^4 °C/s in the single-layer laser melting sample [Figure 56(b)] is within the cooling rate window of the in-situ experiment (Figure 54). Hence, it serves as an orthogonal reference point for the ex-situ data. In addition, the substrate in Figure 56(b) is a piece of UW_17-4 after condition-A solution heat treatment. During condition-A heat treatment, the material was heated up to 1038°C (above its austenite temperature), held for 45 minutes, and followed by quenching. All potential δ-ferrite will transform into austenite during the long time holding at high temperature. During quenching, all austenite will transform into martensite. Hence, the substrate microstructure in Figure 56(b) is fully martensitic and also serves as a reference point for other ex-situ experiments.

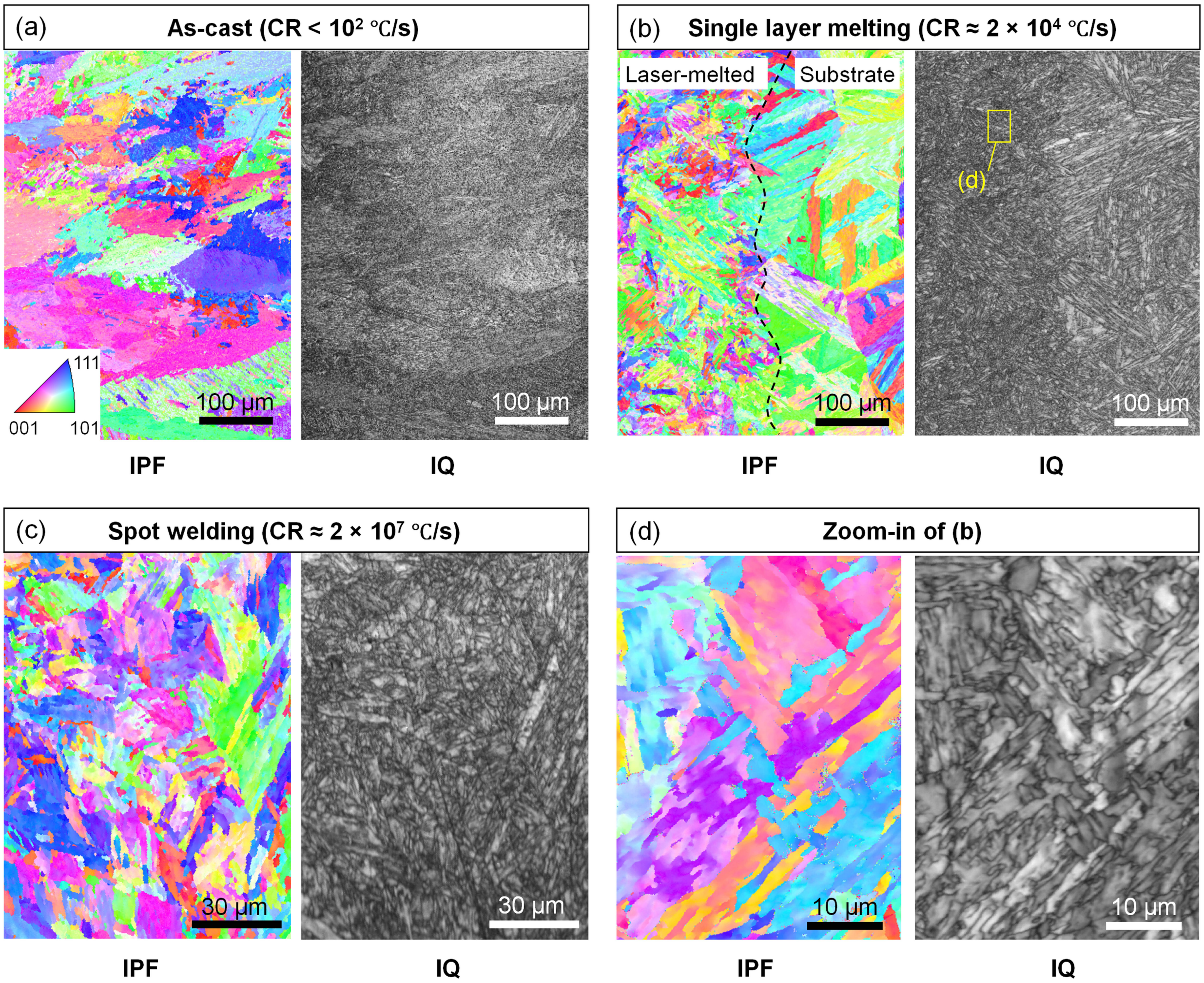

Figure 56. EBSD characterization of as-solidified UW_17-4 under various cooling rates. (a) EBSD of as-cast UW_17-4 fabricated by arc-melting. The left panel is an inversed pole figure (IPF). The right panel is an image quality (IQ) map. (b) EBSD of UW_17-4 after a single-layer laser melting (transverse cross-section). The substrate is a cast, fully martensitic UW_17-4 after a solution heat treatment. (c) EBSD of UW_17-4 after laser spot welding under 156 W for 1 ms laser duration (transverse cross-section). (d) EBSD of a zoom-in area from (b). The microstructures for all conditions are fully martensitic. All IPFs share the same color code, shown in the inset of (a). Original figure from [142].

EBSD data in Figure 56 confirms that the microstructure under the three cooling rates (10^2 °C/s, 10^4 °C/s, 10^7 °C/s) were all fully martensitic, as indicated by the image quality (IQ) maps of Figure 56(a–c). The consistent dark netlike features in the IQ maps are signatures of martensite resulting from its poor diffraction quality caused by internal high-density lattice defects (such as dislocations and sub-grain boundaries) [150,154–156]. These features are distinct from the δ-ferrite IQ map in Figure 49(b), where the δ-ferrite grains appear much brighter due to fewer lattice defects. The IQ map of Figure 56(b) shows a slight difference in the imaging contrast, where the left half field-of-view is darker than the right half. This observation is due to a refined structure obtained under a high cooling rate, as exhibited in the inversed pole figure (IPF) of Figure 56(b). The details of the refined structure were zoomed in and displayed in Figure 56(d).

Therefore, with both in-situ and postmortem examination, the developed alloy, UW_17-4, is demonstrated to consistently form a fully martensitic final structure under a broad range of cooling rates (10^2–10^7 °C/s). The range encompasses all major types of fusion-based additive manufacturing technologies.

In addition to good tolerance to cooling rates, a robust material for AM must have good resistance to environmental impurities. Environmental impurities in AM refer to elements not within the alloy specifications. It is almost inevitable to entrain environmental impurities to the alloy during AM processing. For example, the directed energy deposition (DED) AM processes, especially the wire-based DED process [157], sometimes are performed in an open environment, with flowing inert gas blowing toward the laser-matter interaction area. The inert gas could easily mix with the environment air during the process.

Therefore, the following experiments were designed to demonstrate that UW_17-4 can consistently produce a fully martensitic structure with impurity in the processing environment. To simulate the impurities in the environment, 20 vol.% air was mixed with 80 vol.% shielding argon gas inside the test chamber. Under this mixed-gas environment, a UW_17-4 specimen was remelted at the exact same location up to three times, with the phase transformation dynamics monitored using in-situ XRD. The results are shown in Figure 57.

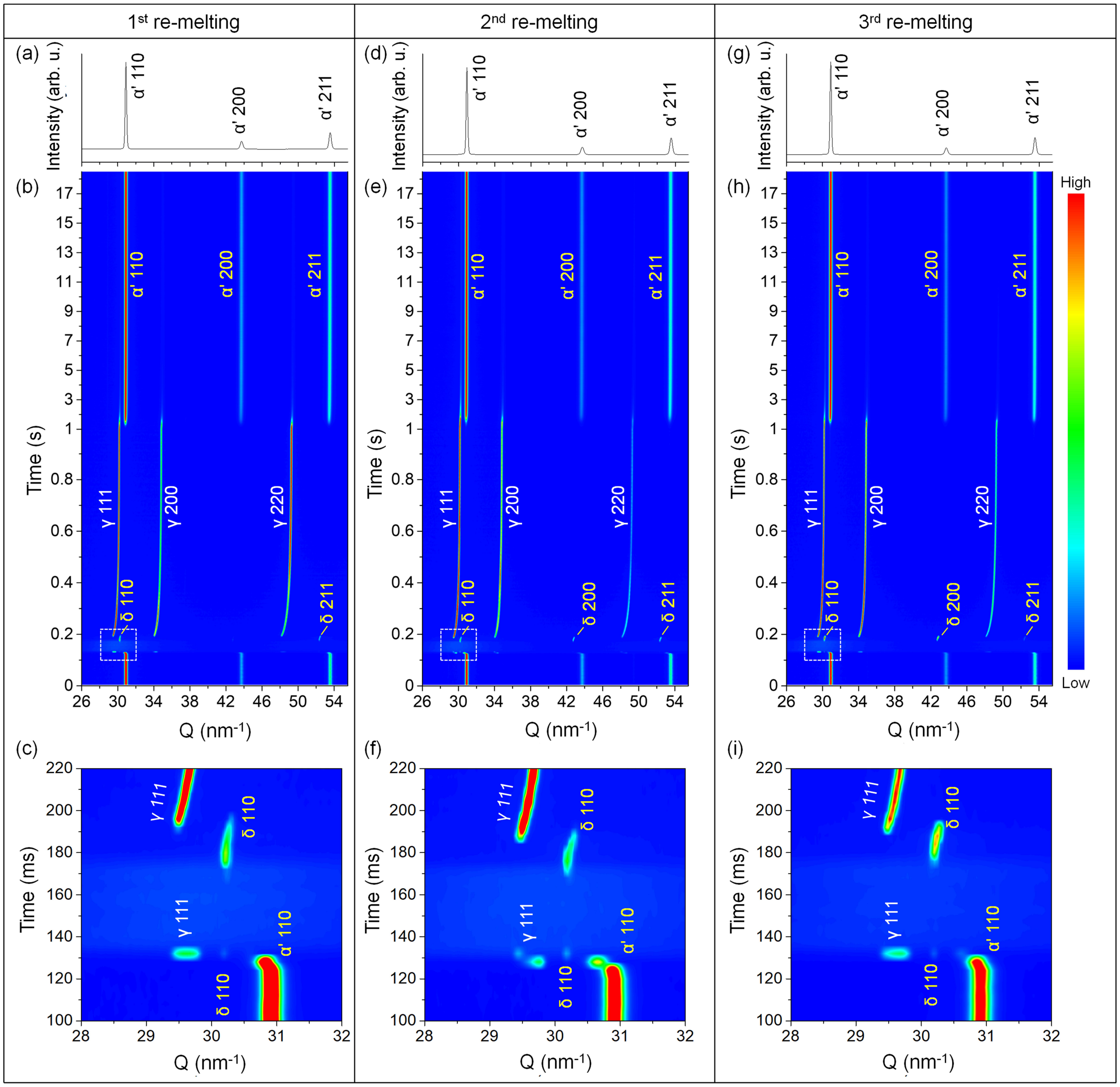

Figure 57. Phase transformation dynamics of UW_17-4 with impurity in the environment gas. (a) Room temperature XRD of as-solidified UW_17-4 after 1st laser re-melting. (b) XRD intensity map during 1st laser re-melting from 0 s to 18.5 s. (c) Zoom-in view from (b) highlighting phase transformation during the initial solidification. (d–f) XRD results of laser re-melting for the 2nd time at the same location as in (a–c). (g–i) XRD results of

laser re-melting for the 3rd time at the exact location as in (a–c). Original figure from [142].

After the 3rd re-melting, the final phase structure is still fully martensitic, as evidenced by the BCC peaks in Figure 57(g) and the complete δ–γ–α' transformation in Figure 57(h and i). In addition, among the three re-melting experiments, no significant differences were observed regarding phase transformation sequence and temperature, indicating a good tolerance of UW_17-4 to typical environment impurities.

7.6 Structure and Property of As-Printed UW_17-4

A 3D-printed UW_17-4 part was fabricated using a laser powder bed fusion system to examine our developed alloy in the actual AM process. The final structure in the as-printed part was a fully BCC structure (> 99.9 mass %), as confirmed by the synchrotron XRD data in Figure 58(a), which contains bulk structural information from a sampling volume of 1.0 mm × 0.6 mm × 0.8 mm. Further EBSD examination revealed fully martensitic features on the IQ map of the as-printed UW_17-4 [Figure 58(b)], similarly to those shown in Figure 56. Given the combined evidence from Figure 58(a and b), the as-printed UW_17-4 part is fully martensitic.

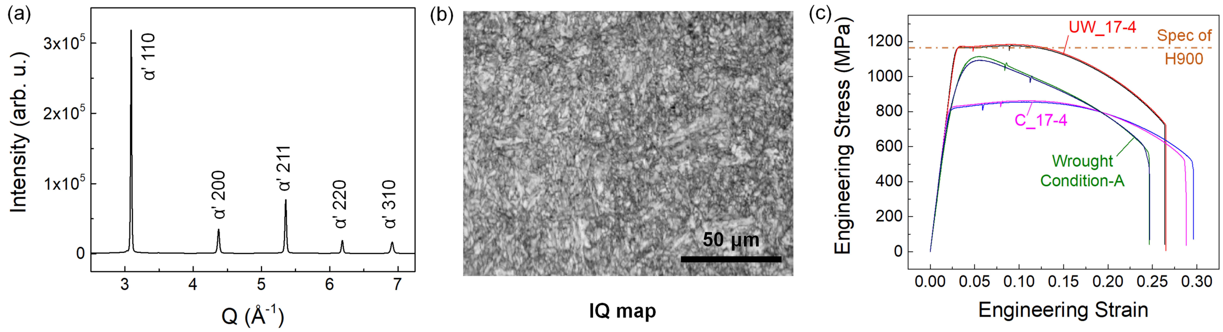

Figure 58. Structure and property of as-printed UW_17-4. (a) HRXRD of as-printed UW_17-4. The XRD sample volume was 1.0 mm × 0.6 mm × 0.8 mm. (b) IQ map of as-printed UW_17-4 by EBSD characterization. (c) Tensile test curves of the as-printed

UW_17-4, as-printed C_17-4, and commercial wrought 17-4 steel after condition-A solution heat treatment (Wrought Condition-A). The orange line is the minimum specification of precipitation-hardened 17-4 PH stainless steel after H900 heat treatment. Original figure from [142]*.*

The mechanical property of the as-printed UW_17-4 was characterized by tensile testing. The engineering stress-strain tensile curves of the as-printed UW_17-4 was compared with its counterparts, as-printed C_17-4 and commercial wrought 17-4 after condition-A solution hear treatment (fully martensitic), with a reference point being the specification of 17-4 PH stainless steel after condition-A + H900 heat treatment (fully martensitic + precipitation hardening). The results exhibited in Figure 58(c) demonstrate that: (1) the as-printed UW_17-4 has a yield strength of 1157 ± 23 MPa, which is over 40% (346 MPa) higher than that of the as-printed C_17-4 (811 ± 16 MPa); (2) the yield strength of the UW_17-4 in the as-printed condition is comparable to that of the 17-4 steel specification (1170 MPa) after a precipitation hardening heat treatment.

The as-printed UW_17-4 possesses high yield strength that cannot be explained by UW_17-4 being fully martensitic alone because otherwise, it would have a similar yield strength to the solution heat-treated wrought 17-4 steel [Figure 58(c)]. A probable reason for the unexpected high yield strength is the existence of copper-rich precipitates, which are a major contributor to the extra strength in precipitation-hardened wrought 17-4 steel [92]. To test this hypothesis, small-angle X-ray scattering (SAXS) measurements were performed on as-printed UW_17-4. The SAXS data contain statistically meaningful information from a bulk specimen of 0.8 mm × 0.8 mm × 0.1 mm. The SAXS results in Figure 59(a) unequivocally revealed a scattering feature with a nominal size of ~4 nm (orange line). This size is characteristic of the copper-rich precipitates in the 17-4 PH steel [158,159]. Atom probe tomography (APT) was further performed from the same as-printed UW_17-4 sample. The APT results in Figure 59(b) validated our hypothesis that a high density of Cu-rich precipitation particles exists in the as-printed UW_17-4. It is likely that these small precipitates formed during the cyclic heating/cooling process in AM, which represents an intrinsic heat treatment. An additional characteristic length on the scale of 50 nm also showed up on the SAXS curve in Figure 59(a), which is a good match with the metallurgical pores in the as-printed material, as exhibited by the SEM image in Figure 59(c) and supported by the statistical analysis of pore size distributions within a representative area [Figure 59(d)].

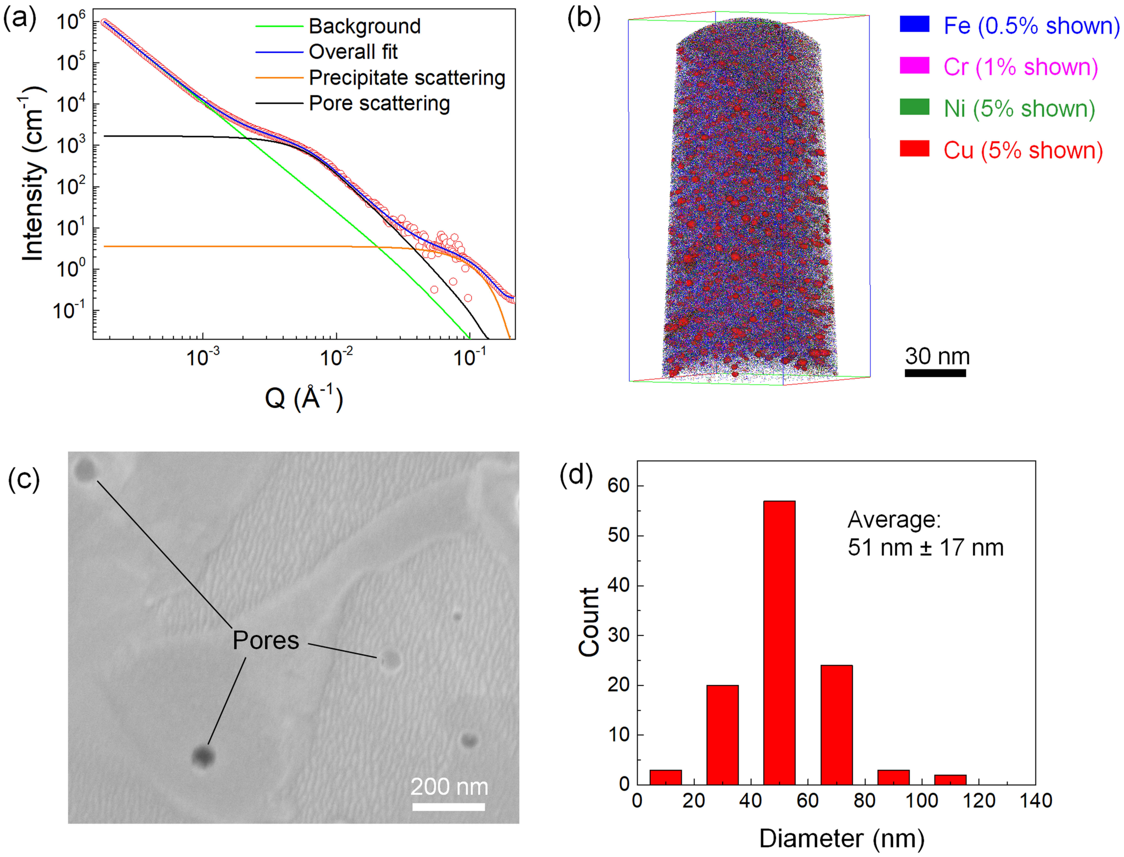

Figure 59. Microstructure analysis on the as-printed UW_17-4. (a) Small-angle X-ray scattering (SAXS) of as-printed UW_17-4. (b) Atom probe tomography (APT) showing the atom map of the as-printed UW_17-4. The Cu-rich precipitates have an average size of ~4 nm. (c) SEM image showing the metallurgical pores in the as-printed UW_17-

4. (d) Statistics of the metallurgical pore size distributed within a 21.79 µm × 14.55 µm area. Original figure from [142]*.*

7.7 Summary and Conclusions

Informed by phase transformation dynamics, a robust martensitic 17-4 stainless steel (UW_17-4) for additive manufacturing was developed in this chapter. The alloy development strategy reported here signifies the importance of understanding phase transformation dynamics under AM conditions. Probed by in-situ high-speed high-energy high-resolution X-ray diffraction, the phase transformation dynamics of 17-4 PH stainless steel during rapid solidification guided the alloy development to target the initial liquid-solid phase transformation during solidification. The alloy development strategy mitigated the formation of the initial δ-ferrite phase and promoted the austenite-to-martensite transformation to achieve the desired fully martensitic phase in the final structure of the UW_17-4. The developed alloy was demonstrated to maintain a fully martensitic structure in the as-solidified state under a wide range of cooling rates (10^2–10^7 °C/s) and withstand common environment impurities. The tolerance of the material to the complex thermal and chemical environments is critical for industrial adoption to achieve reliable and consistent additively manufactured parts, regardless of the differences among AM machines, printing batches, and printing regions.

Chapter 8: Conclusions of Work

Additive manufacturing (AM) has the potential to revolutionize the manufacturing industry by enabling customized production of geometrically and compositionally complex parts with unprecedented functionality and performance [160,161]. However, the complex physical dynamics (spattering, melt pool variation, melt flow evolution, phase transformation, etc.) emerging during the laser powder-bed fusion (LPBF) AM process are challenging to be interpreted and characterized experimentally, because these physics usually occur within a localized region (10s of micrometer to sub-millimeter scale) with highly dynamic behavior (up to meters-per-second movement), and mostly take place inside the metals that cannot be directly observed. In this dissertation, in-situ high-energy synchrotron X-ray imaging & diffraction are utilized as the core process-monitoring techniques to overcome the abovementioned challenges by providing high temporal resolution (up to 1 MHz in imaging, 250 Hz in diffraction), high spatial resolution (down to 1 μm pixel size in imaging), and visibility through metals and alloys at the same time. The transient dynamics above the melt pool (spattering in Chapter 3), inside the melt pool (melt pool variation in Chapter 4, melt flow evolution in Chapters 5 and 6), and beneath the melt pool (phase transformation dynamics in Chapter 7) during LPBF process were revealed and characterized experimentally through in-situ X-ray imaging & diffraction in this dissertation.

In Chapter 3, powder spattering behavior during the LPBF process as a function of time, environment pressure, and the location was characterized and quantified by in-situ X-ray imaging. The complex powder moving trajectories were identified to be driven by the synergistic effects of laser-induced metal vapor jet and the vapor-jet-induced argon gas flow. The metal vapor jet was found to be stronger than the argon gas flow as the spatters within the vapor jet travel with a speed roughly three times as large as the ones traveling within the argon gas flow. The timeline and sequence for establishing the corresponding events in laser-matter interaction were measured to be laser heating & melting (10s μs) – formation of melt pool (10s μs) – formation of intensive vapor jet (100s μs) – formation of argon gas flow (>100s μs). Due to the invisibility of the gaseous phase under X-ray imaging, an experiment was designed to quantify the angular propagation of metallic vapor during laser melting under vacuum by tracing the movement of fine powders pre-placed in the path of the vapor. The results exhibited a trend of vapor speed attenuation during expansion and along the low-angle travel direction. Based on the spattering formation and moving mechanisms revealed in this chapter, several potential ways for mitigating powder spattering were proposed, including (1) pre-sintering the powder bed; (2) using smaller layer thickness; (3) tuning the environment pressure, with the hope that these could guide the future process development for making defect-lean parts.

Chapter 3 characterized the transient dynamics of spatters moving outside the powder bed, while the X-ray signal shows its real strength when the target is within the metals opaque to visible light. Chapter 4 presented the direct observation and quantification of melt pool variations during the LPBF process using in-situ X-ray imaging. By evaluating the size and shape of melt pools under various processing conditions, Chapter 4 attempted to answer a question: whether input energy density (IED) can be used as a metric to assess the combined effects of laser power and laser scanning speed.

The results showed that the same IED with different combinations of laser power and scan speed does not necessarily lead to the same melt pool size or shape. This was attributed to the inconsistency of energy absorption and heat dissipation rates under different laser processing parameters, even though the IED was maintained the same. Further theoretical analysis of energy balance in the melt pool indicates that energy absorption played a significant role in determining the melt pool size and melting mode. It was identified in this chapter that the energy absorption varies for different combinations of laser power and scan speed under a constant IED because laser power and laser scan speed play different roles in the development of the keyhole. Laser power was found to have a greater impact on the depth of the keyhole, while laser scan speed affects more on the width of the keyhole. Therefore, IED is not suitable as a metric to compare different processing parameters when different melting modes are involved because of the substantial differences in the laser absorption among different melting modes. However, within the same melting modes (conduction mode or keyhole mode), IED could still work as a reasonable metric due to the comparable energy absorption rates and energy dissipation rates under the same melting mode.

In Chapter 5 and Chapter 6, a novel melt flow tracing approach was developed and adopted for the in-situ study of liquid flow behavior within the laser-induced melt pool during the LPBF process. Uniformly dispersed populous micro-tracers were used to “visualize” the melt flow movement through in-situ X-ray imaging. Chapter 5 studied the regular melt flow behavior, which is the most probable flow behavior when the melt pool experiences no disturbances from either interior or exterior environments. Chapter 6 aimed to reveal the stochastic melt flow instabilities intrinsic to the LPBF process. Chapter

5 and Chapter 6 together provide a comprehensive understanding of the melt flow behavior in the LPBF process.

Specifically, in Chapter 5, the melt flow tracing approach was elaborated on in detail and confirmed to be effective for representing the surrounding liquid flow through the evaluation of particle settling velocity, acceleration, and effects on the viscosity change of the liquid. Based on the established flow tracing approach, the detailed full-field melt flow patterns in the conduction-mode melt pool and keyhole-mode melt pool were revealed and quantified. Based on the location and moving behavior of the flow, the driving forces for different flows were analyzed and discussed. With the quantified flow speed, it was further found that heat convection is the dominating heat transfer route around the keyhole region, while heat conduction dominates the rest part of the melt pool. The surface wave was found to be damped out during the travel from the keyhole outlet to the tail of the melt pool due to the increased ratio of surface tension over liquid inertia.

In Chapter 6, three major types of melt flow instabilities were identified as: (1) powder/droplet impact, (2) significant keyhole oscillation, and (3) melting-mode switching. It was demonstrated that these instabilities could roughen the part surface, disturb the energy input (by changing the instant keyhole profile), and disturb the solidification process by altering the local solidification rate. The evolution path from simple melt flow pattern (in conduction-mode melt pool) through transition melt flow pattern (in transition-mode melt pool) to complex melt flow pattern (in keyhole-mode melt pool) was revealed and discussed. In the end, two mechanisms for causing keyhole oscillations were identified: laser blocking and powder incorporation.

The last chapter, Chapter 7, explored the phase transformation dynamics during the rapid solidification process associated with the LPBF process using in-situ high-resolution X-ray diffraction. Taking 17-4PH stainless steel as a model material, Chapter 7 aimed to solve a longstanding problem: how to consistently obtain a full martensite phase in 17-4PH stainless steel? The study first observed that commercial 3D-printed 17-4PH stainless steel tended to form a highly stabilized δ-ferrite phase during initial solidification, which resisted transforming into the austenite phase and the subsequent martensite phase at lower temperatures. Based on the observation, a strategy was formed to reduce the initial-solidified δ-ferrite phase to obtain more austenite (which further transforms into martensite). The strategy was executed by developing an alloy composition, UW_17-4, with the guidance of both CALPHAD calculation and experimental validation. The UW_17-4 was demonstrated to form a fully martensitic structure under a wide cooling rate range (10^2–10^7 °C/s) and exhibit certain tolerance to common environment impurities (oxygen and nitrogen). Characterizations on an as-printed LPBF UW_17-4 part also indicate a fully martensitic structure with a high yield strength of 1157 ± 23 MPa, comparable to its wrought counterpart after precipitation-hardening heat treatment. The high mechanical performance in as-printed UW_17-4 was demonstrated by atom probe tomography to be attributed to the high-density Cu-rich nanoscopic precipitations, possibly formed in situ during the cyclic heating/cooling intrinsic to the LPBF process.

Overall, it is hoped that the quantified data and the physical mechanisms revealed in this dissertation will help develop new process technologies with better process stability, fewer defects, and better performance. The data can be used to fit uncertain constants or validate computational models. The phase transformation dynamics informed alloy development strategy in Chapter 7 has the potential to be extended to other alloy systems for developing reliable, high-performance alloys specific for additive manufacturing.

Chapter 9: Recommendations for Future Work

Although this dissertation provides a comprehensive study of the physical dynamics from multiple levels of the LPBF process, there remain various opportunities for future work.

In Chapter 3, studying spattering behavior was conducted with a static environment argon gas for variable control in the experiments. However, commercial LPBF machines usually apply flowing argon gas across the powder bed to blow away the metal vapor and a fraction of the spatters. It would be important to study the interaction between the flowing shielding gas and the spatter particles for a better process design to control the spatters. At the end of Chapter 3, three potential mechanisms were proposed for the mitigation of spattering: (1) pre-sintering the powder bed; (2) using smaller layer thickness; (3) tuning the environment pressure. Although the mechanism (2) has been demonstrated in the publication [43] associated with Chapter 3, mechanisms (1) and (3) remained unvalidated by the time of publication. Later, several works were published with the experiments related to the mechanisms of (1) and (3), such as the evaluation of low chamber pressure on the LPBF printing quality [162] and the study of laser pre-sintering on the denudation behavior [163] in LPBF. Nevertheless, research on these topics is still limited, and there is plenty of room for exploration.

Chapter 4 suggested that input energy density (IED) was not suitable as a metric to describe the process conditions, especially when different sets of parameters lead to different melting modes. Therefore, new metrics must be developed for the convenience of process design with better accuracy. Since laser absorption is a major variant among different processing conditions, it is suggested the new metrics should include the laser absorption term in the formula.

The melt flow tracing approach used in Chapters 5 and 6 opened the door for experimental characterization of melt flows under various processing conditions and material properties. For example, the melt flow behavior could be studied in the processes of pulsed-laser melting, with/without pre-heating, or under an electric/magnetic field. The melt flow behavior could also differ in different material systems, such as nanocomposites with high viscosity [164], immiscible alloys, or alloys with surface active agents. To better understand the melt flow dynamics, it is also necessary to perform computational works using experimental measurements as inputs to identify and quantify the exact driving forces of the melt flow. Such knowledge is critical for process development, such as removing pores by thermocapillary force [39].

Another topic worth investigating is the relationship between the melt flow variation and the microstructure. As demonstrated in Chapter 6, the melt flow instabilities will lead to the local solidification rate variation, resulting in microstructure variation. Depending on the specific applications, such microstructural variation could be either beneficial or detrimental to the material. Investigating such microstructural variation as a function of local melt flow behavior would provide important information for better control of the process.

The phase transformation dynamics informed alloy development work reported in Chapter 7 could inspire future work in two ways. First, the alloy development strategy can potentially be applied to other alloy systems with multi-stage phase transformations (such as titanium alloy) to control the as-printed phase constitutions. Second, the developed alloy UW_17-4 is a proof-of-concept. Pure elements were used to fabricate UW_17-4 with low levels of impurities. It remains unclear what level of impurity elements such as carbon, sulfur, and phosphorus UW_17-4 can tolerate without changing its phase transformation behavior. It also remains unclear the energy barrier for forming the Cu-rich precipitations in the as-printed UW_17-4. The proper processing conditions to promote the in-situ precipitation-hardening still need future investigations. In the end, although as-printed UW_17-4 processes a yield strength comparable to H900 17-4PH, it is still worth studying the influence of various post-heat-treatment on the mechanical performance change of the as-printed UW_17-4 to establish a reliable fabrication procedure for producing high-quality, high-performance parts.

References

[1] D. Loterie, P. Delrot, C. Moser, High-resolution tomographic volumetric additive manufacturing, Nat. Commun. 11 (2020) 852.

[2] J.J. Schwartz, A.J. Boydston, Multimaterial actinic spatial control 3D and 4D printing, Nat. Commun. 10 (2019) 791.

[3] L. Thijs, F. Verhaeghe, T. Craeghs, J. Van Humbeeck, J.-P. Kruth, A study of the microstructural evolution during selective laser melting of Ti–6Al–4V, Acta Mater. 58 (2010) 3303–3312.

[4] J.H. Martin, B.D. Yahata, J.M. Hundley, J.A. Mayer, T.A. Schaedler, T.M. Pollock, 3D printing of high-strength aluminium alloys, Nature. 549 (2017) 365–369.

[5] Y.M. Wang, T. Voisin, J.T. McKeown, J. Ye, N.P. Calta, Z. Li, Z. Zeng, Y. Zhang, W. Chen, T.T. Roehling, R.T. Ott, M.K. Santala, P.J.J. Depond, M.J. Matthews, A. V. Hamza, T. Zhu, Additively manufactured hierarchical stainless steels with high strength and ductility, Nat. Mater. 17 (2018) 63–71.

[6] Q. Jia, D. Gu, Selective laser melting additive manufacturing of Inconel 718 superalloy parts: Densification, microstructure and properties, J. Alloys Compd. 585 (2014) 713–721.

[7] Z. Wang, T.A. Palmer, A.M. Beese, Effect of processing parameters on microstructure and tensile properties of austenitic stainless steel 304L made by directed energy deposition additive manufacturing, Acta Mater. 110 (2016) 226–235.

[8] Y. Liu, Y. Yang, S. Mai, D. Wang, C. Song, Investigation into spatter behavior during selective laser melting of AISI 316L stainless steel powder, Mater. Des. 87 (2015) 797–806.

[9] P. Bidare, R.R.J. Maier, R.J. Beck, J.D. Shephard, A.J. Moore, An open-architecture metal powder bed fusion system for in-situ process measurements, Addit. Manuf. 16 (2017) 177–185.

[10] F. Hugger, K. Hofmann, S. Kohl, M. Dobler, M. Schmidt, Spatter formation in laser beam welding using laser beam oscillation, Weld. World. 59 (2015) 165–172.

[11] G. Repossini, V. Laguzza, M. Grasso, B.M. Colosimo, On the use of spatter signature for in-situ monitoring of Laser Powder Bed Fusion, Addit. Manuf. 16 (2017) 35–48.

[12] H. Krauss, T. Zeugner, M.F. Zaeh, Layerwise Monitoring of the Selective Laser Melting Process by Thermography, Phys. Procedia. 56 (2014) 64–71.

[13] T.G. Spears, S.A. Gold, In-process sensing in selective laser melting (SLM) additive manufacturing, Integr. Mater. Manuf. Innov. 5 (2016) 16–40.

[14] M. Grasso, A.G. Demir, B. Previtali, B.M. Colosimo, In situ monitoring of selective laser melting of zinc powder via infrared imaging of the process plume, Robot. Comput. Integr. Manuf. 49 (2018) 229–239.

[15] H. Shipley, D. McDonnell, M. Culleton, R. Coull, R. Lupoi, G. O'Donnell, D. Trimble, Optimisation of process parameters to address fundamental challenges during selective laser melting of Ti-6Al-4V: A review, Int. J. Mach. Tools Manuf. 128 (2018) 1–20.

[16] L. Hitzler, P. Williams, M. Merkel, W. Hall, A. Öchsner, Correlation between the energy input and the microstructure of additively manufactured cobalt-chromium, Defect Diffus. Forum. 379 (2017) 157–165.

[17] K.G. Prashanth, S. Scudino, T. Maity, J. Das, J. Eckert, Is the energy density a reliable parameter for materials synthesis by selective laser melting?, Mater. Res. Lett. 5 (2017) 1–5.

[18] A.M. Rubenchik, W.E. King, S.S. Wu, Scaling laws for the additive manufacturing, J. Mater. Process. Technol. 257 (2018) 234–243.

[19] O. Andreau, I. Koutiri, P. Peyre, J.-D. Penot, N. Saintier, E. Pessard, T. De Terris, C. Dupuy, T. Baudin, Texture control of 316L parts by modulation of the melt pool

morphology in selective laser melting, J. Mater. Process. Technol. 264 (2018) 21–31.

[20] L.E. Criales, Y.M. Arısoy, B. Lane, S. Moylan, A. Donmez, T. Özel, Laser powder bed fusion of nickel alloy 625: Experimental investigations of effects of process parameters on melt pool size and shape with spatter analysis, Int. J. Mach. Tools Manuf. 121 (2017) 22–36.

[21] T.T. Roehling, S.S.Q. Wu, S.A. Khairallah, J.D. Roehling, S. Stefan Soezeri, M.F. Crumb, M.J. Matthews, Modulating laser intensity profile ellipticity for microstructural control during metal additive manufacturing, Acta Mater. 128 (2017) 197–206.

[22] J.C. Ramme, T.T. Roehling, J.D. Roehling, J.C. McKeown, M.J. Matthews, Laser Intensity Profile Effects on the Solidification Microstructure of Ti-6Al-4V and Ti-5553, Lawrence Livermore National Lab.(LLNL), Livermore, CA., 2018.

[23] Y. Kawahito, N. Matsumoto, Y. Abe, S. Katayama, Relationship of laser absorption to keyhole behavior in high power fiber laser welding of stainless steel and aluminum alloy, J. Mater. Process. Technol. 211 (2011) 1563–1568.

[24] R.R. UNOCIC, J.N. DuPONT, Process efficiency measurements in the laser engineered net shaping process, Metall. Mater. Trans. B. 35 (2004) 143–152.

[25] S.K. Rauniyar, K. Chou, Melt pool analysis and mesoscale simulation of laser powder bed fusion process (L-PBF) with Ti-6Al-4V powder particles, JOM. 71 (2019) 938–945.

[26] P. Yuan, D. Gu, Molten pool behaviour and its physical mechanism during selective laser melting of TiC/AlSi10Mg nanocomposites: simulation and experiments, J. Phys. D. Appl. Phys. 48 (2015) 035303.

[27] Z. Gan, G. Yu, X. He, S. Li, Surface-active element transport and its effect on liquid metal flow in laser-assisted additive manufacturing, Int. Commun. Heat Mass Transf. 86 (2017) 206–214.

[28] S.A. Khairallah, A.T. Anderson, A. Rubenchik, W.E. King, Laser powder-bed fusion additive manufacturing: Physics of complex melt flow and formation mechanisms of pores, spatter, and denudation zones, Acta Mater. 108 (2016) 36–45.

[29] M. Sohail, S.-W. Han, S.-J. Na, A. Gumenyuk, M. Rethmeier, Characteristics of weld pool behavior in laser welding with various power inputs, Weld. World. 58 (2014) 269–277.

[30] P. Jin, Z. Wenjie, W. Xingxing, G. Guoquan, Z. Furong, Numerical simulation of effect of filler wire melting and filling mode on molten pool in laser welding, Infrared Laser Eng. 47 (2018) 306005.

[31] S. Katayama, Y. Kawahito, M. Mizutani, Elucidation of laser welding phenomena and factors affecting weld penetration and welding defects, Phys. Procedia. 5 (2010) 9–17.

[32] Y. Kawahito, K. Nakada, Y. Uemura, M. Mizutani, K. Nishimoto, H. Kawakami, S. Katayama, Relationship between melt flows based on three-dimensional X-ray transmission in situ observation and spatter reduction by angle of incidence and defocussing distance in high-power laser welding of stainless steel, Weld. Int. 32 (2018) 485–496.

[33] A. Matsunawa, J.-D. Kim, N. Seto, M. Mizutani, S. Katayama, Dynamics of keyhole and molten pool in laser welding, J. Laser Appl. 10 (1998) 247–254.

[34] Y. Naito, M. Mizutani, S. Katayama, Effect of oxygen in ambient atmosphere on penetration characteristics in single yttrium–aluminum–garnet laser and hybrid welding, J. Laser Appl. 18 (2006) 21–27.

[35] S. Katayama, Y. Kobayashi, M. Mizutani, A. Matsunawa, Effect of vacuum on penetration and defects in laser welding, J. Laser Appl. 13 (2001) 187–192.

[36] F. Tenner, B. Berg, C. Brock, F. Klämpfl, M. Schmidt, Experimental approach for quantification of fluid dynamics in laser metal welding, J. Laser Appl. 27 (2015) S29003.

[37] Q. Guo, C. Zhao, M. Qu, L. Xiong, L.I. Escano, S.M.H. Hojjatzadeh, N.D. Parab, K. Fezzaa, W. Everhart, T. Sun, L. Chen, In-situ characterization and quantification of melt pool variation under constant input energy density in laser powder bed fusion additive

manufacturing process, Addit. Manuf. 28 (2019) 600–609.
[38] C.L.A. Leung, S. Marussi, R.C. Atwood, M. Towrie, P.J. Withers, P.D. Lee, In situ X-ray imaging of defect and molten pool dynamics in laser additive manufacturing, Nat. Commun. 9 (2018) 1355.
[39] S.M.H. Hojjatzadeh, N.D. Parab, W. Yan, Q. Guo, L. Xiong, C. Zhao, M. Qu, L.I. Escano, X. Xiao, K. Fezzaa, W. Everhart, T. Sun, L. Chen, Pore elimination mechanisms during 3D printing of metals, Nat. Commun. 10 (2019) 3088.
[40] A.A. Martin, N.P. Calta, S.A. Khairallah, J. Wang, P.J. Depond, A.Y. Fong, V. Thampy, G.M. Guss, A.M. Kiss, K.H. Stone, C.J. Tassone, J. Nelson Weker, M.F. Toney, T. van Buuren, M.J. Matthews, Dynamics of pore formation during laser powder bed fusion additive manufacturing, Nat. Commun. 10 (2019) 1987.
[41] J.-B. Forien, N.P. Calta, P.J. DePond, G.M. Guss, T.T. Roehling, M.J. Matthews, Detecting keyhole pore defects and monitoring process signatures during laser powder bed fusion: A correlation between in situ pyrometry and ex situ X-ray radiography, Addit. Manuf. 35 (2020) 101336.
[42] Z.A. Young, Q. Guo, N.D. Parab, C. Zhao, M. Qu, L.I. Escano, K. Fezzaa, W. Everhart, T. Sun, L. Chen, Types of spatter and their features and formation mechanisms in laser powder bed fusion additive manufacturing process, Addit. Manuf. 36 (2020) 101438.
[43] Q. Guo, C. Zhao, L.I. Escano, Z. Young, L. Xiong, K. Fezzaa, W. Everhart, B. Brown, T. Sun, L. Chen, Transient dynamics of powder spattering in laser powder bed fusion additive manufacturing process revealed by in-situ high-speed high-energy x-ray imaging, Acta Mater. 151 (2018) 169–180.
[44] S.A. Khairallah, T. Sun, B.J. Simonds, Onset of periodic oscillations as a precursor of a transition to pore-generating turbulence in laser melting, Addit. Manuf. Lett. 1 (2021) 100002.
[45] C. Zhao, N.D. Parab, X. Li, K. Fezzaa, W. Tan, A.D. Rollett, T. Sun, Critical instability at moving keyhole tip generates porosity in laser melting, Science (80-.). 370 (2020) 1080–1086.
[46] R. Cunningham, C. Zhao, N. Parab, C. Kantzos, J. Pauza, K. Fezzaa, T. Sun, A.D. Rollett, Keyhole threshold and morphology in laser melting revealed by ultrahigh-speed x-ray imaging, Science (80-.). 363 (2019) 849–852.
[47] M. Colopi, A.G. Demir, L. Caprio, B. Previtali, Limits and solutions in processing pure Cu via selective laser melting using a high-power single-mode fiber laser, Int. J. Adv. Manuf. Technol. 104 (2019) 2473–2486.
[48] L. Scime, J. Beuth, Using machine learning to identify in-situ melt pool signatures indicative of flaw formation in a laser powder bed fusion additive manufacturing process, Addit. Manuf. 25 (2019) 151–165.
[49] V. Gunenthiram, P. Peyre, M. Schneider, M. Dal, F. Coste, R. Fabbro, Analysis of laser–melt pool–powder bed interaction during the selective laser melting of a stainless steel, J. Laser Appl. 29 (2017) 022303.
[50] S. Wang, L. Zhu, Y. Dun, Z. Yang, J.Y.H. Fuh, W. Yan, Multi-physics modeling of direct energy deposition process of thin-walled structures: defect analysis, Comput. Mech. 67 (2021) 1229–1242.
[51] W. Ren, Z. Zhang, Y. Lu, G. Wen, J. Mazumder, In-situ monitoring of laser additive manufacturing for Al7075 alloy using emission spectroscopy and plume imaging, IEEE Access. 9 (2021) 61671–61679.
[52] Y. Zhao, Y. Koizumi, K. Aoyagi, D. Wei, K. Yamanaka, A. Chiba, Molten pool behavior and effect of fluid flow on solidification conditions in selective electron beam melting (SEBM) of a biomedical Co-Cr-Mo alloy, Addit. Manuf. 26 (2019) 202–214.
[53] M. Bisht, N. Ray, F. Verbist, S. Coeck, Correlation of selective laser melting-melt pool events with the tensile properties of Ti-6Al-4V ELI processed by laser powder bed fusion,

Addit. Manuf. 22 (2018) 302–306.
[54] K.G. Prashanth, J. Eckert, Formation of metastable cellular microstructures in selective laser melted alloys, J. Alloys Compd. 707 (2017) 27–34.
[55] L. Aucott, H. Dong, W. Mirihanage, R. Atwood, A. Kidess, S. Gao, S. Wen, J. Marsden, S. Feng, M. Tong, T. Connolley, M. Drakopoulos, C.R. Kleijn, I.M. Richardson, D.J. Browne, R.H. Mathiesen, H. V Atkinson, Revealing internal flow behaviour in arc welding and additive manufacturing of metals, Nat. Commun. 9 (2018) 5414.
[56] S.J. Clark, C.L.A. Leung, Y. Chen, L. Sinclair, S. Marussi, P.D. Lee, Capturing Marangoni flow via synchrotron imaging of selective laser melting, IOP Conf. Ser. Mater. Sci. Eng. 861 (2020) 012010.
[57] S.J. Wolff, H. Wang, B. Gould, N. Parab, Z. Wu, C. Zhao, A. Greco, T. Sun, In situ X-ray imaging of pore formation mechanisms and dynamics in laser powder-blown directed energy deposition additive manufacturing, Int. J. Mach. Tools Manuf. 166 (2021) 103743.
[58] A. Bobel, L.G. Hector, I. Chelladurai, A.K. Sachdev, T. Brown, W.A. Poling, R. Kubic, B. Gould, C. Zhao, N. Parab, A. Greco, T. Sun, In situ synchrotron X-ray imaging of 4140 steel laser powder bed fusion, Materialia. 6 (2019) 100306.
[59] Q. Guo, C. Zhao, M. Qu, L. Xiong, S.M.H. Hojjatzadeh, L.I. Escano, N.D. Parab, K. Fezzaa, T. Sun, L. Chen, In-situ full-field mapping of melt flow dynamics in laser metal additive manufacturing, Addit. Manuf. 31 (2020) 100939.
[60] C. Qiu, C. Panwisawas, M. Ward, H.C. Basoalto, J.W. Brooks, M.M. Attallah, On the role of melt flow into the surface structure and porosity development during selective laser melting, Acta Mater. 96 (2015) 72–79.
[61] S.M.H. Hojjatzadeh, N.D. Parab, Q. Guo, M. Qu, L. Xiong, C. Zhao, L.I. Escano, K. Fezzaa, W. Everhart, T. Sun, L. Chen, Direct observation of pore formation mechanisms during LPBF additive manufacturing process and high energy density laser welding, Int. J. Mach. Tools Manuf. 153 (2020) 103555.
[62] M. Xia, D. Gu, G. Yu, D. Dai, H. Chen, Q. Shi, Influence of hatch spacing on heat and mass transfer, thermodynamics and laser processability during additive manufacturing of Inconel 718 alloy, Int. J. Mach. Tools Manuf. 109 (2016) 147–157.
[63] D. Dai, D. Gu, Influence of thermodynamics within molten pool on migration and distribution state of reinforcement during selective laser melting of AlN/AlSi10Mg composites, Int. J. Mach. Tools Manuf. 100 (2016) 14–24.
[64] D. Gu, M. Xia, D. Dai, On the role of powder flow behavior in fluid thermodynamics and laser processability of Ni-based composites by selective laser melting, Int. J. Mach. Tools Manuf. 137 (2019) 67–78.
[65] L. Wang, Y. Zhang, H.Y. Chia, W. Yan, Mechanism of keyhole pore formation in metal additive manufacturing, Npj Comput. Mater. 8 (2022) 22.
[66] S. Ly, A.M. Rubenchik, S.A. Khairallah, G. Guss, M.J. Matthews, Metal vapor micro-jet controls material redistribution in laser powder bed fusion additive manufacturing, Sci. Rep. 7 (2017) 4085.
[67] H. Fayazfar, M. Salarian, A. Rogalsky, D. Sarker, P. Russo, V. Paserin, E. Toyserkani, A critical review of powder-based additive manufacturing of ferrous alloys: Process parameters, microstructure and mechanical properties, Mater. Des. 144 (2018) 98–128.
[68] M. Qian, W. Xu, M. Brandt, H.P. Tang, Additive manufacturing and postprocessing of Ti-6Al-4V for superior mechanical properties, MRS Bull. 41 (2016) 775–784.
[69] W.M. Tucho, P. Cuvillier, A. Sjolyst-Kverneland, V. Hansen, Microstructure and hardness studies of Inconel 718 manufactured by selective laser melting before and after solution heat treatment, Mater. Sci. Eng. A. 689 (2017) 220–232.
[70] K. Amato, Comparison of Microstructures and Properties for a Ni-Base Superalloy (Alloy 625) Fabricated by Electron Beam Melting, J. Mater. Sci. Res. 1 (2012) 3.
[71] M. Alnajjar, F. Christien, C. Bosch, K. Wolski, A.D. Fortes, M. Telling, In-situ neutron

diffraction study of wrought and selective laser melted maraging stainless steels, Mater. Charact. 172 (2021) 110840.

[72] A.J. Shahani, A.J. Clarke, Processing metallic materials far from equilibrium, MRS Bull. 45 (2020) 906–909.

[73] X. Tan, Y. Kok, Y.J. Tan, M. Descoins, D. Mangelinck, S.B. Tor, K.F. Leong, C.K. Chua, Graded microstructure and mechanical properties of additive manufactured Ti–6Al–4V via electron beam melting, Acta Mater. 97 (2015) 1–16.

[74] P. Kürnsteiner, M.B. Wilms, A. Weisheit, B. Gault, E.A. Jägle, D. Raabe, High-strength Damascus steel by additive manufacturing, Nature. 582 (2020) 515–519.

[75] Y. Kok, X.P. Tan, P. Wang, M.L.S. Nai, N.H. Loh, E. Liu, S.B. Tor, Anisotropy and heterogeneity of microstructure and mechanical properties in metal additive manufacturing: A critical review, Mater. Des. 139 (2018) 565–586.

[76] L. Zai, C. Zhang, Y. Wang, W. Guo, D. Wellmann, X. Tong, Y. Tian, Laser Powder Bed Fusion of Precipitation-Hardened Martensitic Stainless Steels: A Review, Metals (Basel). 10 (2020) 255.

[77] C.N.N. Hsiao, C.S.S. Chiou, J.R.R. Yang, Aging reactions in a 17-4 PH stainless steel, Mater. Chem. Phys. 74 (2002) 134–142.

[78] E.A. Lass, F. Zhang, C.E. Campbell, Nitrogen Effects in Additively Manufactured Martensitic Stainless Steels: Conventional Thermal Processing and Comparison with Wrought, Metall. Mater. Trans. A. 51 (2020) 2318–2332.

[79] A.A. Adeyemi, E.T. Akinlabi, R.M. Mahamood, K.O. Sanusi, S. Pityana, M. Tlotleng, Influence of laser power on microstructure of laser metal deposited 17-4 PH stainless steel, IOP Conf. Ser. Mater. Sci. Eng. 225 (2017) 012028.

[80] F. Zhang, M.R. Stoudt, S. Hammadi, C.E. Campbell, E.A. Lass, M.E. Williams, How Austenitic Is a Martensitic Steel Produced by Laser Powder Bed Fusion? A Cautionary Tale, Metals (Basel). 11 (2021) 1924.

[81] M.S. Moyle, N. Haghdadi, X.Z. Liao, S.P. Ringer, S. Primig, On the microstructure and texture evolution in 17-4 PH stainless steel during laser powder bed fusion: Towards textural design, J. Mater. Sci. Technol. 117 (2022) 183–195.

[82] M. Alnajjar, F. Christien, K. Wolski, C. Bosch, Evidence of austenite by-passing in a stainless steel obtained from laser melting additive manufacturing, Addit. Manuf. 25 (2019) 187–195.

[83] L. Facchini, N. Vicente, I. Lonardelli, E. Magalini, P. Robotti, A. Molinari, N. Vicente Jr, I. Lonardelli, E. Magalini, P. Robotti, A. Molinari, Metastable austenite in 17-4 precipitation-hardening stainless steel produced by selective laser melting, Adv. Eng. Mater. 12 (2010) 184–188.

[84] L.E. Murr, E. Martinez, J. Hernandez, S. Collins, K.N. Amato, S.M. Gaytan, P.W. Shindo, Microstructures and properties of 17-4 PH stainless steel fabricated by selective laser melting, J. Mater. Res. Technol. 1 (2012) 167–177.

[85] P. Leo, M. Cabibbo, A. Del Prete, S. Giganto, S. Martínez-Pellitero, J. Barreiro, Laser Defocusing Effect on the Microstructure and Defects of 17-4PH Parts Additively Manufactured by SLM at a Low Energy Input, Metals (Basel). 11 (2021) 588.

[86] T.-H. Hsu, P.-C. Huang, M.-Y. Lee, K.-C. Chang, C.-C. Lee, M.-Y. Li, C.-P. Chen, K.-K. Jen, A.-C. Yeh, Effect of processing parameters on the fractions of martensite in 17-4 PH stainless steel fabricated by selective laser melting, J. Alloys Compd. 859 (2021) 157758.

[87] I. Mathoho, E.T. Akinlabi, N. Arthur, M. Tlotleng, Impact of DED process parameters on the metallurgical characteristics of 17-4 PH SS deposited using DED, CIRP J. Manuf. Sci. Technol. 31 (2020) 450–458.

[88] A. Caballero, J. Ding, S. Ganguly, S. Williams, Wire + Arc Additive Manufacture of 17-4 PH stainless steel: Effect of different processing conditions on microstructure, hardness, and tensile strength, J. Mater. Process. Technol. 268 (2019) 54–62.

[89] F.S.H.B. Freeman, A. Lincoln, J. Sharp, A. Lambourne, I. Todd, Exploiting thermal strain to achieve an in-situ magnetically graded material, Mater. Des. 161 (2019) 14–21.

[90] H.K. Rafi, D. Pal, N. Patil, T.L. Starr, B.E. Stucker, Microstructure and mechanical behavior of 17-4 precipitation hardenable steel processed by selective laser melting, J. Mater. Eng. Perform. 23 (2014) 4421–4428.

[91] X. Wang, G. Wang, T. Shi, Y. Wang, Tensile Mechanical Behavior and Spall Response of a Selective Laser Melted 17-4 PH Stainless Steel, Metall. Mater. Trans. A. 52 (2021) 2369–2388.

[92] A. Yadollahi, N. Shamsaei, S.M. Thompson, A. Elwany, L. Bian, Effects of building orientation and heat treatment on fatigue behavior of selective laser melted 17-4 PH stainless steel, Int. J. Fatigue. 94 (2017) 218–235.

[93] P. Bidare, I. Bitharas, R.M. Ward, M.M. Attallah, A.J. Moore, Fluid and particle dynamics in laser powder bed fusion, Acta Mater. 142 (2018) 107–120.

[94] M.J. Matthews, G. Guss, S.A. Khairallah, A.M. Rubenchik, P.J. Depond, W.E. King, Denudation of metal powder layers in laser powder bed fusion processes, Acta Mater. 114 (2016) 33–42.

[95] M.M. Francois, A. Sun, W.E. King, N.J. Henson, D. Tourret, C.A. Bronkhorst, N.N. Carlson, C.K. Newman, T. Haut, J. Bakosi, J.W. Gibbs, V. Livescu, S.A. Vander Wiel, A.J. Clarke, M.W. Schraad, T. Blacker, H. Lim, T. Rodgers, S. Owen, F. Abdeljawad, J. Madison, A.T. Anderson, J.L. Fattebert, R.M. Ferencz, N.E. Hodge, S.A. Khairallah, O. Walton, Modeling of additive manufacturing processes for metals: Challenges and opportunities, Curr. Opin. Solid State Mater. Sci. 21 (2017) 198–206.

[96] M. Simonelli, C. Tuck, N.T. Aboulkhair, I. Maskery, I. Ashcroft, R.D. Wildman, R. Hague, A Study on the Laser Spatter and the Oxidation Reactions During Selective Laser Melting of 316L Stainless Steel, Al-Si10-Mg, and Ti-6Al-4V, Metall. Mater. Trans. A. 46 (2015) 3842–3851.

[97] M. Grasso, B.M. Colosimo, Process defects and in situ monitoring methods in metal powder bed fusion: a review, Meas. Sci. Technol. 28 (2017) 44005.

[98] W. Everhart, J. Dinardo, C. Barr, The Effect of Scan Length on the Structure and Mechanical Properties of Electron Beam-Melted Ti-6Al-4V, Metall. Mater. Trans. A. 48 (2017) 697–705.

[99] L.E. Murr, S.M. Gaytan, D.A. Ramirez, E. Martinez, J. Hernandez, K.N. Amato, P.W. Shindo, F.R. Medina, R.B. Wicker, Metal Fabrication by Additive Manufacturing Using Laser and Electron Beam Melting Technologies, J. Mater. Sci. Technol. 28 (2012) 1–14.

[100] S.L. Sing, J. An, W.Y. Yeong, F.E. Wiria, Laser and electron-beam powder-bed additive manufacturing of metallic implants: A review on processes, materials and designs, J. Orthop. Res. 34 (2016) 369–385.

[101] W.E. King, H.D. Barth, V.M. Castillo, G.F. Gallegos, J.W. Gibbs, D.E. Hahn, C. Kamath, A.M. Rubenchik, Observation of keyhole-mode laser melting in laser powder-bed fusion additive manufacturing, J. Mater. Process. Technol. 214 (2014) 2915–2925.

[102] D.B. Hann, J. Iammi, J. Folkes, A simple methodology for predicting laser-weld properties from material and laser parameters, J. Phys. D. Appl. Phys. 44 (2011) 445401.

[103] J. Ye, A.M. Rubenchik, M.F. Crumb, G. Guss, M.J. Matthews, Laser Absorption and Scaling Behavior in Powder Bed Fusion Additive Manufacturing of Metals, Conf. Lasers Electro-Optics, OSA Tech. Dig. (Optical Soc. Am. 2018). JW2A (2018).

[104] R.M. Hunt, K.J. Kramer, B. El-Dasher, Selective laser sintering of MA956 oxide dispersion strengthened steel, J. Nucl. Mater. 464 (2015) 80–85.

[105] R. Fabbro, Scaling laws for the laser welding process in keyhole mode, J. Mater. Process. Technol. 264 (2019) 346–351.

[106] J. Yang, J. Han, H. Yu, J. Yin, M. Gao, Z. Wang, X. Zeng, Role of molten pool mode on formability, microstructure and mechanical properties of selective laser melted Ti-6Al-4V

alloy, Mater. Des. 110 (2016) 558–570.
[107] U. Scipioni Bertoli, A.J. Wolfer, M.J. Matthews, J.-P.R. Delplanque, J.M. Schoenung, On the limitations of Volumetric Energy Density as a design parameter for Selective Laser Melting, Mater. Des. 113 (2017) 331–340.
[108] S. Sulaiman, L.Y. Pio, Validation of Magmasoft simulation of the sand casting process, Inst. Eng. Malaysia. 65 (2004) 55–64.
[109] M. Sokolov, A. Salminen, Methods for Improving Laser Beam Welding Efficiency, Phys. Procedia. 56 (2014) 450–457.
[110] Y. Cheng, X. Jin, S. Li, L. Zeng, Fresnel absorption and inverse bremsstrahlung absorption in an actual 3D keyhole during deep penetration CO2 laser welding of aluminum 6016, Opt. Laser Technol. 44 (2012) 1426–1436.
[111] T. DebRoy, S.A. David, Physical processes in fusion welding, Rev. Mod. Phys. 67 (1995) 85–112.
[112] A. Kaplan, A model of deep penetration laser welding based on calculation of the keyhole profile, J. Phys. D. Appl. Phys. 27 (1994) 1805–1814.
[113] F.L. Pedrotti, L.S. Pedrotti, Introduction to Optics (3rd Edition), Pearson Educ. (2006) 656.
[114] R. Fabbro, Melt pool and keyhole behaviour analysis for deep penetration laser welding, J. Phys. D. Appl. Phys. 43 (2010) 445501.
[115] Q. Guo, M. Qu, L.I. Escano, S.M.H. Hojjatzadeh, Z. Young, K. Fezzaa, L. Chen, Revealing melt flow instabilities in laser powder bed fusion additive manufacturing of aluminum alloy via in-situ high-speed X-ray imaging, Int. J. Mach. Tools Manuf. 175 (2022) 103861.
[116] F. Wirth, S. Arpagaus, K. Wegener, Analysis of melt pool dynamics in laser cladding and direct metal deposition by automated high-speed camera image evaluation, Addit. Manuf. 21 (2018) 369–382.
[117] M. Poletto, D.D. Joseph, Effective density and viscosity of a suspension, J. Rheol. (N. Y. N. Y). 39 (1995) 323–343.
[118] K. Abderrazak, S. Bannour, H. Mhiri, G. Lepalec, M. Autric, Numerical and experimental study of molten pool formation during continuous laser welding of AZ91 magnesium alloy, Comput. Mater. Sci. 44 (2009) 858–866.
[119] P. Jin, H. Sumeng, W. Xingxing, W. Jiansheng, Z. Furong, Effect of filler metal on three-dimensional transient behavior of keyholes and molten pools in laser welding, Chinese J. Lasers. 45 (2018) 0102003.
[120] A. Paul, T. Debroy, Free surface flow and heat transfer in conduction mode laser welding, Metall. Trans. B. 19 (1988) 851–858.
[121] I. Eriksson, J. Powell, A.F.H. Kaplan, Melt behavior on the keyhole front during high speed laser welding, Opt. Lasers Eng. 51 (2013) 735–740.
[122] H. Nakamura, Y. Kawahito, K. Nishimoto, S. Katayama, Elucidation of melt flows and spatter formation mechanisms during high power laser welding of pure titanium, J. Laser Appl. 27 (2015) 032012.
[123] A. Matsunawa, N. Seto, M. Mizutani, S. Katayama, Liquid motion in keyhole laser welding, in: Int. Congr. Appl. Lasers Electro-Optics, Laser Institute of America, 1998: pp. G151–G160.
[124] B. Chang, C. Allen, J. Blackburn, P. Hilton, D. Du, Fluid flow characteristics and porosity behavior in full penetration laser welding of a titanium alloy, Metall. Mater. Trans. B. 46 (2015) 906–918.
[125] J. Peng, L. Li, S. Lin, F. Zhang, Q. Pan, S. Katayama, High-speed x-ray transmission and numerical study of melt flows inside the molten pool during laser welding of aluminum alloy, Math. Probl. Eng. 2016 (2016) 1–13.
[126] Z.S. Saldi, Marangoni driven free surface flows in liquid weld pools, Delft University of

Technology, 2012.

[127] S. Kou, Y.H. Wang, Computer simulation of convection in moving arc weld pools, Metall. Trans. A. 17 (1986) 2271–2277.

[128] Y. Kawahito, Y. Uemura, Y. Doi, M. Mizutani, K. Nishimoto, H. Kawakami, M. Tanaka, H. Fujii, K. Nakata, S. Katayama, Elucidation of the effect of welding speed on melt flows in high-brightness and high-power laser welding of stainless steel on basis of three-dimensional X-ray transmission in situ observation, Weld. Int. 31 (2017) 206–213.

[129] S. Kou, C. Limmaneevichitr, P.S. Wei, Oscillatory Marangoni flow: a fundamental study by conduction-mode laser spot welding, Weld. J. 90 (2011) 229–240.

[130] L. Zhang, J. Zhang, G. Zhang, W. Bo, S. Gong, An investigation on the effects of side assisting gas flow and metallic vapour jet on the stability of keyhole and molten pool during laser full-penetration welding, J. Phys. D. Appl. Phys. 44 (2011) 135201.

[131] A. Matsunawa, N. Seto, J.-D. Kim, M. Mizutani, S. Katayama, Dynamics of keyhole and molten pool in high-power CO 2 laser welding, in: X. Chen, T. Fujioka, A. Matsunawa (Eds.), High-Power Lasers Manuf., International Society for Optics and Photonics, 2000: p. 34.

[132] M. Schaefer, S. Kessler, F. Fetzer, T. Graf, Influence of the focal position on the melt flow during laser welding of steel, J. Laser Appl. 29 (2017) 012010.

[133] M. Bachmann, V. Avilov, A. Gumenyuk, M. Rethmeier, About the influence of a steady magnetic field on weld pool dynamics in partial penetration high power laser beam welding of thick aluminium parts, Int. J. Heat Mass Transf. 60 (2013) 309–321.

[134] M. Xia, D. Gu, G. Yu, D. Dai, H. Chen, Q. Shi, Selective laser melting 3D printing of Ni-based superalloy: understanding thermodynamic mechanisms, Sci. Bull. 61 (2016) 1013–1022.

[135] T. Zhang, H. Li, S. Liu, S. Shen, H. Xie, W. Shi, G. Zhang, B. Shen, L. Chen, B. Xiao, M. Wei, Evolution of molten pool during selective laser melting of Ti–6Al–4V, J. Phys. D. Appl. Phys. 52 (2019) 055302.

[136] B. Schoinochoritis, D. Chantzis, K. Salonitis, Simulation of metallic powder bed additive manufacturing processes with the finite element method: A critical review, Proc. Inst. Mech. Eng. Part B J. Eng. Manuf. 231 (2017) 96–117.

[137] M. Matthews, J. Trapp, G. Guss, A. Rubenchik, Direct measurements of laser absorptivity during metal melt pool formation associated with powder bed fusion additive manufacturing processes, J. Laser Appl. 30 (2018) 032302.

[138] A.A. Martin, N.P. Calta, J.A. Hammons, S.A. Khairallah, M.H. Nielsen, R.M. Shuttlesworth, N. Sinclair, M.J. Matthews, J.R. Jeffries, T.M. Willey, J.R.I. Lee, Ultrafast dynamics of laser-metal interactions in additive manufacturing alloys captured by in situ X-ray imaging, Mater. Today Adv. 1 (2019) 100002.

[139] N. Kouraytem, X. Li, R. Cunningham, C. Zhao, N. Parab, T. Sun, A.D. Rollett, A.D. Spear, W. Tan, Effect of laser-matter interaction on molten pool flow and keyhole dynamics, Phys. Rev. Appl. 11 (2019) 064054.

[140] Y. Chen, S.J. Clark, C.L.A. Leung, L. Sinclair, S. Marussi, M.P. Olbinado, E. Boller, A. Rack, I. Todd, P.D. Lee, In-situ Synchrotron imaging of keyhole mode multi-layer laser powder bed fusion additive manufacturing, Appl. Mater. Today. 20 (2020) 100650.

[141] L. Wang, Y. Zhang, W. Yan, Evaporation Model for Keyhole Dynamics During Additive Manufacturing of Metal, Phys. Rev. Appl. 14 (2020) 064039.

[142] Q. Guo, M. Qu, C.A. Chuang, L. Xiong, A. Nabaa, Z.A. Young, Y. Ren, P. Kenesei, F. Zhang, L. Chen, Phase transformation dynamics guided alloy development for additive manufacturing, Addit. Manuf. 59 (2022) 103068.

[143] J.W. Elmer, T.A. Palmer, E.D. Specht, Direct Observations of Sigma Phase Formation in Duplex Stainless Steels Using In-Situ Synchrotron X-Ray Diffraction, Metall. Mater. Trans. A. 38 (2007) 464–475.

[144] S.A. Oh, R.E. Lim, J.W. Aroh, A.C. Chuang, B.J. Gould, J. V. Bernier, N. Parab, T. Sun, R.M. Suter, A.D. Rollett, Microscale observation via high-speed X-ray diffraction of alloy 718 during in situ laser melting, JOM. 73 (2021) 212–222.

[145] F. Zhang, J. Ilavsky, G.G. Long, J.P.G. Quintana, A.J. Allen, P.R. Jemian, Glassy carbon as an absolute intensity calibration standard for small-angle scattering, Metall. Mater. Trans. A. 41 (2010) 1151–1158.

[146] J. Ilavsky, F. Zhang, R.N. Andrews, I. Kuzmenko, P.R. Jemian, L.E. Levine, A.J. Allen, Development of combined microstructure and structure characterization facility for in situ and operando studies at the Advanced Photon Source, J. Appl. Crystallogr. 51 (2018) 867–882.

[147] F. Zhang, L.E. Levine, A.J. Allen, M.R. Stoudt, G. Lindwall, E.A. Lass, M.E. Williams, Y. Idell, C.E. Campbell, Effect of heat treatment on the microstructural evolution of a nickel-based superalloy additive-manufactured by laser powder bed fusion, Acta Mater. 152 (2018) 200–214.

[148] J. Ilavsky, P.R. Jemian, Irena : tool suite for modeling and analysis of small-angle scattering, J. Appl. Crystallogr. 42 (2009) 347–353.

[149] F. Villaret, X. Boulnat, P. Aubry, J. Zollinger, D. Fabrègue, Y. de Carlan, Modelling of delta ferrite to austenite phase transformation kinetics in martensitic steels: Application to rapid cooling in additive manufacturing, Materialia. 18 (2021) 101157.

[150] S. Vunnam, A. Saboo, C. Sudbrack, T.L. Starr, Effect of powder chemical composition on the as-built microstructure of 17-4 PH stainless steel processed by selective laser melting, Addit. Manuf. 30 (2019) 100876.

[151] S. Sabooni, A. Chabok, S.C. Feng, H. Blaauw, T.C. Pijper, H.J. Yang, Y.T. Pei, Laser powder bed fusion of 17–4 PH stainless steel: A comparative study on the effect of heat treatment on the microstructure evolution and mechanical properties, Addit. Manuf. 46 (2021) 102176.

[152] J. Wang, P.J. van der Wolk, S. van der Zwaag, Determination of Martensite Start Temperature in Engineering Steels Part I. Empirical Relations Describing the Effect of Steel Chemistry, Mater. Trans. JIM. 41 (2000) 761–768.

[153] C. Capdevila, F.G. Caballero, C.G. de Andrés, Determination of Ms Temperature in Steels: A Bayesian Neural Network Model., ISIJ Int. 42 (2002) 894–902.

[154] L. Ryde, Application of EBSD to analysis of microstructures in commercial steels, Mater. Sci. Technol. 22 (2006) 1297–1306.

[155] J. WU, P.J. Wray, C.I. GARCIA, M. HUA, A.J. Deardo, Image quality analysis: A new method of characterizing microstructures, ISIJ Int. 45 (2005) 254–262.

[156] S. Zaefferer, J. Ohlert, W. Bleck, A study of microstructure, transformation mechanisms and correlation between microstructure and mechanical properties of a low alloyed TRIP steel, Acta Mater. 52 (2004) 2765–2778.

[157] M. Akbari, R. Kovacevic, An investigation on mechanical and microstructural properties of 316LSi parts fabricated by a robotized laser/wire direct metal deposition system, Addit. Manuf. 23 (2018) 487–497.

[158] G. Yeli, M.A. Auger, K. Wilford, G.D.W.W. Smith, P.A.J.J. Bagot, M.P. Moody, Sequential nucleation of phases in a 17-4PH steel: Microstructural characterisation and mechanical properties, Acta Mater. 125 (2017) 38–49.

[159] Y. Sun, R.J. Hebert, M. Aindow, Effect of heat treatments on microstructural evolution of additively manufactured and wrought 17-4PH stainless steel, Mater. Des. 156 (2018) 429–440.

[160] T. DebRoy, T. Mukherjee, H.L. Wei, J.W. Elmer, J.O. Milewski, Metallurgy, mechanistic models and machine learning in metal printing, Nat. Rev. Mater. 6 (2021) 48–68.

[161] T.D. Ngo, A. Kashani, G. Imbalzano, K.T.Q. Nguyen, D. Hui, Additive manufacturing (3D printing): A review of materials, methods, applications and challenges, Compos. Part B

Eng. 143 (2018) 172–196.

[162] P. Bidare, I. Bitharas, R.M. Ward, M.M. Attallah, A.J. Moore, Laser powder bed fusion at sub-atmospheric pressures, Int. J. Mach. Tools Manuf. 130–131 (2018) 65–72.

[163] T. Achee, G. Guss, A. Elwany, M. Matthews, Laser pre-sintering for denudation reduction in the laser powder bed fusion additive manufacturing of Ti-6Al-4V alloy, Addit. Manuf. 42 (2021) 101985.

[164] M. Qu, Q. Guo, L.I. Escano, A. Nabaa, S.M.H. Hojjatzadeh, Z.A. Young, L. Chen, Controlling process instability for defect lean metal additive manufacturing, Nat. Commun. 13 (2022) 1079.

Appendices

Appendix A – Copyright Permissions

Chapters 3–6 contain material from previous published work [37,43,59,115]. The permissions for the usage of figures from those papers are shown below in Figures A1–A4.

Transient dynamics of powder spattering in laser powder bed fusion additive manufacturing process revealed by in-situ high-speed high-energy x-ray imaging

Author: Qilin Guo,Cang Zhao,Luis I. Escano,Zachary Young,Lianghua Xiong,Kamel Fezzaa,Wes Everhart,Ben Brown,Tao Sun,Lianyi Chen

Publication: Acta Materialia

Publisher: Elsevier

Date: 1 June 2018

© 2018 Acta Materialia Inc. Published by Elsevier Ltd. All rights reserved.

Journal Author Rights

Please note that, as the author of this Elsevier article, you retain the right to include it in a thesis or dissertation, provided it is not published commercially. Permission is not required, but please ensure that you reference the journal as the original source. For more information on this and on your other retained rights, please visit: https://www.elsevier.com/about/our-business/policies/copyright#Author-rights

Figure A1. Copyright permission for the material of [43].

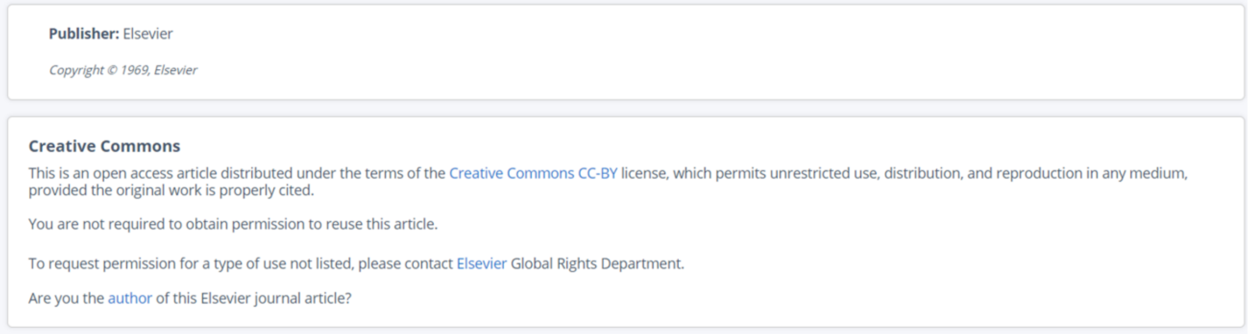

Publisher: Elsevier

Copyright © 1969, Elsevier

Creative Commons

This is an open access article distributed under the terms of the Creative Commons CC-BY license, which permits unrestricted use, distribution, and reproduction in any medium, provided the original work is properly cited.

You are not required to obtain permission to reuse this article.

To request permission for a type of use not listed, please contact Elsevier Global Rights Department.

Are you the author of this Elsevier journal article?

Figure A2. Copyright permission for materials of [37,59] (open access).

Revealing melt flow instabilities in laser powder bed fusion additive manufacturing of aluminum alloy via in-situ high-speed X-ray imaging

Author: Qilin Guo,Minglei Qu,Luis I. Escano,S. Mohammad H. Hojjatzadeh,Zachary Young,Kamel Fezzaa,Lianyi Chen

Publication: International Journal of Machine Tools and Manufacture

Publisher: Elsevier

Date: April 2022

© 2022 Published by Elsevier Ltd.

Journal Author Rights

Please note that, as the author of this Elsevier article, you retain the right to include it in a thesis or dissertation, provided it is not published commercially. Permission is not required, but please ensure that you reference the journal as the original source. For more information on this and on your other retained rights, please visit: https://www.elsevier.com/about/our-business/policies/copyright#Author-rights

Figure A3. Copyright permission for the material of [115].

Phase transformation dynamics guided alloy development for additive manufacturing

Author: Qilin Guo,Minglei Qu,Chihpin Andrew Chuang,Lianghua Xiong,Ali Nabaa,Zachary A. Young,Yang Ren,Peter Kenesei,Fan Zhang,Lianyi Chen

Publication: Additive Manufacturing

Publisher: Elsevier

Date: November 2022

© 2022 Elsevier B.V. All rights reserved.

Journal Author Rights

Please note that, as the author of this Elsevier article, you retain the right to include it in a thesis or dissertation, provided it is not published commercially. Permission is not required, but please ensure that you reference the journal as the original source. For more information on this and on your other retained rights, please visit: https://www.elsevier.com/about/our-business/policies/copyright#Author-rights

Figure A4. Copyright permission for the material of [142].

Appendix B – Extended Data

Figure A5. Extended data of Figure 50 showing more representative diffraction spots of δ-ferrite during cooling.